A Bunch Compressor for small Emittances and high Peak Currents at the VUV Free-Electron Laser

by Frank Stulle

University of Hamburg

A Bunch Compressor for small Emittances and high Peak Currents at the VUV Free-Electron Laser

Dissertation
zur Erlangung des Doktorgrades
des Fachbereichs Physik
der Universität Hamburg

vorgelegt von
Frank Stulle
aus Hamburg

Hamburg
2004

Gutachter der Dissertation:	Prof. Dr. J. Roßbach Prof. Dr. P. Schmüser
Gutachter der Disputation:	Prof. Dr. R. D. Heuer Prof. Dr. J. Roßbach
Datum der Disputation:	28.09.2004
Vorsitzende des Prüfungsausschusses:	Prof. Dr. C. Hagner
Vorsitzender der Promotionsausschusses:	Prof. Dr. R. Wiesendanger
Dekan des Fachbereichs Physik:	Prof. Dr. G. Huber

Abstract

The Free-Electron Laser (FEL) at the TESLA Test Facility (TTF2) produces laser-like radiation in the vacuum-ultraviolet (VUV) and soft X-ray regime. To reach the minimum radiation wavelength of 6 nm, bunches of electrons with an energy of 1 GeV, a peak current of 2500 A and a normalized transverse emittance of less than 2 mm mrad are needed.

The high peak current is achieved by compressing the electron bunches longitudinally in two magnetic chicanes. The first chicane is a modified version of bunch compressor 2 (BC2) which was used at TTF1. The second chicane is a new bunch compressor, the so called BC3. Since the charge density is very high when the bunches pass BC3, strong coherent synchrotron radiation (CSR) is emitted by the electrons and the transverse emittance of the bunch is diluted. Within this thesis different chicane layouts are compared analytically and by computer simulations to find a chicane layout which minimizes emittance dilution. A 6-bend S-shaped chicane is found to match the requirements of the VUV-FEL very well.

CSR will not only lead to a growth of the transverse emittance, but also to an amplification of small modulations in energy and charge density. The dependence of the amplification on the modulation wavelength is studied for different chicane layouts and various electron bunch parameters. Computer simulations and results obtained by a theoretical model are compared. It is shown that density modulations can be amplified in BC3 by up to one order of magnitude. When the amplification in BC2 and BC3 is taken into account, the total amplification factor might reach up to two orders of magnitude.

Zusammenfassung

Der Freie-Elektronen Laser (FEL) der TESLA Test Anlage (TTF2) erzeugt Laser-artige Strahlung im vakuum-ultravioletten (VUV) und weichen Röntgenspektrum. Um die minimale Wellenlänge von 6 nm erreichen zu können, müssen die Elektronenpulse eine Energie von 1GeV und einen Spitzenstrom von 2500A haben. Ihre normierte transversale Emittanz darf 2 mm mrad nicht überschreiten.

Der hohe Spitzenstrom wird erreicht, indem die Elektronenpulse in zwei Magnetschikanen longitudinal komprimiert werden. Die erste Schikane ist eine modifizerte Version des Bunch Compressor 2 (BC2), der bei TTF1 verwendet wurde. Die zweite Schikane ist eine neue Schikane und wird BC3 genannt. Da die Ladungsdichte sehr hoch ist, wenn die Elektronenpulse BC3 passieren, wird starke kohärente Synchrotronstrahlung (CSR) erzeugt und die transversale Emittanz wird vergrößert. In dieser Arbeit werden verschiedene Magnetschikanen analytisch und mit Hilfe von Computersimulationen verglichen, um eine Anordnung der Ablenkmagnete zu finden, bei welcher die Emittanzvergrößerung möglichst gering ist. Es wird gezeigt, dass eine S-förmige Schikane aus sechs Dipolen die Anforderungen des VUV-FEL's sehr gut erfüllt.

CSR führt nicht nur zu einer Vergrößerung der transversalen Emittanz, sondern auch zu einer Verstärkung kleiner Energie- und Ladungsdichtemodulationen. Die Abhängigkeit der Verstärkung von der Modulationswellenlänge wird für verschiedene Schikanen und Elektronenpulsparameter untersucht. Computersimulationen und die Ergebnisse eines theoretischen Modells werden verglichen. Es zeigt sich, dass Dichtemodulationen in BC3 um eine Größenordnung verstärkt werden können. Berücksichtigt man die Verstärkung in BC2 und BC3, so kann die gesamte Verstärkung zwei Größenordnungen erreichen.

Contents

Chapter 1

Introduction

Since the early 1990's there is a broad consensus within the high energy physics community, that a linear accelerator which collides electrons on positrons at a center of mass energy of $E_{\mathrm{cm}} = 500 - 1000\,\mathrm{GeV}$ would be of enormous importance for the further understanding of particle physics. The concept of such a linear collider was already proposed in 1965 by M. Tigner [1]. But it has been realized until today only in the Stanford Linear Collider (SLC) in Stanford, USA, which collided electrons and positrons at $E_{\mathrm{cm}} = 91$ GeV [2].

The highest energies for electron-positron collisions were reached at the Large Electron-Positron Collider (LEP) at CERN (Conseil Européen pour la Recherche Nucléaire, European Organization for Nuclear Research) in Geneva, Switzerland. LEP was a storage ring of 27 km circumference and reached up to $E_{\mathrm{cm}} = 209$ GeV [3]. It was shut down in November 2000 and in 2001 the construction of the Large Hadron Collider (LHC) began in the LEP tunnel. This new storage ring will collide protons on protons at a center of mass energy of $E_{\mathrm{cm}} = 14\,\mathrm{TeV}$ [4]. The high-precision measurements which are possible at a linear electron-positron collider will complement the LHC results. Together, both accelerators have the potential to establish fundamentally new insight into particle physics even beyond the Standard Model.

To design a linear collider which is based on superconducting technology, in 1992 the international TESLA (TeV Energy Superconducting Linear Accelerator) collaboration was initiated at the Deutsches Elektronen-Synchrotron (DESY) in Hamburg, Germany [5]. At that time groups from the National Laboratory for High Energy Physics (KEK) in Tsukuba, Japan [6] and the Stanford Linear Accelerator Center (SLAC) in Stanford, USA [7] also started to work on linear collider designs. In contrast to TESLA these designs are based on normal-conducting technology.

Very soon it was proposed to include an X-ray Free-Electron Laser (FEL) in TESLA sharing part of the accelerating structures [8]. Also the FEL demands a high beam quality which is inherent to the TESLA design. Since the interest in X-ray FELs for research in the field of condensed matter physics, chemistry, material sciences and structural biology is very high, other projects are also under study worldwide. The principal example is the Linac Coherent Light Source (LCLS) where it was proposed to make use of a linear accelerator to drive an FEL for X-rays for the first time [9].

Although the TESLA linear collider and the X-ray FEL were initially proposed as a combined system, they were later divided into independent projects to gain flexibility for their distinct needs. Still, both are based on the same superconducting technology [10].

To prove the feasibility of a high-gradient superconducting accelerator, a TESLA test facility (TTF) was built during the 1990's [11, 12]. Also the principle of a Free-Electron Laser based on the self-amplified spontaneous emission (SASE) scheme in the VUV regime was proven by the generation of FEL radiation in the range from 80 nm to 180 nm [13]. To expand the possibilities of the initial TTF a new test facility is being built and will start operation in 2004 [14], providing a source of laser-like radiation in the range from 6 nm up to approximately 100 nm.

1.1 The X-Ray Free-Electron Laser

Over the past decades synchrotron radiation has become a major tool for the analysis of structural and electrical properties of atoms, molecules and solid state matter. The growing interest in dedicated radiation sources led to the development of the so called 3rd-generation light sources (e.g. Advanced Photon Source (APS) in Argonne, USA, European Synchrotron Radiation Facility (ESRF) in Grenoble, France, Super Photon Ring 8 GeV (SPring-8) in Harima, Japan). These specially designed storage rings use insertion devices like wigglers and undulators to increase the peak and average brilliance by several orders of magnitude with respect to the spontaneously emitted light from the bending magnets.

The X-ray FEL will not only extend today's light sources by increasing the brilliance of the radiation (figure 1.1). Its sub-picosecond light pulses of very narrow bandwidth will enable scientists to perform experiments which have never been possible before. For example, diffraction patterns of single molecules can be produced with a single light pulse from the X-ray FEL . This is of special interest in biology where molecules can often only be crystallized on a very small scale or even not at all. To study dynamical processes on an atomic scale, up to 4000 light pulses with an rms length of 80 fs each can be produced within a bunch train 800 μs long. The radiation wavelength will be tunable in the range of $0.1 - 6$ nm.

The X-ray FEL includes a photo-injector which produces electron bunches with a charge of 1nC. It will be located on the DESY site in Hamburg. The linac accelerates the electrons to an energy of up to 20 GeV. The experimental hall will be located about 3.3 km to the north-west of the DESY site. It is planned to start the construction of the X-ray FEL in 2006. In 2012 the first radiation is expected to be delivered to the experiments [10].

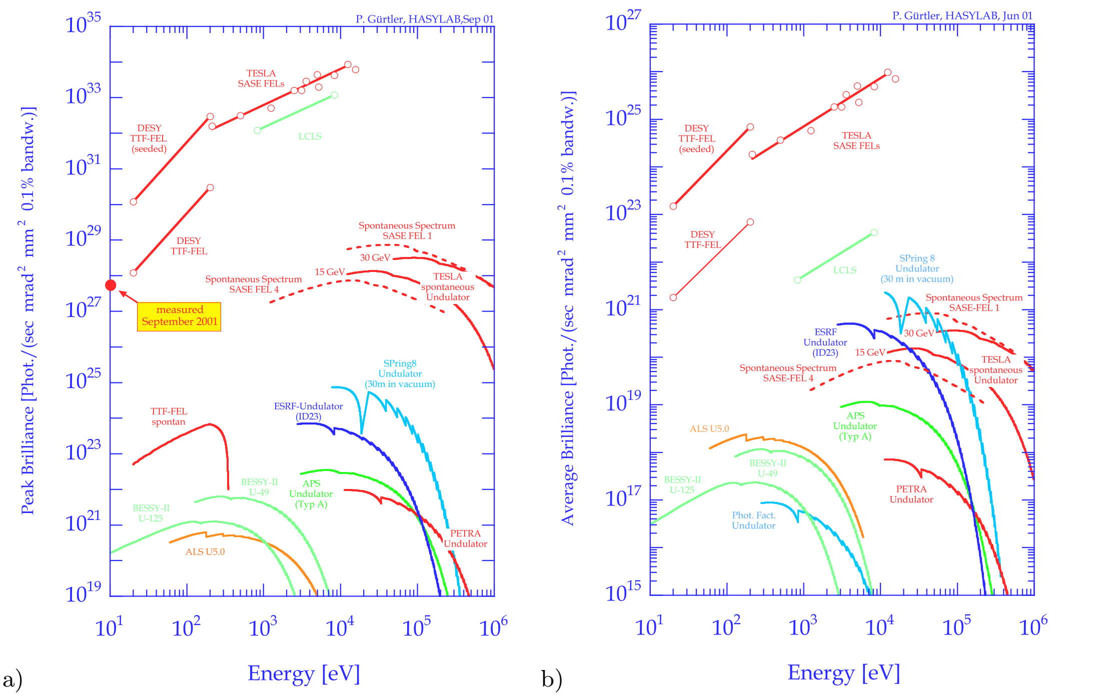

Figure 1.1: *The peak brilliance (a) and the average brilliance (b) of the FELs will surpass today's synchrotron radiation sources by several orders of magnitude over a wide range of photon energies. (pictures by P. Gürtler)*

1.2 The TESLA Test Facility

The TESLA Test Facility (TTF) linac started operation in 1996. Initially, it consisted of a thermionic electron gun and a single superconducting accelerating module. During the following years TTF linac was extended to drive an FEL based on the self-amplified spontaneous emission scheme (SASE). Its construction was finished in July 1999. At that time, the linac included a radio-frequency (RF) gun which was built by the Fermi National Accelerator Laboratory (FNAL) in Batavia, USA, two accelerating modules and three undulator sections each 4.5 m long. The beam was compressed by bunch compressor chicanes at 15 MeV and at 140 MeV. Following a commissioning period, in February 2000 the first radiation from the SASE FEL was observed at a wavelength of 109 nm [15]. Saturation of the radiation intensity was reached for the first time in September 2001 at a wavelength of 98 nm and until 2002 saturation was achieved in the wavelength range from 80 nm to 120 nm [13]. At the end of 2003 TTF was shut down and the construction of the second phase of TTF began. By then a total operation time of 13000 h had accumulated.

A major step towards the X-ray FEL will be the second phase of the TESLA Test Facility (TTF2) which will drive an FEL in the vacuum-ultraviolet and soft X-ray regime (VUV-FEL) [14]. TTF2 is not just an expansion of TTF, but a completely new machine. Only few components will be reused, some can be modified. In February 2004 the commissioning of the RF gun started. By the second half of 2004 the remaining construction work will be finished and the VUV-FEL will start operation. In contrast to the original test facility, the VUV-FEL will ultimately become a user facility.

The RF gun at TTF2 can produce electron bunches of up to 4 nC charge. The electrons are accelerated in the 1.5-cell cavity of the gun and the first accelerating module ACC1 to an energy of about 120 MeV. All cavities work at a frequency of 1.3 GHz. In the following bunch compressor, called BC2 for historical reasons, the bunch length can be reduced by about a factor of 8. Before the second compression step in BC3 the electrons are accelerated in modules ACC2 and ACC3 to an energy of 450 MeV. In BC3 the bunch length can be reduced by another factor of 5. The following two modules accelerate the electrons up to 800 MeV. To prevent radiation damage to the undulators a collimation section is included. The SASE FEL will produce radiation in the range of $6 - 100$ nm. At a later time, a 3^{rd}-harmonic cavity, i.e. a cavity working at 3.9 GHz, will be included in front of BC2 to improve bunch compression [16]. There is also space foreseen for two additional accelerating modules which increase the electron energy to 1000 GeV. The higher energy is needed to produce radiation of 6 nm wavelength. For a seeding option additional undulators can be installed (figure 1.2).

The experimental hall will provide space for five experiments and some additional space for preparation, on-line diagnostics and a synchronized optical laser for pump-probe experiments (figure 1.3). Three of the experimental stations will use the FEL radiation directly whereas the other two are served by a monochromator which narrows the spectral bandwidth of the radiation. A reduction of the radiation intensity can be achieved by a gas-filled cell of about 15 m length in front of the hall. More information on photon beam diagnostics can be found in [18].

Experiments are proposed from a variety of research areas. The proposals include experiments on atoms, ions, molecules and clusters as well as solids and surfaces or plasmas. Additionally, some effort aims at the technical development of new experimental set-ups, e.g. for pump-probe experiments using FEL radiation [18, 19].

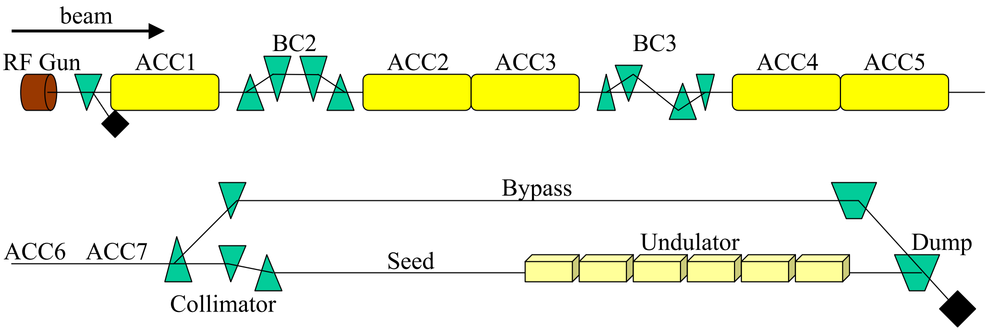

Figure 1.2: *A sketch of TTF2 is given. The electrons are produced in the RF gun. They are accelerated in the accelerating modules ACC1–ACC7. The bunch compression occurs in the chicanes BC2 and BC3. Collimators protect the undulators from radiation damage. The undulators can be bypassed. (picture taken from [17])*

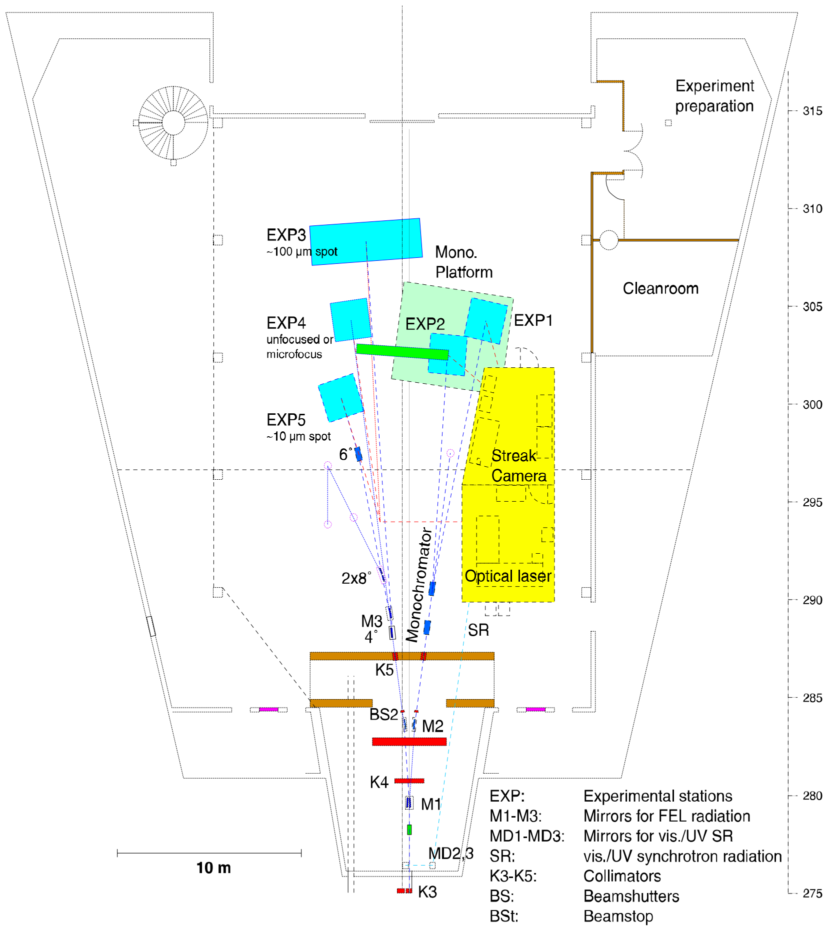

Figure 1.3: *The experimental hall provides space for five different experimental stations. (picture taken from [19])*

Chapter 2

The Principle of Free-Electron Lasers

In 1971 J.M.J. Madey gave a quantum mechanical description of the stimulated emission of bremsstrahlung by highly relativistic electrons passing periodic magnetic fields [20]. An externally applied electromagnetic wave which propagates parallel to the electrons will be amplified and finally laser-like radiation will be produced. Since the electrons are not bound to any medium, Madey called such a device free-electron laser (FEL). In accordance with the theoretical description, in 1976 the stimulated emission was observed at a frequency of 10 μm [21].

The formalism given by J.M.J. Madey assumes that the energy of the electromagnetic wave changes only by a small amount during one passage through the periodic magnetic field. This case is called the low-gain FEL. It is described in section 2.1. In a high-gain FEL the energy of the electromagnetic wave can grow by several orders of magnitude within a single passage. The high-gain case is described in section 2.2. There we will see that the performance of an FEL depends not only on the peak current of the beam and the electron energy but also on the energy spread of the beam and its transverse emittance. Consequently, the requirements of the FEL define the performance which has to be matched by the linac producing and accelerating the electron beam.

2.1 The Low-Gain FEL

The physical processes leading to the amplification of electromagnetic waves in low-gain and high-gain FELs are described by a classical approach, for example in [22, 23, 24]. Based on [23] I will outline the principles of FEL physics. In a helical undulator[1] the trajectory of the electrons can be expressed as the combination of a uniform longitudinal motion $z = v_\mathrm{z}\, t$ and a transverse circular motion

$$\begin{pmatrix} v_\mathrm{x} \\ v_\mathrm{y} \end{pmatrix} = c\frac{K}{\gamma}\begin{pmatrix} -\sin(k_\mathrm{u} z) \\ \cos(k_\mathrm{u} z) \end{pmatrix}$$

where $K = \frac{e_0 B_\mathrm{u} \lambda_\mathrm{u}}{2\pi m_\mathrm{e} c}$ is the undulator parameter given by the period length $\lambda_\mathrm{u} = \frac{2\pi}{k_\mathrm{u}}$ of the magnetic field in the undulator and its amplitude B_u. The elementary charge is e_0, m_e is the electron mass and c is the speed of light. γ is the relativistic Lorentz factor of the electrons. When an electromagnetic plane wave with the electric field components

$$\vec{E_\mathrm{L}} = E_{\mathrm{L},0}\begin{pmatrix} \cos(\omega_\mathrm{L} t - k_\mathrm{L} z - \phi_0) \\ \sin(\omega_\mathrm{L} t - k_\mathrm{L} z - \phi_0) \\ 0 \end{pmatrix}$$

and the magnetic field components

$$\vec{B_\mathrm{L}} = \frac{1}{c\,\omega_\mathrm{L}}\frac{d\vec{E_\mathrm{L}}}{dt}$$

[1] If the motion of electrons in a planar undulator is considered, the results change only quantitatively. The physical processes are the same.

overlaps with the electron beam and moves parallel to it, the two will interact. $E_{\mathrm{L},0}$ is the amplitude of the electric field and ϕ_0 is its initial phase. ω_L and k_L are the angular frequency and the wave number of the electromagnetic wave, respectively.

Inside the undulator the electrons start to oscillate and transverse velocity components are generated. These components are parallel to the transverse electric field components of the wave and, consequently, energy can be exchanged between the electrons and the wave. The magnetic field does not change the electron energy. Depending on the phase difference between the electron oscillation and the electromagnetic wave, the energy is transferred from the electrons into the wave or from the wave into the electrons. If the phase difference changes very rapidly the energy exchange cancels in average. Only if the phase difference is constant a net energy transfer is possible. This condition is met if the wavelength of the electromagnetic wave matches the resonance condition

$$\lambda_\mathrm{L} \approx \frac{\lambda_\mathrm{u}}{2\gamma^2}(1+K^2) \tag{2.1}$$

In this case, the energy is transferred continuously from the electrons to the electromagnetic wave.

A consequence of the energy transfer is that the resonance wavelengths shifts and the resonance condition is not fulfilled anymore. It can be shown that the electron motion in the $\Delta\gamma$-Ψ phase space is given by the pendulum equation [23]

$$\frac{d^2\Psi}{dz^2} = -\Omega^2 \sin\Psi \tag{2.2}$$

with $\Omega^2 = \frac{2e_0}{m_0c^2}\frac{E_{\mathrm{L},0}K\,k_\mathrm{u}}{\gamma_\mathrm{res}^2\beta_\mathrm{z}}$. Ψ is the phase difference between the electron oscillation and the electromagnetic wave. $\gamma = \gamma_\mathrm{res} + \Delta\gamma$ is the Lorentz factor of the electrons which are slightly off the resonance at γ_res. As a consequence of eqn. (2.2) $\Delta\gamma$ has to fulfill the equation

$$\Delta\gamma = \sqrt{C_0 + \frac{e_0E_{\mathrm{L},0}K}{m_\mathrm{e}c^2k_\mathrm{u}\beta_\mathrm{z}}\cos\Psi} \tag{2.3}$$

The constant C_0 is determined by the initial conditions.

For the motion of the electrons in the $\Delta\gamma$-Ψ phase space two cases have to be distinguished. If $C_0 < \frac{e_0E_{\mathrm{L},0}K}{m_\mathrm{e}c^2k_\mathrm{u}\beta_\mathrm{z}}$ equation (2.3) has only real solutions in a limited range of phases Ψ. The electrons will oscillate in the phase space. If $C_0 > \frac{e_0E_{\mathrm{L},0}K}{m_\mathrm{e}c^2k_\mathrm{u}\beta_\mathrm{z}}$ all phases are allowed and the electrons move unbounded. Both regimes are separated by the separatrix with $C_0 = \frac{e_0E_{\mathrm{L},0}K}{m_\mathrm{e}c^2k_\mathrm{u}\beta_\mathrm{z}}$ (figure 2.1).

For the calculation of the gain $G = \frac{\text{increase of field energy}}{\text{initial field energy}}$ of the field energy it is assumed that the field amplitude is almost constant throughout the undulator. This is called the low-gain approximation. If all electrons in the beam have the same deviation $\Delta\gamma$ from γ_res at the entrance of the undulator, the gain is

$$G = -\frac{\pi e_0^2 N_\mathrm{u}^3 \lambda_\mathrm{u}^2 K^2 n_\mathrm{e}}{\epsilon_0 m_\mathrm{e} c^2 \gamma^3}\frac{d}{d\xi}\left(\frac{\sin^2\xi}{\xi^2}\right) \tag{2.4}$$

Here N_u is number of undulator periods. $n_\mathrm{e} = \frac{N_\mathrm{e}}{V}$ is the electron density in the volume V. $\xi = 2\pi N_\mathrm{u}\frac{\Delta\gamma}{\gamma_\mathrm{res}}$ is the normalized relative energy deviation of the electrons. It is interesting to note that the gain is proportional to the derivative of the line shape function of the spontaneous undulator radiation. This is known as the Madey theorem [25]. The total

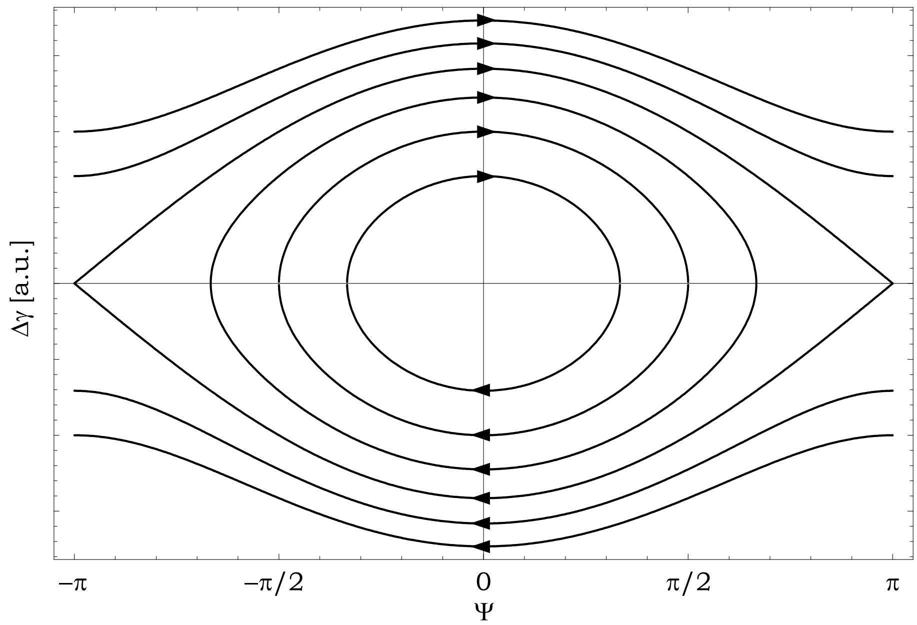

Figure 2.1: *The $\Delta\gamma$-Ψ phase space is shown for electrons with different initial conditions. Some electrons oscillate periodically, others perform unbounded motion.*

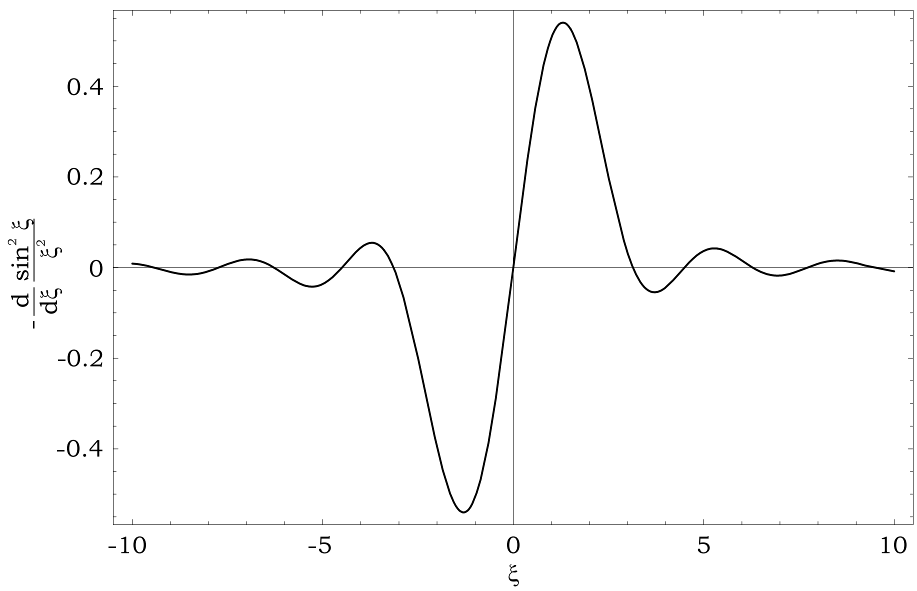

Figure 2.2: *The dependency of the normalized gain of the field energy on the initial normalized relative energy deviation of the electrons is shown.*

gain of the field energy depends on the initial electron energy. If the electron energy is slightly above the resonance energy the field energy increases. If the electron energy is slightly below the resonance energy the field energy decreases (figure 2.2).

Since the gain is small in a low-gain FEL the electromagnetic wave has to pass the undulator several times. That means, an optical cavity is needed which traps the wave and couples only a small amount of the energy out.

2.2 The High-Gain FEL

During the passage of the electrons through the undulator the field amplitude grows and the height of the separatrix $\Delta\gamma_{\text{max}} - \Delta\gamma_{\text{min}} = \sqrt{\frac{2e_0 E_{\text{L},0} K}{m_e c^2 k_u \beta_z}}$ increases. Hence, the number of electrons oscillating periodically in the phase space increases and the electron beam is longitudinally bunched at the resonance wavelength. So called micro-bunches develop. Eventually, the field energy will increase by several orders of magnitude and saturates when the density bunching of the electron beam is almost perfect (figure 2.3). In this regime the low-gain approximation is not valid and the FEL process has to be described for the high-gain case.

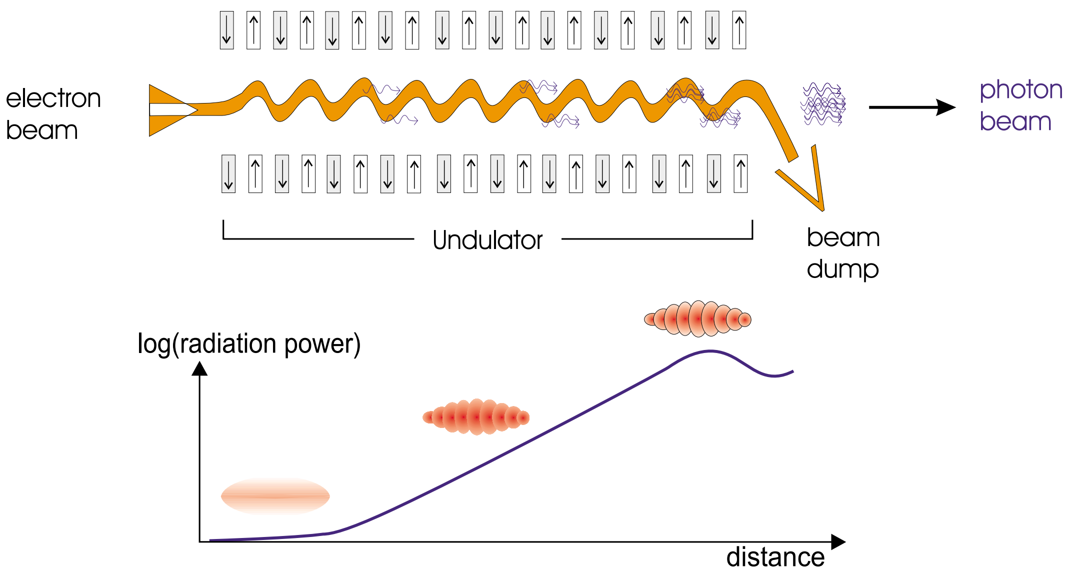

Figure 2.3: *Electrons and radiation interact along the undulator. Micro-bunches develop in the longitudinal bunch profile and the radiation power grows exponentially (picture taken from [5]).*

To take the bunching of the electrons into account for the calculation of the gain, the time-dependence of the electromagnetic wave and the electron motion have to be solved self-consistently. The radiation power will grow exponentially along the undulator and the initial field amplitude may be very small. As described by A.M. Kondratenko and E.L. Saldin it is also possible that there is no initial electromagnetic field but a small density modulation in the electron beam [26]. The random distribution of the electrons always leads to spectral components in the charge density spectrum which match the resonance condition and start the FEL process. This mechanism is called self-amplified spontaneous emission (SASE). An independent derivation was given by R. Bonifacio, C. Pellegrini and L.M. Narducci [27]. That the SASE principle is indeed working for short wavelengths was first demonstrated at the Low Energy Undulator Test Line (LEUTL) in Argonne, USA. Here in October 2000 saturation of the radiation intensity was reached for a wavelength of 390 nm [28]. One year later at the TTF-FEL saturation was reached at 80 nm wavelength [13].

For the derivation of the gain in the high-gain regime, the amplitude of the electromagnetic wave is allowed to change along the undulator. Also the electron density can change, but the induced bunching is assumed to be small. All electrons have the same initial energy. The electron beam is one-dimensional, i.e. it has no transverse extent. In this case it can be shown (see e.g. [22]) that the complex field amplitude $\tilde{E}_{\mathrm{L},0} = E_{\mathrm{L},0}e^{i\Psi_{\mathrm{L}}}$ is given by a linear third-order differential equation:

$$\frac{d^3\tilde{E}_{\mathrm{L},0}}{dz^3} + 2iC\frac{d^2\tilde{E}_{\mathrm{L},0}}{dz^2} - C^2\frac{d\tilde{E}_{\mathrm{L},0}}{dz} = i\Gamma^3\tilde{E}_{\mathrm{L},0} \tag{2.5}$$

A slow variation Ψ_{L} of the phase of the electromagnetic wave is allowed. The electron energy can deviate from the resonance energy. This is described by the detuning parameter $C(\gamma) = k_{\mathrm{u}} + k_{\mathrm{L}} - \frac{\omega_{\mathrm{L}}}{c\beta_z(\gamma)}$. $\Gamma^3 = \frac{\pi j_0 K^2(1+K^2)\omega_{\mathrm{L}}}{I_{\mathrm{A}} c\gamma^5}$ is the gain parameter with the Alven current $I_{\mathrm{A}} = \frac{4\pi m_{\mathrm{e}} c}{\mu_0 e_0}$. $j_0 = \frac{I_{\mathrm{e}}}{\pi\sigma_{\mathrm{r}}^2}$ is the initial current density given by the beam current I_{e} and the beam cross section $\pi\sigma_{\mathrm{r}}^2$.

In case of a mono-energetic electron beam which matches the resonance energy, the gain of an external electromagnetic wave along the undulator is given by

$$G(z) \approx \frac{1}{9}e^{\sqrt{3}\Gamma z} \tag{2.6}$$

if $z \gg \frac{1}{\Gamma}$. The gain grows exponentially with the gain length

$$L_{\mathrm{G}} = \frac{1}{\sqrt{3}\Gamma} = \frac{1}{\sqrt{3}}\left(\frac{I_{\mathrm{A}} c\gamma^5}{\pi j_0 K^2(1+K^2)\omega_{\mathrm{L}}}\right)^{1/3} \tag{2.7}$$

which can also be expressed in terms of the peak current $I_0 = j_0\pi\sigma_{\mathrm{r}}^2$ and the beam cross section $\pi\sigma_{\mathrm{r}}^2$:

$$L_{\mathrm{G}} = \frac{1}{\sqrt{3}}\left(\frac{I_{\mathrm{A}}\gamma^3\lambda_{\mathrm{u}}}{4\pi K^2}\frac{\sigma_{\mathrm{r}}^2}{I_0}\right)^{1/3} \tag{2.8}$$

One can see that it is preferable to use electron beams with a small transverse extent and a high peak current.

The maximum gain is reached when the beam energy is on-resonance. If the beam energy is off-resonance the gain will drop. This is an important difference to the low-gain case where the gain vanishes on-resonance and the maximum gain is achieved slightly off-resonance. The bandwidth of the FEL in the high-gain case is

$$\frac{\Delta\lambda_{\mathrm{L}}}{\lambda_{\mathrm{L}}} = 2\frac{\Delta\gamma}{\gamma} = 2\rho \tag{2.9}$$

$\rho = \frac{1}{4\pi\sqrt{3}}\frac{\lambda_{\mathrm{u}}}{L_{\mathrm{G}}}$ is the FEL parameter. Assuming an uncorrelated energy spread, electrons with $\frac{\Delta\gamma}{\gamma} > \rho$ will not contribute to the gain. A linear correlation in the energy of different electrons will broaden the radiation spectrum.

A constraint on the normalized transverse beam emittance can be derived from eqn. (2.9) . The emittance introduces a longitudinal velocity spread and thus acts like an effective energy spread [22]:

$$\varepsilon < \frac{\beta(1+K^2)}{2\gamma}\rho \tag{2.10}$$

β is the beta function describing the beam focusing. Due to diffraction of the electromagnetic wave, a large transverse overlap of the wave and the electron beam can only be achieved if the normalized emittance is [22]:

$$\varepsilon < \frac{\lambda_{\mathrm{L}}}{2\pi 3^{1/4}}\gamma \tag{2.11}$$

We can see that a SASE-FEL imposes strict requirements on the electron beam parameters. The undulators at the VUV-FEL have a period length of $\lambda_{\mathrm{u}} = 2.73$ cm and a peak field of $B_{\mathrm{u}} = 0.47$ T. The undulator parameter is $K = 1.20$. If the electron beam has a peak current of $I_0 = 2500$ A, an energy of $E_0 = 1$ GeV, an rms radius of $\sigma_{\mathrm{r}} = 70\ \mu$m and the beta function is $\beta = 4.5$ m, the gain length is $L_{\mathrm{G}} = 42$ cm. When radiation of $\lambda_{\mathrm{L}} = 6$ nm is required, equation (2.9) limits the energy spread of the electron beam at $\sigma_{\mathrm{E}} = 3\,\mathrm{MeV}$. According to equation (2.10) the normalized emittance has to be lower than $\varepsilon < 8.4\,\mathrm{mm\,mrad}$. Equation (2.11) results in a stricter limit for the normalized emittance: $\varepsilon < 1.4$ mm mrad. The parameters of the undulators and the electron beam are taken from ref. [14].

Chapter 3

Bunch Compression in Magnetic Chicanes

To drive the VUV-FEL, electron bunches with a peak current of up to 2500 A are required. Since the maximum charge density in the RF gun is limited by the space charge fields, this value can only be reached by compressing the electron bunches longitudinally when they have been accelerated to a highly relativistic energy. Unfortunately, all electrons then have velocities close to the speed of light and the speed differences inside the bunch are too small for trailing electrons to catch up with electrons ahead of them. The so called velocity bunching is only an option in the low energy part of a linac and is not discussed within this thesis. A scheme to utilize velocity bunching in the injector part of TTF2 is investigated in [29].

The only way to change the length of an ultra-relativistic electron bunch is to make use of the energy dependence of the path length in dispersive beam lines. Before an electron bunch enters such a beam line an energy slope $\frac{dE}{ds}$ is induced along the bunch in the preceding accelerating modules. In arcs made of dipoles and quadrupoles, so called FODO cells, the energy of trailing electrons needs to be lower than the energy of the electrons ahead of them to compress the bunch. Unfortunately, these layouts produce stronger nonlinear terms in the particle motion than chicanes which are built only of dipole magnets. Therefore, they are not considered within this thesis. For further information refer to [30].

In my thesis I will examine the motion of electrons in different chicanes which are built only of dipoles. These chicanes are called magnetic chicanes in contrast to the FODO cells which include quadrupoles in addition. Since the electron energy is assumed to be ultra-relativistic, it is a good approximation to neglect the rest energy of the electrons: $E_0 \approx p_0 c$. The velocity of the electrons is close to the speed of light.

General aspects of the bunch compression in magnetic chicanes are discussed in section 3.1. The momentum-dependence of the electron trajectories in C-shaped chicanes and S-shaped chicanes is derived in sections 3.2 and 3.3. Only external electric and magnetic fields are taken into account in this chapter. The influence of bunch self-interaction is discussed in the next chapter. For the bunch compressor at the Low Energy Undulator Test Line (LEUTL) in Argonne, USA, a similar study of different chicane layouts was performed by P. Emma and V. Bharadwaj [31].

3.1 General Remarks on Bunch Compression

The basic idea to reduce the length of an electron bunch in a magnetic chicane is that the deflection of the electrons in dipole magnets is energy dependent. Hence, in a chicane built of several magnets the path length of the electrons is energy dependent (figure 3.1a). The path of a high energy electron is shorter than that of a low energy electron. Thus, an energy slope has to be induced along the bunch in such a way that the tail has a higher energy than the head to get a longitudinal compression of the bunch (figure 3.1b). The longitudinal phase space is sheared (figure 3.1c). As a result not only the bunch length is reduced but the uncorrelated energy spread[1] increases at the same time. This is a consequence of Liouville's theorem which states that the phase space density has to remain unchanged under the influence of conservative forces (see e.g. [32]).

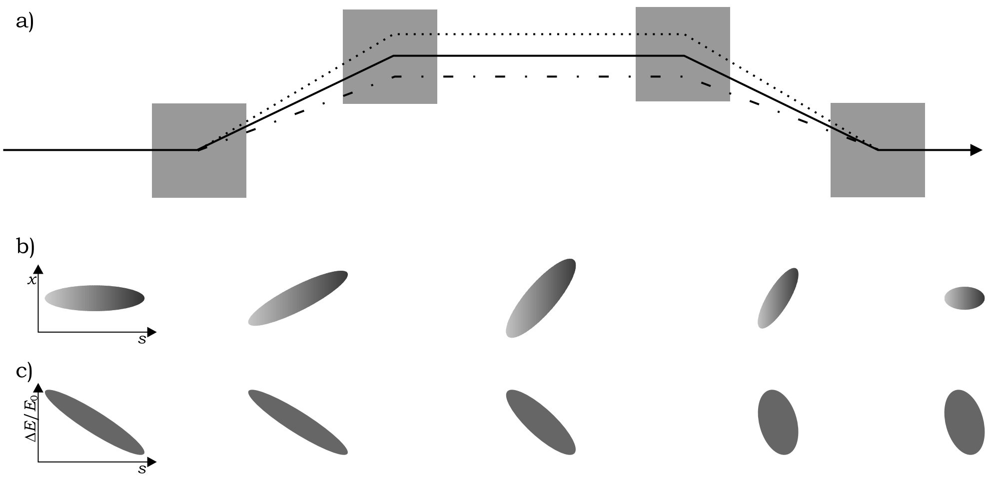

Figure 3.1: *In a magnetic chicane the path length of electrons is energy dependent (a). Electrons with a higher energy travel along a shorter path (dash dot) than electrons with nominal energy (solid). If the energy is lower the path gets longer (dotted). Therefore the high energy tail (light) of a bunch can catch up with its low energy head (dark) (b). The longitudinal phase space of the beam is sheared and the uncorrelated energy spread increases (c).*

The phase space coordinates of the electrons are given in a frame Σ^* which moves relative to the laboratory frame Σ_L along the reference trajectory $\vec{r}$ (figure 3.2).

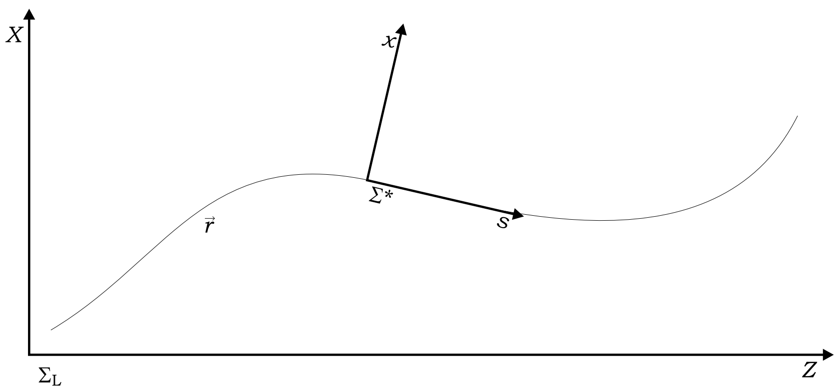

Figure 3.2: *The electron coordinates are given in a frame Σ^* that moves along the reference trajectory $\vec{r}$. The frame Σ^* moves relative to the laboratory frame Σ_L. The vertical axes Y and y are perpendicular to the X-Z-plane and the x-s-plane respectively.*

When a bunch of electrons passes a magnetic chicane the transformation of the initial phase space coordinates of an electron $(x_\mathrm{i}, x'_\mathrm{i}, y_\mathrm{i}, y'_\mathrm{i}, l_\mathrm{i}, \delta_\mathrm{E,i})$ can be described to first order

[1] The uncorrelated energy spread is the energy spread of a short slice of electrons at a given longitudinal position inside the electron bunch. It can vary along the bunch.

by a linear matrix formalism [33]:

$$\begin{pmatrix} x_\mathrm{f} \\ x'_\mathrm{f} \\ y_\mathrm{f} \\ y'_\mathrm{f} \\ l_\mathrm{f} \\ \delta_\mathrm{E,f} \end{pmatrix} = \begin{pmatrix} R_{11} & R_{12} & 0 & 0 & 0 & R_{16} \\ R_{21} & R_{22} & 0 & 0 & 0 & R_{26} \\ 0 & 0 & R_{33} & R_{34} & 0 & 0 \\ 0 & 0 & R_{43} & R_{44} & 0 & 0 \\ R_{51} & R_{52} & 0 & 0 & 1 & R_{56} \\ 0 & 0 & 0 & 0 & 0 & 1 \end{pmatrix} \begin{pmatrix} x_\mathrm{i} \\ x'_\mathrm{i} \\ y_\mathrm{i} \\ y'_\mathrm{i} \\ l_\mathrm{i} \\ \delta_\mathrm{E,i} \end{pmatrix} \tag{3.1}$$

$l_\mathrm{f} = R_{51}x_\mathrm{i} + R_{52}x'_\mathrm{i} + l_\mathrm{i} + R_{56}\delta_\mathrm{E,i}$ is the length of the path travelled by an electron with respect to the length of the reference trajectory. The contributions $R_{51}x_\mathrm{i}$ and $R_{52}x'_\mathrm{i}$ are small and can be neglected. Thus, the difference $l_\mathrm{f} - l_\mathrm{i} \approx R_{56}\delta_\mathrm{E,i}$ is the length of the path travelled by the electron along the chicane. The final longitudinal position s_f of the electron with respect to the bunch center will be

$$s_\mathrm{f} = s_\mathrm{i} - (l_\mathrm{f} - l_\mathrm{i}) = s_\mathrm{i} - R_{56}\delta_\mathrm{E,i} \tag{3.2}$$

$\delta_\mathrm{E} = \frac{\Delta E}{E_0}$ is the relative energy deviation of the electron from the nominal energy E_0. The matrix element R_{56} is called the momentum compaction factor or longitudinal dispersion.

The energy of an electron at the initial position $s_{\mathrm{i},n}$ deviates from the nominal energy to first order by a correlated energy variation which is given by the linear energy slope $u = \frac{dE}{ds}$ along the bunch and an uncorrelated energy variation which is given by the uncorrelated energy spread $\sigma_{\epsilon,\mathrm{i}} = \sqrt{\left\langle \epsilon_{\mathrm{i},n}^2 \right\rangle}$:

$$\delta_{\mathrm{E},n} = \frac{u\, s_{\mathrm{i},n} + \epsilon_{\mathrm{i},n}}{E_0}$$

Assuming an initial rms bunch length of $\sigma_\mathrm{s,i} = \sqrt{\left\langle s_{\mathrm{i},n}^2 \right\rangle}$, the final rms bunch length will be

$$\sigma_\mathrm{s,f} = \sqrt{(1 - R_{56}\,\frac{u}{E_0})^2 \sigma_\mathrm{s,i}^2 + R_{56}^2 \left(\frac{\sigma_{\epsilon,\mathrm{i}}}{E_0}\right)^2} \tag{3.3}$$

One can see that the minimum achievable rms bunch length is limited by the initial uncorrelated energy spread $\sigma_{\epsilon,\mathrm{i}}$. During compression the uncorrelated energy spread increases to $\sigma_{\epsilon,\mathrm{f}} = \sigma_{\epsilon,\mathrm{i}} \frac{\sigma_\mathrm{s,i}}{\sigma_\mathrm{s,f}}$.

If one takes into account nonlinear contributions to the electron movement, the final longitudinal position of an electron inside the bunch becomes:

$$s_\mathrm{f} = s_\mathrm{i} - R_{56}\delta_\mathrm{E} - R_{566}\delta_\mathrm{E}^2 - \ldots \tag{3.4}$$

These nonlinearities, which deform the bunch shape, limit the minimum achievable bunch length further. Especially the second order term can be strong enough to fold over the longitudinal phase space and thus produce a sharp peak at the head of the longitudinal density profile.

The same happens if the initial energy variation along the bunch includes nonlinear terms. Usually the energy variation is generated by running off-crest through accelerating cavities. The accelerating voltage changes sinusoidally in time and the electron energy gets a sinusoidal modulation along the bunch. The final energy E_f of an electron after passing an accelerating section is

$$E_\mathrm{f} = E_\mathrm{0,i} + \Delta E_\mathrm{i} + e_0 V_\mathrm{acc} \cos\left(\frac{2\pi s_\mathrm{i}}{\lambda} + \phi_0\right) \tag{3.5}$$

Here e_0 is the elementary charge, V_{acc} is the amplitude of the accelerating voltage, s_{i} is the initial longitudinal coordinate with respect to the bunch center, λ is the wavelength of the electric field and ϕ_0 is the phase offset with respect to the crest. $E_{0,\mathrm{i}}$ is the initial nominal energy and ΔE_{i} is the initial energy deviation of the particle. Since the bunch length is usually much smaller than the wavelength of the accelerating radio-frequency (RF) field, it is a good approximation to expand equation (3.5) to second order around $s_{\mathrm{i}} = 0$:

$$E_{\mathrm{f}} \approx E_{0,\mathrm{i}} + \Delta E_{\mathrm{i}} + e_0 V_{\mathrm{acc}} \left(\cos\phi_0 - s_{\mathrm{i}} \frac{2\pi}{\lambda} \sin\phi_0 - s_{\mathrm{i}}^2 \frac{2\pi^2}{\lambda^2} \cos\phi_0 \right)$$

After acceleration the nominal energy is

$$E_{0,\mathrm{f}} = E_{0,\mathrm{i}} + e_0 V_{\mathrm{acc}} \cos\phi_0$$

and the relative energy deviation of an electron changes from $\delta_{\mathrm{E,i}} = \frac{\Delta E_{\mathrm{i}}}{E_{0,\mathrm{i}}}$ before acceleration to

$$\begin{aligned} \frac{\Delta E_{\mathrm{f}}}{E_{0,\mathrm{f}}} &= \frac{E_{0,\mathrm{i}}}{E_{0,\mathrm{f}}} \delta_{\mathrm{E,i}} - s_{\mathrm{i}} \frac{e_0 V_{\mathrm{acc}}}{E_{0,\mathrm{f}}} \frac{2\pi}{\lambda} \sin\phi_0 - s_{\mathrm{i}}^2 \frac{e_0 V_{\mathrm{acc}}}{E_{0,\mathrm{f}}} \frac{2\pi^2}{\lambda^2} \cos\phi_0 \\ &= A\delta_{\mathrm{E,i}} + B s_{\mathrm{i}} + C s_{\mathrm{i}}^2 \end{aligned} \tag{3.6}$$

Substituting equation (3.6) in (3.4) results in the second order dependence of the final position s_{f} of an electron on its initial position s_{i}:

$$s_{\mathrm{f}} = R_{56} A \delta_{\mathrm{E,i}} + R_{566} A^2 \delta_{\mathrm{E,i}}^2 + (1 + R_{56} B + 2R_{566} AB \delta_{\mathrm{E,i}}) s_{\mathrm{i}} + (R_{56} C + R_{566} B^2 + 2R_{566} AC \delta_{\mathrm{E,i}}) s_{\mathrm{i}}^2$$

Further simplifications can be made since $|\delta_{\mathrm{E,i}}\ A| << 1$ and $\left| \frac{R_{566}}{R_{56}} \right| \sim 1$:

$$s_{\mathrm{f}} \approx A R_{56} \delta_{\mathrm{E,i}} + (1 + B R_{56}) s_{\mathrm{i}} + (C R_{56} + B^2 R_{566}) s_{\mathrm{i}}^2 \tag{3.7}$$

As we will see later, the R_{56} is always negative[2] in magnetic chicanes and it is a good approximation to set $R_{566} = -\frac{3}{2} R_{56}$. Consequently, the effect of the second order terms of the transfer matrix and the curvature caused by the RF can only cancel when C is positive. That means $|\phi_0|$ has to be larger than $\pi/2$ and the beam would have to be decelerated to decrease the curvature in the longitudinal phase space. A better way to reduce the curvature and thus to reduce the achievable bunch length is to include an additional cavity that linearizes the phase space but leaves the mean energy almost unchanged. At TTF2 this will be done with a 3$^{\mathrm{rd}}$-harmonic cavity, i.e. a cavity with a frequency of 3.9 GHz [16].

Figure 3.3 shows the development of a bunch with a small curvature in the initial longitudinal phase space. During compression the longitudinal phase space folds over and most of the charge accumulates at the head of the bunch. The width of the resulting peak is mainly given by the uncorrelated energy spread.

Of main interest in bunch compressor chicanes are the final and the peak dispersion as well as the momentum compaction factor. Ideally, the dispersion should vanish behind the chicane, but in practice a small amount of residual dispersion often remains. The amount of the residual dispersion depends on the chicane geometry.

Assuming that the chicane is built of n magnets with bending angles $\alpha_1, \ldots, \alpha_n$ all orders of dispersion and momentum compaction can be defined as the coefficients of the

[2] In some publications the R_{56} is defined with a sign opposite to the definition in eqn. (3.1).

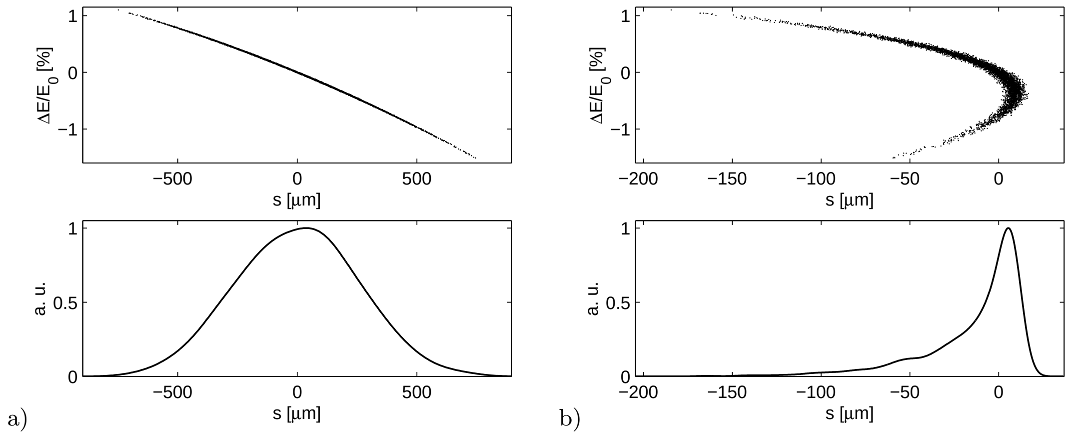

Figure 3.3: *The longitudinal phase space distribution and the charge profile are shown in front of the chicane (a) and behind it (b). Due to the small initial curvature the phase space distribution folds over during compression and a huge amount of charge accumulates at the head of the bunch.*

Taylor expansions of the transverse electron offset $x(\delta_\mathrm{E}, \alpha_1, \ldots, \alpha_n)$ and the path length $l(\delta_\mathrm{E}, \alpha_1, \ldots, \alpha_n)$ for small energy deviations $|\delta_\mathrm{E}| \ll 1$:

$$x(\delta_\mathrm{E}, \alpha_1, \ldots, \alpha_n) = x(0, \alpha_1, \ldots, \alpha_n) + R_{16}(\alpha_1, \ldots, \alpha_n)\delta_\mathrm{E} + R_{166}(\alpha_1, \ldots, \alpha_n)\delta_\mathrm{E}^2 + \ldots$$

and

$$l(\delta_\mathrm{E}, \alpha_1, \ldots, \alpha_n) = l(0, \alpha_1, \ldots, \alpha_n) + R_{56}(\alpha_1, \ldots, \alpha_n)\delta_\mathrm{E} + R_{566}(\alpha_1, \ldots, \alpha_n)\delta_\mathrm{E}^2 + \ldots$$

Following the definition of the coordinate system, the coordinates $x(0, \alpha_1, \ldots, \alpha_n)$ and $l(0, \alpha_1, \ldots, \alpha_n)$ are the coordinates of an electron that travels along the reference trajectory. Accordingly, they are both 0. Identifying the coefficients R_{m6} and R_{m66} with the coefficients from the general Taylor expansion

$$\begin{aligned} w(\delta_\mathrm{E}, \alpha_1, \ldots, \alpha_n) = w(0, \alpha_1, \ldots, \alpha_n) + \left.\frac{\partial w(\delta_\mathrm{E}, \alpha_1, \ldots, \alpha_n)}{\partial \delta_\mathrm{E}}\right|_{\delta_\mathrm{E}=0} \delta_\mathrm{E} \\ + \left.\frac{1}{2}\frac{\partial^2 w(\delta_\mathrm{E}, \alpha_1, \ldots, \alpha_n)}{\partial \delta_\mathrm{E}^2}\right|_{\delta_\mathrm{E}=0} \delta_\mathrm{E}^2 + \ldots \end{aligned}$$

we get

$$R_{m6}(\alpha_1, \ldots, \alpha_n) = \left.\frac{\partial w(\delta_\mathrm{E}, \alpha_1, \ldots, \alpha_n)}{\partial \delta_\mathrm{E}}\right|_{\delta_\mathrm{E}=0} \tag{3.8}$$

$$R_{m66}(\alpha_1, \ldots, \alpha_n) = \left.\frac{1}{2}\frac{\partial^2 w(\delta_\mathrm{E}, \alpha_1, \ldots, \alpha_n)}{\partial \delta_\mathrm{E}^2}\right|_{\delta_\mathrm{E}=0} \tag{3.9}$$

$$\ldots$$

Here m stands for 1 or 5 and w for x or l. $x(\delta_\mathrm{E}, \alpha_1, \ldots, \alpha_n)$ and $l(\delta_\mathrm{E}, \alpha_1, \ldots, \alpha_n)$ are given by the chicane geometry. In some cases one can also avoid the introduction of the dependence on δ_E in $x(\alpha_1, \ldots, \alpha_n)$ and $l(\alpha_1, \ldots, \alpha_n)$ and calculate the elements $R_{m6}(\alpha), R_{m66}(\alpha), \ldots$ recursively by using the following formula:

$$R_{m6}^{(n)}(\alpha) = -\frac{n-1}{n} R_{m6}^{(n-1)}(\alpha) - \frac{1}{n} \tan\alpha \left.\frac{\partial R_{m6}^{(n-1)}(\alpha^*)}{\partial \alpha^*}\right|_{\alpha^*=\alpha} \tag{3.10}$$

For convenience I introduced the index $n = 1, 2, \ldots$ that denotes the order of the matrix element, i.e. $R^{(0)}_{m6}(\alpha) = w(\alpha)$, $R^{(1)}_{m6}(\alpha) = R_{m6}(\alpha)$, $R^{(2)}_{m6}(\alpha) = R_{m66}(\alpha), \ldots$. For a derivation of formula (3.10) see appendix A.

The chicane layouts compared for BC3 are the usual 4-bend chicanes, which I will call C-chicanes throughout my thesis, and S-shaped chicanes. These are sometimes called one-period wigglers in other publications, but I will call them S-chicanes. Both types can be symmetric or asymmetric. In the symmetric cases the bending angles of all magnets are the same and the outer drift spaces have the same length (figures 3.4a and c). The lengths of the first and the last drift space differ in the asymmetric C-chicane. The first two dipoles then have a different bending angle than the last two dipoles (figure 3.4b). At the Low Energy Undulator Test Line (LEUTL) in Argonne, USA, such a chicane was built [34]. In an S-chicane it is possible to break the symmetry without changing the bending angle α of the dipoles. Starting from the symmetric S-chicane the central magnets have to be shifted under the angle α with respect to the Z-axis, i.e. they are not just longitudinally shifted but also transversely. Literally speaking, they are shifted along the electron path in the outer drift spaces (figure 3.4d). Another way to introduce an asymmetry in the S-chicanes is to keep the lengths of the drift spaces[3] constant, but to change the transverse position of the central dipoles. In this case the bending angles of the dipoles change (figure 3.4e). Of course combinations of these two cases are possible, but they are not considered within this thesis. In the S-chicanes one can also split the central dipoles. This leads to 6-bend S-chicanes which have some practical advantages (figure 3.4f).

Since I neglect the influence of synchrotron radiation on beam dynamics in this chapter all these layouts only differ in the amount of the residual dispersion and the size of the bending angles which are needed to reach a certain R_{56}. The main differences between the layouts will become evident when synchrotron radiation is included as we will see in chapter 4. There we will also see why it might be preferable to build S-chicanes or asymmetric chicanes.

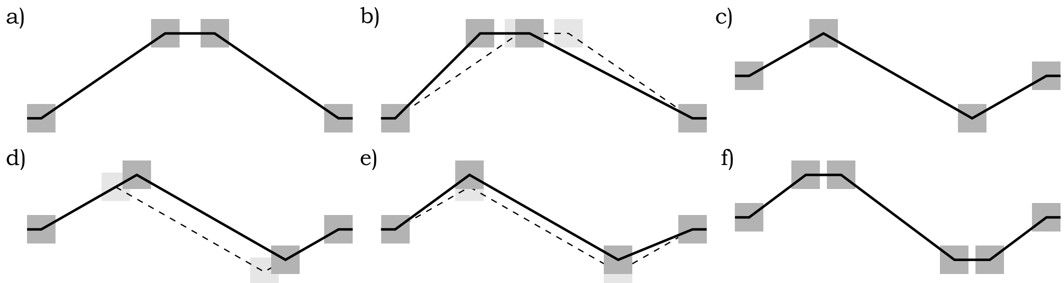

Figure 3.4: *Different bunch compressor chicanes have been compared for BC3. The symmetric C-chicane with four dipoles of the same strength is sketched in a). In the asymmetric C-chicane the first two dipoles have a strength different from the last two dipoles (b). The symmetric S-chicane (c) can be modified in two ways: by changing the outer drift lengths but keeping the bending angles (d) or by changing the angles but keeping the drift lengths (e). The central dipoles of an S-chicane can be split into pairs of dipoles (f).*

[3] Throughout my thesis the length of a drift space is always the length along the Z-axis, i.e. it is independent of the bending angle.

3.2 Momentum-dependence of the Particle Trajectories in C-Chicanes

Behind a bunch compressor chicane the dispersion should vanish. This means, that behind a magnetic chicane the mean transverse bunch offset $\langle X \rangle$ and its mean angle $\langle X' \rangle$ in the laboratory frame must vanish[4]. This limits the freedom of choice for the bending angles of the magnets and the lengths of the drift spaces. Additionally, I assume that the central drift space of the C-chicane is parallel to the Z-axis.

Electrons with nominal energy E_0 are deflected in dipole 1 and dipole 2 by the angles α_1 and $-\alpha_1$. In dipole 3 and dipole 4 they are deflected by the angles $-\alpha_2$ and α_2. Electrons with a small energy deviation are deflected by slightly different angles $\frac{\sin\alpha_1}{1+\delta_E}$ and $\frac{\sin\alpha_2}{1+\delta_E}$. The drift space between the first two dipoles has the length L_{12}. The drift space between the last two dipoles has the length L_{34}. The drift space L_{23} between dipole 2 and dipole 3 does not contribute to the transverse offset and the dispersion. The length of the bending magnets is L_B (figure 3.5).

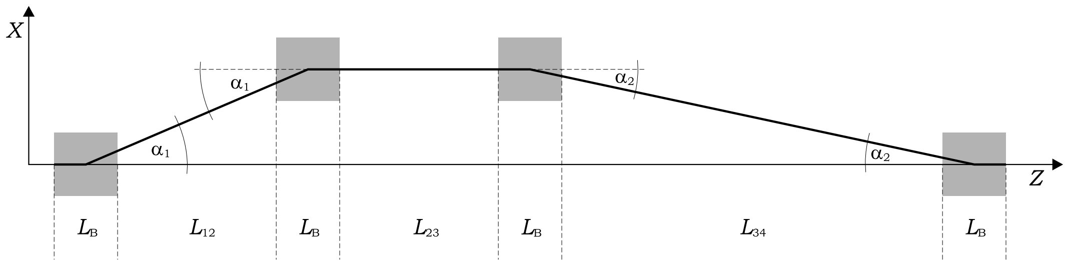

Figure 3.5: *The C-chicane is sketched. It is assumed that the central drift is parallel to the Z-axis and that all magnets have the same length.*

An electron with nominal energy travels on the reference trajectory. In the laboratory frame it will have a final transverse offset of

$$X_f = 2L_B \tan\frac{\alpha_1}{2} + L_{12}\tan\alpha_1 - 2L_B\tan\frac{\alpha_2}{2} - L_{34}\tan\alpha_2 \tag{3.11}$$

Since $X_f \stackrel{!}{=} 0$ the dependence of α_2 on α_1 can be calculated by solving

$$2L_B \tan\frac{\alpha_1}{2} + L_{12}\tan\alpha_1 = 2L_B\tan\frac{\alpha_2}{2} + L_{34}\tan\alpha_2$$

for α_2. Unfortunately, due to the occurrence of $\tan\frac{\alpha_2}{2}$ and $\tan\alpha_2$ this is analytically not possible. But since α_1 and α_2 are usually small and close to each other we can approximate the functions $2\tan\frac{\alpha}{2}$ by $\tan\alpha$ on both sides and get

$$(L_B + L_{12})\tan\alpha_1 \approx (L_B + L_{34})\tan\alpha_2$$

what is easy to solve:

$$\alpha_2(\alpha_1) \approx \arctan\left(\frac{L_B + L_{12}}{L_B + L_{34}}\tan\alpha_1\right) \tag{3.12}$$

For an electron with a small energy deviation the final transverse electron offset x_f in the moving frame is energy dependent. It is the sum of the offsets accumulated in the

[4] I also assume that $\langle X \rangle$ and $\langle X' \rangle$ of the incoming bunch are both zero.

different parts (dipoles and drifts) of the chicane:

$$x_\mathrm{f}(\delta_\mathrm{E},\alpha_1,\alpha_2) = 2L_\mathrm{B}\tan\frac{\arcsin\left(\frac{\sin\alpha_1}{1+\delta_\mathrm{E}}\right)}{2} + L_{12}\tan\arcsin\left(\frac{\sin\alpha_1}{1+\delta_\mathrm{E}}\right)$$
$$- 2L_\mathrm{B}\tan\frac{\arcsin\left(\frac{\sin\alpha_2}{1+\delta_\mathrm{E}}\right)}{2} - L_{34}\tan\arcsin\left(\frac{\sin\alpha_2}{1+\delta_\mathrm{E}}\right) - X_\mathrm{f}(\alpha_1,\alpha_2) \quad (3.13)$$

Making use of formulae (3.8) and (3.9) the first and second order dispersion can be calculated. They result in

$$R_{16}(\alpha_1,\alpha_2) = -2\frac{L_\mathrm{B}\tan\frac{\alpha_1}{2}}{\cos\alpha_1} - \frac{L_{12}\tan\alpha_1}{(\cos\alpha_1)^2} + 2\frac{L_\mathrm{B}\tan\frac{\alpha_2}{2}}{\cos\alpha_2} + \frac{L_{34}\tan\alpha_2}{(\cos\alpha_2)^2} \quad (3.14)$$

and

$$R_{166}(\alpha_1,\alpha_2) = \frac{(2L_\mathrm{B}-L_{12})\tan\alpha_1}{2\,(\cos\alpha_1)^2} + \frac{3L_{12}\tan\alpha_1}{2\,(\cos\alpha_1)^4} - \frac{(2L_\mathrm{B}-L_{34})\tan\alpha_2}{2\,(\cos\alpha_2)^2} - \frac{3L_{34}\tan\alpha_2}{2\,(\cos\alpha_2)^4} \quad (3.15)$$

To simplify equations (3.11), (3.14) and (3.15) α_2 is replaced by equation (3.12) and then the equations are expanded to third order in α_1:

$$X_\mathrm{f}(\alpha_1) \approx \frac{L_\mathrm{B}}{4}\left(\frac{(L_{12}+L_\mathrm{B})^3}{(L_{34}+L_\mathrm{B})^3} - 1\right)\alpha_1^3 \quad (3.16)$$

$$R_{16}(\alpha_1) \approx \left(\frac{(L_{12}+L_\mathrm{B})^3}{(L_{34}+L_\mathrm{B})^3}(\frac{L_\mathrm{B}}{4}+L_{34}) - (\frac{L_\mathrm{B}}{4}+L_{12})\right)\alpha_1^3 \quad (3.17)$$

$$R_{166}(\alpha_1) \approx \left(\frac{(L_{12}+L_\mathrm{B})^3}{(L_{34}+L_\mathrm{B})^3}(L_\mathrm{B}+\frac{5}{2}L_{34}) - (L_\mathrm{B}+\frac{5}{2}L_{12})\right)\alpha_1^3 \quad (3.18)$$

Now it is easy to see that in asymmetric C-chicanes the transverse bunch offset and the first order dispersion usually do not vanish at the same time. Also the higher orders of dispersion are never cancelled completely. Only in symmetric C-chicanes where $\alpha_1 = \alpha_2$ and $L_{12} = L_{34}$ the final bunch offset and all orders of dispersion are always 0. In other words, only the symmetric C-chicane is achromatic. The fact that X_f is not exactly 0 in equation (3.16) is an expression of the error made by the approximation in (3.12).

When inserting typical values $L_\mathrm{B} = 0.5$ m, $L_{12} = 5.15$ m, $L_{34} = 6.35$ m, $\alpha_1 = 4.0°$ the momentum compaction factor is $R_{56} = -4.9$ cm and the residual dispersion is $R_{16} = -0.46$ mm. A similar amount of dispersion would be produced by a longitudinal dipole alignment error of some millimeters. Since the alignment error is usually about a tenth of a millimeter the residual dispersion behind symmetric C-chicanes will be about an order of magnitude smaller. This is a great advantage of the symmetric C-chicane in comparison to the asymmetric design.

The influence of the approximation made in equation (3.12) on the dispersion can be estimated by comparing the results from the approximated functions with numerical solutions. For the parameters given above, the relative error due to the approximation is found to be of the order of some percent.

The transverse bunch offset and the dispersion reach their maximum absolute values

$$X_\mathrm{m}(\alpha_1) = 2L_\mathrm{B}\tan\frac{\alpha_1}{2} + L_{12}\tan\alpha_1 \approx (L_{12}+L_\mathrm{B})\alpha_1 + \left(\frac{L_{12}}{3}+\frac{L_\mathrm{B}}{12}\right)\alpha_1^3 \quad (3.19)$$

and

$$R_{16,\mathrm{m}}(\alpha_1,\alpha_2) = -2\frac{L_\mathrm{B}\tan\frac{\alpha_1}{2}}{\cos\alpha_1} - \frac{L_{12}\tan\alpha_1}{(\cos\alpha_1)^2} \approx -(L_{12}+L_\mathrm{B})\alpha_1 - \left(\frac{4L_{12}}{3}+\frac{7L_\mathrm{B}}{12}\right)\alpha_1^3 \quad (3.20)$$

between the second and the third dipole

To calculate the momentum compaction factors R_{56} and R_{566} behind the C-chicane we have to repeat the same steps as for the dispersion calculation. The only difference is that we need the path length $l_\mathrm{f}(\delta_\mathrm{E})$ instead of the final transverse electron offset $x_\mathrm{f}(\delta_\mathrm{E})$. Also the path length can easily be derived from the chicane geometry. The total length of the reference trajectory is:

$$L_\mathrm{f}(\alpha_1,\alpha_2) = 2L_\mathrm{B}\frac{\alpha_1}{\sin\alpha_1} + \frac{L_{12}}{\sqrt{1-(\sin\alpha_1)^2}} + L_{23} + 2L_\mathrm{B}\frac{\alpha_2}{\sin\alpha_2} + \frac{L_{34}}{\sqrt{1-(\sin\alpha_2)^2}} \quad (3.21)$$

and the total path length of an electron with a small energy deviation is

$$\begin{aligned} l_\mathrm{f}(\delta_\mathrm{E},\alpha_1,\alpha_2) = {} & 2L_\mathrm{B}\arcsin\left(\frac{\sin\alpha_1}{1+\delta_\mathrm{E}}\right)\frac{1+\delta_\mathrm{E}}{\sin\alpha_1} + \frac{L_{12}}{\sqrt{1-\left(\frac{\sin\alpha_1}{1+\delta_\mathrm{E}}\right)^2}} + L_{23} \\ & + 2L_\mathrm{B}\arcsin\left(\frac{\sin\alpha_2}{1+\delta_\mathrm{E}}\right)\frac{1+\delta_\mathrm{E}}{\sin\alpha_2} + \frac{L_{34}}{\sqrt{1-\left(\frac{\sin\alpha_2}{1+\delta_\mathrm{E}}\right)^2}} - L_\mathrm{f}(\alpha_1,\alpha_2) \end{aligned}$$

First and second order momentum compaction factors can be calculated from formulae (3.8) and (3.9). After including (3.12) third order expansions of $L_\mathrm{f}(\alpha_1)$, $R_{56}(\alpha_1)$ and $R_{566}(\alpha_1)$ result in:

$$L_\mathrm{f}(\alpha_1) \approx (L_{12}+L_{23}+L_{34}+4L_\mathrm{B}) + \frac{1}{6}\left(3L_{12}+2L_\mathrm{B}+\frac{(L_{12}+L_\mathrm{B})^2(3L_{34}+2L_\mathrm{B})}{(L_{34}+L_\mathrm{B})^2}\right)\alpha_1^2 \quad (3.22)$$

$$R_{56}(\alpha_1) \approx -\frac{1}{3}\left(3L_{12}+2L_\mathrm{B}+\frac{(L_{12}+L_\mathrm{B})^2(3L_{34}+2L_\mathrm{B})}{(L_{34}+L_\mathrm{B})^2}\right)\alpha_1^2 \quad (3.23)$$

$$R_{566}(\alpha_1) \approx \frac{1}{2}\left(3L_{12}+2L_\mathrm{B}+\frac{(L_{12}+L_\mathrm{B})^2(3L_{34}+2L_\mathrm{B})}{(L_{34}+L_\mathrm{B})^2}\right)\alpha_1^2 \approx -\frac{3}{2}R_{56} \quad (3.24)$$

The third order terms of the expansions vanish. Thus, the total length of the reference trajectory and the momentum compaction factors depend only to second order on the bending angle α_1. In all practical cases it is sufficient to set $R_{566} = -\frac{3}{2}R_{56}$.

3.3 Momentum-dependence of the Particle Trajectories in S-Chicanes

Two different asymmetric 6-bend S-chicanes are described here. In the first case the bending angles in all dipoles are assumed to have the same value but the lengths of the outer drifts differ. For the second case the bending angles differ but the lengths of the outer drift spaces are the same. The symmetric S-chicane can be derived from both cases. The length of the central drift space remains constant for all cases. The formulae for offset, path length, dispersion and momentum compaction factors are first derived for a general case and later simplified.

The bending angles of the first and the second dipole are α_1 and $-\alpha_1$. They are separated by the drift space L_{12}. The third and fourth dipole have the bending angles

$-\alpha_2$ and α_2 and their separation is L_{34}. The bending angles of the fifth and sixth dipole are α_3 and $-\alpha_3$ and they are separated by the drift space L_{56}. The length of all dipoles is L_B. The drift spaces between dipoles 2 and 3 and between dipoles 4 and 5 have the lengths L_{23} and L_{45} respectively. They are parallel to the Z-axis and do not contribute to offset and dispersion (figure 3.6).

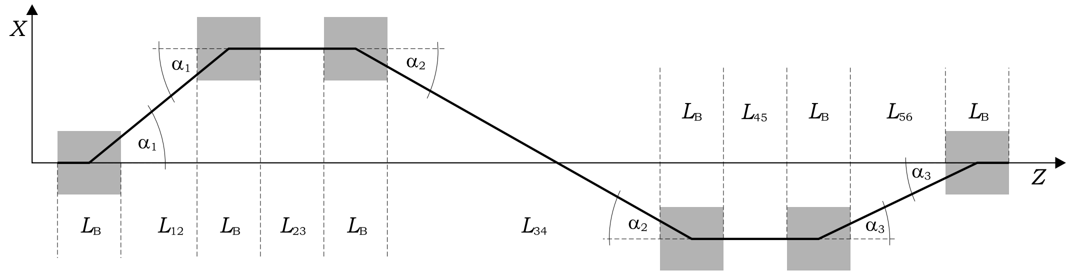

Figure 3.6: *The 6-bend S-chicane is sketched. It is assumed that all magnets have the same length. The drifts between dipole 2 and 3 as well as between dipole 4 and 5 are parallel to the Z-axis.*

As before, I assume that, in the laboratory frame, the mean transverse bunch offset $\langle X \rangle$ and the mean angle $\langle X' \rangle$ vanish both in front of and behind the chicane. Therefore drift lengths and bending angles depend on each other. For the symmetric 6-bend S-chicane the final transverse bunch offset X_f in the laboratory frame is:

$$X_f(\alpha) = 2L_B \tan\frac{\alpha}{2} + (L_{12} - L_{34} + L_{56}) \tan\alpha$$

Since $X_f \overset{!}{=} 0$ for a nominal bending angle α_0 the required length L_{34} of the central drift space can be calculated:

$$L_{34} = L_{12} + L_{56} + 2L_B \frac{\tan\frac{\alpha_0}{2}}{\tan\alpha_0} \tag{3.25}$$

For a general 6-bend S-chicane we get from simple geometric considerations the energy dependence of the final transverse electron offset:

$$\begin{aligned} x_f(\delta_E, \alpha_1, \alpha_2, \alpha_3) = -X_f(\alpha_1, \alpha_2, \alpha_3) &+ 2L_B \tan\frac{\arcsin\left(\frac{\sin\alpha_1}{1+\delta_E}\right)}{2} + L_{12}\tan\arcsin\left(\frac{\sin\alpha_1}{1+\delta_E}\right) \\ &- 2L_B \tan\frac{\arcsin\left(\frac{\sin\alpha_2}{1+\delta_E}\right)}{2} - L_{34}\tan\arcsin\left(\frac{\sin\alpha_2}{1+\delta_E}\right) \\ &+ 2L_B \tan\frac{\arcsin\left(\frac{\sin\alpha_3}{1+\delta_E}\right)}{2} + L_{56}\tan\arcsin\left(\frac{\sin\alpha_3}{1+\delta_E}\right) \end{aligned} \tag{3.26}$$

The first order dispersion is given by (3.8):

$$\begin{aligned} R_{16}(\alpha_1, \alpha_2, \alpha_3) = &-2\frac{L_B \tan\frac{\alpha_1}{2}}{\cos\alpha_1} - \frac{L_{12}\tan\alpha_1}{(\cos\alpha_1)^2} \\ &+2\frac{L_B \tan\frac{\alpha_2}{2}}{\cos\alpha_2} + \frac{L_{34}\tan\alpha_2}{(\cos\alpha_2)^2} \\ &-2\frac{L_B \tan\frac{\alpha_3}{2}}{\cos\alpha_3} - \frac{L_{56}\tan\alpha_3}{(\cos\alpha_3)^2} \end{aligned} \tag{3.27}$$

And the second order dispersion is given by (3.9):

$$R_{166}(\alpha_1,\alpha_2,\alpha_3) = \frac{(2L_\mathrm{B}-L_{12})\tan\alpha_1}{2(\cos\alpha_1)^2} + \frac{3L_{12}\tan\alpha_1}{2(\cos\alpha_1)^4} - \frac{(2L_\mathrm{B}-L_{34})\tan\alpha_2}{2(\cos\alpha_2)^2} - \frac{3L_{34}\tan\alpha_2}{2(\cos\alpha_2)^4} + \frac{(2L_\mathrm{B}-L_{56})\tan\alpha_3}{2(\cos\alpha_3)^2} + \frac{3L_{56}\tan\alpha_3}{2(\cos\alpha_3)^4} \tag{3.28}$$

These formulae are valid for all types of 6-bend S-chicanes which I consider in my thesis. The two asymmetric cases are just simplifications of the general formulae. For the first asymmetric case I assume that all bending angles are the same, i.e. $\alpha_1=\alpha_2=\alpha_3$:

$$x_\mathrm{f}(\alpha_1) = 2L_\mathrm{B}\tan\frac{\alpha_1}{2} + (L_{12}-L_{34}+L_{56})\tan\alpha_1$$

$$R_{16}(\alpha_1) = -\frac{2L_\mathrm{B}\tan\frac{\alpha_1}{2}}{\cos\alpha_1} + (L_{12}-L_{34}+L_{56})\frac{\tan\alpha_1}{(\cos\alpha_1)^2}$$

$$R_{166}(\alpha_1) = \frac{\tan\alpha_1}{2(\cos\alpha_1)^2}\left(2L_\mathrm{B}-L_{12}+L_{34}-L_{56}+3(L_{12}-L_{34}+L_{56})\frac{1}{(\cos\alpha_1)^2}\right)$$

After replacing L_{34} by eqn. (3.25) in the equations for X_f, R_{16} and R_{166} they can be approximated to third order for small angles α_1 and α_0:

$$X_\mathrm{f}(\alpha_1) \approx -\frac{1}{4}L_\mathrm{B}\alpha_1^3 + \frac{1}{4}L_\mathrm{B}\alpha_1\alpha_0^2 \tag{3.29}$$

$$R_{16}(\alpha_1) \approx \frac{3}{4}L_\mathrm{B}\alpha_1^3 - \frac{1}{4}L_\mathrm{B}\alpha_1\alpha_0^2 \tag{3.30}$$

$$R_{166}(\alpha_1) \approx -\frac{3}{2}L_\mathrm{B}\alpha_1^3 + \frac{1}{4}L_\mathrm{B}\alpha_1\alpha_0^2 \tag{3.31}$$

We can see that the final transverse bunch offset and the dispersion do not depend on the lengths of the outer drift spaces. That means, if the bending angles stay constant one can move the central magnets without changing the final properties of the chicane. Additionally, one can see that there is always a certain amount of residual dispersion left even in a symmetric S-chicane. Thus, an S-chicane is never achromatic. Since the length of the central drift L_{34} is adjusted for a nominal angle α_0 the residual bunch offset and the dispersion will change if the bending angles of the dipoles change. This will happen for example in a chicane like BC3 where it is required to run with different bending angles (see chapter 6). For example, if the dipoles have a length of $L_\mathrm{B}=0.5\,\mathrm{m}$ and L_{34} is chosen for $\alpha_0=3.85°$ the transverse bunch offset will be $X_\mathrm{f}=-50\,\mu\mathrm{m}$ if $\alpha_1=5.4°$.

The second type of asymmetry in an S-chicane is achieved when different bending angles $\alpha_1\neq\alpha_2\neq\alpha_3$ for the first, second and third dipole pair are used. The drift spaces have the same lengths as in the symmetric case, i.e. $L_{12}=L_{56}$ and $L_{34}=L_{12}+L_{56}+2L_\mathrm{B}\frac{\tan(\alpha_0/2)}{\tan\alpha_0}$.

Obviously, the bending angles are not independent of each other. From geometric considerations we get $\alpha_1\approx\arctan(\frac{\Delta h}{L_{12}+L_\mathrm{B}}+\tan\alpha_2)$ and $\alpha_3\approx\arctan(-\frac{\Delta h}{L_{12}+L_\mathrm{B}}+\tan\alpha_2)$. Δh is the change of the transverse position of the central dipoles. For small angles and small offsets we get:

$$X_\mathrm{f}(\alpha_2) \approx -\frac{1}{4}L_\mathrm{B}\alpha_2^3 + \frac{1}{4}L_\mathrm{B}\alpha_2\alpha_0^2 - \frac{3L_\mathrm{B}}{2(L_{12}+L_\mathrm{B})^2}\Delta h^2\alpha_2 \tag{3.32}$$

$$R_{16}(\alpha_2) \approx \frac{3}{4}L_\mathrm{B}\alpha_2^3 - \frac{1}{4}L_\mathrm{B}\alpha_2\alpha_0^2 - \frac{3L_\mathrm{B}+12L_{12}}{2(L_{12}+L_\mathrm{B})^2}\Delta h^2\alpha_2 \tag{3.33}$$

$$R_{166}(\alpha_2) \approx -\frac{3}{2}L_{\mathrm{B}}\alpha_2^3 + \frac{1}{4}L_{\mathrm{B}}\alpha_2\alpha_0^2 + \frac{6L_{\mathrm{B}}+15L_{12}}{(L_{12}+L_{\mathrm{B}})^2}\Delta h^2\alpha_2 \tag{3.34}$$

Again the final bunch offset and the dispersion show a third order dependence on the bending angle. But this time they also depend to second order on the transverse displacement of the dipoles. This is a major difference to the first asymmetric case where no dependence on the dipole displacement was found.

In an S-chicane transverse bunch offset and dispersion each have two local extrema. They are located between the second and third dipole and between the fourth and fifth dipole. The first extreme values are

$$X_{\mathrm{m1}}(\alpha_1) = 2L_{\mathrm{B}}\tan\frac{\alpha_1}{2} + L_{12}\tan\alpha_1\ , \tag{3.35}$$

$$R_{16,\mathrm{m1}}(\alpha_1) = -2\frac{L_{\mathrm{B}}\tan\frac{\alpha_1}{2}}{\cos\alpha_1} - \frac{L_{12}\tan\alpha_1}{(\cos\alpha_1)^2} \tag{3.36}$$

and the second extreme values are

$$X_{\mathrm{m2}}(\alpha_1,\alpha_2) = 2L_{\mathrm{B}}\tan\frac{\alpha_1}{2} + L_{12}\tan\alpha_1 - 2L_{\mathrm{B}}\tan\frac{\alpha_2}{2} - L_{34}\tan\alpha_2 \tag{3.37}$$

$$R_{16,\mathrm{m2}}(\alpha_1,\alpha_2) = -2\frac{L_{\mathrm{B}}\tan\frac{\alpha_1}{2}}{\cos\alpha_1} - \frac{L_{12}\tan\alpha_1}{(\cos\alpha_1)^2} + 2\frac{L_{\mathrm{B}}\tan\frac{\alpha_2}{2}}{\cos\alpha_2} + \frac{L_{34}\tan\alpha_2}{(\cos\alpha_2)^2} \tag{3.38}$$

The first and second order momentum compaction factors can be derived from the path length l_{f} by making use of equations (3.8) and (3.9). In general the energy dependent path length l_{f} is

$$\begin{aligned} l_{\mathrm{f}}(\delta_{\mathrm{E}},\alpha_1,\alpha_2,\alpha_3) = {} & 2L_{\mathrm{B}}\arcsin\left(\frac{\sin\alpha_1}{1+\delta_{\mathrm{E}}}\right)\frac{1+\delta_{\mathrm{E}}}{\sin\alpha_1} + \frac{L_{12}}{\sqrt{1-\left(\frac{\sin\alpha_1}{1+\delta_{\mathrm{E}}}\right)^2}} + L_{23} \\ & + 2L_{\mathrm{B}}\arcsin\left(\frac{\sin\alpha_2}{1+\delta_{\mathrm{E}}}\right)\frac{1+\delta_{\mathrm{E}}}{\sin\alpha_2} + \frac{L_{34}}{\sqrt{1-\left(\frac{\sin\alpha_2}{1+\delta_{\mathrm{E}}}\right)^2}} + L_{45} \\ & + 2L_{\mathrm{B}}\arcsin\left(\frac{\sin\alpha_3}{1+\delta_{\mathrm{E}}}\right)\frac{1+\delta_{\mathrm{E}}}{\sin\alpha_3} + \frac{L_{56}}{\sqrt{1-\left(\frac{\sin\alpha_3}{1+\delta_{\mathrm{E}}}\right)^2}} - L_{\mathrm{f}} \end{aligned}$$

where

$$\begin{aligned} L_{\mathrm{f}}(\alpha_1,\alpha_2,\alpha_3) = {} & 2L_{\mathrm{B}}\frac{\alpha_1}{\sin\alpha_1} + \frac{L_{12}}{\sqrt{1-(\sin\alpha_1)^2}} + L_{23} + 2L_{\mathrm{B}}\frac{\alpha_2}{\sin\alpha_2} + \frac{L_{34}}{\sqrt{1-(\sin\alpha_2)^2}} + L_{45} \\ & + 2L_{\mathrm{B}}\frac{\alpha_3}{\sin\alpha_3} + \frac{L_{56}}{\sqrt{1-(\sin\alpha_2)^2}} \end{aligned}$$

is the length of the reference trajectory. Again L_{34} is replaced by (3.25) and the resulting equations are expanded. For the first asymmetric case the third order expansions are

$$L_{\mathrm{f}}(\alpha_1) \approx 2L_{12} + L_{23} + L_{45} + 2L_{56} + 7L_{\mathrm{B}} - \frac{1}{4}L_{\mathrm{B}}\alpha_{1,0}^2 + (L_{12} + L_{56} + \frac{3}{2}L_{\mathrm{B}})\alpha_1^2 \tag{3.39}$$

$$R_{56}(\alpha_1) \approx -(2L_{12} + 2L_{56} + 3L_{\mathrm{B}})\alpha_1^2 \tag{3.40}$$

$$R_{566}(\alpha_1) \approx (3L_{12} + 3L_{56} + \frac{9}{2}L_{\mathrm{B}})\alpha_1^2 = -\frac{3}{2}R_{56} \tag{3.41}$$

The third order terms of the expansion vanish. As before we can see that the final properties of the chicane remain unchanged when shifting the central magnets. In contrast to the dispersion the momentum compaction factors depend weakly on the nominal angle α_0 for which the length of the central drift is adjusted.

For the second asymmetric case the expansions result in:

$$L_\mathrm{f}(\alpha_2) \approx (4L_{12}+L_{23}+L_{45}+7L_\mathrm{B})-\frac{L_\mathrm{B}}{4}\alpha_{1,0}+\left(2L_{12}+\frac{3L_\mathrm{B}}{2}\right)\alpha_2^2+\frac{3L_{12}+2L_\mathrm{B}}{3(L_{12}+L_\mathrm{B})^2}\Delta h^2 \quad (3.42)$$

$$R_{56}(\alpha_2) \approx -\frac{6L_{12}+4L_\mathrm{B}}{3(L_{12}+L_\mathrm{B})^2}\Delta h^2-(4L_{12}+3L_\mathrm{B})\alpha_2^2 \quad (3.43)$$

$$R_{566}(\alpha_2) \approx \frac{3L_{12}+2L_\mathrm{B}}{(L_{12}+L_\mathrm{B})^2}\Delta h^2-(6L_{12}+\frac{9}{2}L_\mathrm{B})\alpha_2^2=-\frac{3}{2}R_{56} \quad (3.44)$$

The quadratic dependence on the vertical displacement already found for the dispersion is also found for the momentum compaction factors. Also the relation $R_{566} = -\frac{3}{2}R_{56}$ is confirmed.

For the estimation of the residual dispersion only two cases have to be compared. The symmetric S-chicane and the asymmetric S-chicane with modified angles. We have seen before that shifting the inner magnets but keeping the bending angles constant does not change offset and dispersion. The length of all dipoles is $L_\mathrm{B} = 0.5$ m and their bending angle is $\alpha = 3.8^\circ$ for the symmetric case. For the asymmetric case only the two central dipoles deflect the bunch by this angle. The first drift has the length $L_{12} = 2.375$ m. All other parameters depend on these values or are irrelevant. It is assumed that the length of the central drift is adjusted for the bending angle $\alpha_0 = \alpha$. For the asymmetric chicane, the transverse dipole shift is $\Delta h = 0.02$ m. When these values are substituted, the transverse bunch offset vanishes behind the symmetric S-chicane and the residual dispersion is $R_{16} = 0.073$ mm. For the asymmetric S-chicane the final offset is just $2.4\,\mu$m and the residual dispersion is $R_{16} = 0.025$ mm. The momentum compaction factor is in both cases $R_{56} = -4.9$ cm.

Taking into account longitudinal misalignments of the dipoles, terms linear in bending angle and displacement have to be added. Misalignments are normally of the order of some 0.1 mm and therefore contribute to the offset and the dispersion at a comparable level. One can conclude that even the asymmetric S-chicanes will produce a negligible amount of residual offset and dispersion. In contrast to this, we have seen that in an asymmetric C-chicane with the same R_{56} a residual dispersion is generated that is about an order of magnitude higher and therefore not negligible. This looks like a profound difference between C-chicanes and S-chicanes, but it has a simple explanation. The shift of the central dipoles in the C-chicane has to be a lot larger than in the S-chicane to reach a similar change in bending angle. Since the bending angles are very small they are more sensitive to transverse shifts than to longitudinal shifts. For the cases compared here the transverse shift of the four central dipoles in the S-chicane is just 2 cm but the longitudinal shift of the two central dipoles in the C-chicane is 60 cm.

Chapter 4

Bunch Self Interaction due to Synchrotron Radiation, Space Charge and Wake Fields

In the previous chapter I discussed the motion of electrons in external electric and magnetic fields. Unfortunately, the electrons which pass a bunch compressor chicane also produce strong electromagnetic fields themselves. These fields are the space charge fields that are of course always present in bunches of charged particles, and the synchrotron radiation fields that are emitted in the bending magnets.

The electric and magnetic components of the space charge fields exert forces on the electrons which compensate each other better when the energy increases. Consequently, for ultra-relativistic beams it is usually safe to neglect the influence of the space charge forces. To drive FELs, on the other hand, a very high charge density is needed and the space charge forces might still lead to a noticeable emittance growth even of ultra-relativistic bunches. The influence of the space charge fields is the reason why bunch compressors should not be located in the low energy part of a linac. As was pointed out in [35] space charge fields can also lead to an amplification of small density modulations. This effect is different from the CSR microbunch instability which is studied in chapter 7. The amplification develops in long beam lines and is not an issue specifically related to bunch compressors. It is not studied within this thesis.

The electromagnetic fields generated by the electrons interact with the conducting walls of the vacuum chamber. Thus, one also has to consider the effect of resistive wall wake fields and surface roughness wake fields as well as the shielding of the low frequency part of the synchrotron radiation spectrum due to the chamber. Furthermore steps and tapers in the cross section of the chamber can have an influence on the fields.

All these effects lead to an overall energy loss of the bunch and to a nonuniform energy distribution inside the bunch. A uniform energy loss is not a major concern. The nonuniform energy distribution, however, will dilute the transverse emittance of the bunch due to the dispersive effects in the chicane. In the first section of this chapter I define the different transverse emittances which are used in this thesis.

The synchrotron radiation which is emitted in the bending magnets can lead to a strong tail-head interaction of the electrons inside the bunch. The radiation power and its spectrum depend not only on the bunch length, the charge and the energy but also on the deflection strength in the magnets. In section 4.2 I will recapitulate the main aspects of the synchrotron radiation emitted by a bunch of electrons passing a single bending magnet. For simplicity I first neglect the development of the fields in magnets of finite length and will only discuss the steady-state radiation of electrons in circular motion [36, 37, 38]. The development of the CSR fields along the magnet is taken into account later. A detailed analysis of the radiation of electrons passing a bending magnet of finite length is given in [39].

Section 4.3 explains some features of the dynamics of a bunch passing a magnetic chicane under the influence of CSR fields. In this context one also has to be aware of the fact that the radiation emitted inside the magnets can travel through the vacuum chambers and might interact with the bunch in the drift spaces where no new radiation is emitted.

In section 4.4 the influence of the vacuum chamber on the emission of the synchrotron radiation is explained. The shielding due to the vacuum chamber suppresses the low frequency part of the spectrum and thus reduces the total radiation power. This positive effect increases when the chamber becomes narrower. Unfortunately, the negative effect of the wake fields becomes more important in narrow chambers. Some basic aspects of wake fields are discussed in section 4.5.

4.1 Definition of the Transverse Emittance

In general the transverse emittance is given by the transverse phase space coordinates x and x' of the particles in a bunch:

$$\varepsilon_{\mathrm{x}} = \sqrt{\langle x^2 \rangle \langle x'^2 \rangle - \langle x\, x' \rangle^2}$$

It is a measure of the area occupied by the particles in transverse phase space. Usually, the emittance is normalized to remove the energy dependence: $\varepsilon_{\mathrm{x,n}} = \frac{\varepsilon_{\mathrm{x}}}{\gamma}$

Within this thesis three different emittance definitions are used which are calculated from different sets of particles. They describe different aspects of the particle distribution.

The projected emittance is calculated from the transverse phase space coordinates x and x' of all particles within the bunch (figure 4.1 a). With the usual diagnostic systems, e.g. screens, only the projected emittance can be measured. It gives an upper limit for the slice emittance which is important for the FEL process.

The slice emittance is calculated from the transverse phase space coordinates of particles with almost the same longitudinal position s. For different slices the slice emittance will usually vary (figure 4.1 b).

To calculate the correlated emittance the particle distribution is cut longitudinally into many short slices and for each slice s the mean transverse position $x_s = \langle x \rangle$ and the mean angle $x'_s = \langle x' \rangle$ are calculated. These new coordinates x_s and x'_s of all slices are used to calculate the correlated emittance. In other words, the correlated emittance is the emittance of the slice centers (figure 4.1 c). It is a measure for the orientation of the bunch in phase space. For a line distribution the projected and the correlated emittance are identical.

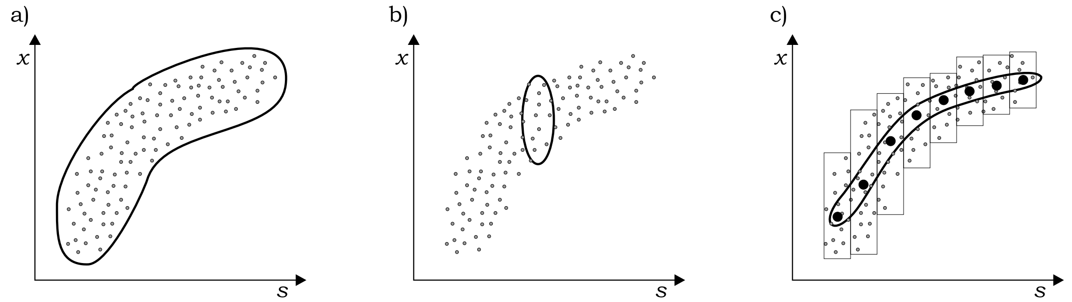

Figure 4.1: *Plots of the x-s phase space distribution are shown. For the calculation of the projected emittance all particles are used (a). To calculate the slice emittance only the particles in a short slice are considered (b). The correlated emittance is calculated from the transverse phase space coordinates of the slice centers (c).*

In the computer simulations the electron bunch is sometimes represented by a line-distribution of gaussian charge distributions, so called sub-bunches, and a short slice of particles (see chapter 5). From these two distribution only the correlated and the slice emittance can be calculated. To approximate the projected emittance, the slice is copied to the positions of the sub-bunches along the line-distribution and the charge of each slice is adjusted to match the charge of the sub-bunch at that position (figure 4.2). The projected emittance is calculated from the transverse phase space coordinates of all particles in this new distribution.

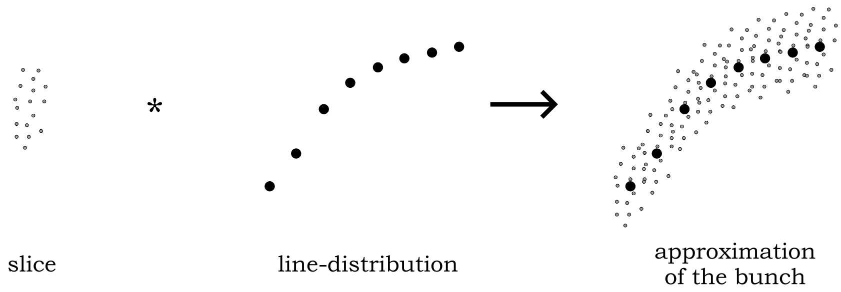

Figure 4.2: *In computer simulation the bunch is often represented only by a slice of particles and a line-distribution. The bunch shape can be approximated by a convolution of the two distributions.*

4.2 Synchrotron Radiation in a Bending Magnet

Electromagnetic radiation is always emitted by charged particles during acceleration. When electrons are accelerated parallel to their direction of motion, i.e. in accelerating cavities, the radiation power is negligible. But the acceleration perpendicular to the direction of motion in bending magnets can lead to a huge radiation power. In bunch compressor chicanes the radiation power is small as long as different electrons emit the synchrotron radiation incoherently. But for wavelengths longer than the bunch length, the electrons radiate coherently and the power increases by many orders of magnitude. For FELs the bunch length is so small that a huge part of the spectrum will be dominated by coherent radiation and strong radiation will be emitted in the bunch compressor chicanes. The electromagnetic fields exert longitudinal and transverse forces on the electrons inside the bunch and dilute the transverse emittance.

If an electron bunch is in circular motion, three regimes of synchrotron radiation can be distinguished [36]. As long as all electrons radiate individually, only incoherent synchrotron radiation (ISR) is emitted and the total radiation power $P_{\mathrm{i.c.}}$ scales linearly with the number of electrons N_{e}:

$$P_{\mathrm{i.c.}} = \frac{1}{6\pi\epsilon_0}\frac{N_{\mathrm{e}}e_0^2c\gamma^4}{R^2} \tag{4.1}$$

When inserting typical values for particle energy $E = \gamma m_0 c^2 = 500$ MeV, total charge $N_{\mathrm{e}}e_0 = 1$ nC and bending radius $R = 7.5$ m, the total incoherent power is $P_{\mathrm{i.c.}} \approx 5$ W. Consequently, the ISR is usually not of great importance in bunch compressors.

If the electrons radiate like a single particle of charge $N_{\mathrm{e}}e_0$ the entire spectrum is dominated by coherent synchrotron radiation (CSR). The power $P_{\mathrm{f.c.}}$ scales with the square of the number of electrons:

$$P_{\mathrm{f.c.}} = \frac{1}{6\pi\epsilon_0}\frac{(N_{\mathrm{e}}e_0)^2c\gamma^4}{R^2} \tag{4.2}$$

A bunch of 1 nC total charge consists of $N_{\mathrm{e}} \approx 6 \cdot 10^9$ electrons. Thus the total power is almost ten orders of magnitude higher than in the incoherent case.

In most practical cases the synchrotron radiation emitted in bunch compressor chicanes is not fully coherent. Only a fraction of the radiation spectrum is coherent whereas the remaining part is still incoherent. The radiation power is dominated by the coherent radiation and includes only a small incoherent part which can be neglected:

$$P_{\mathrm{p.c.}} = \frac{\Gamma\left(\frac{5}{6}\right)}{6^{1/3}4\pi^{3/2}\epsilon_0} \frac{(N_{\mathrm{e}}e_0)^2 c}{R^{2/3}\sigma_{\mathrm{s}}^{4/3}} + \frac{1}{6\pi\epsilon_0} \frac{N_{\mathrm{e}} e_0^2 c \gamma^4}{R^2} \approx \frac{\Gamma\left(\frac{5}{6}\right)}{6^{1/3}4\pi^{3/2}\epsilon_0} \frac{(N_{\mathrm{e}}e_0)^2 c}{R^{2/3}\sigma_{\mathrm{s}}^{4/3}} \tag{4.3}$$

The power of the coherent part depends on the bunch length σ_{s} but not on the particle energy, since only the high frequency part of the spectrum, i.e. the incoherent part, changes with energy (figure 4.3). The incoherent part of the spectrum will expand to higher frequencies when the energy increases and, consequently, the incoherent power increases. If the electron energy becomes high enough the incoherent radiation power starts to dominate. If the energy gets very low the radiation will be fully coherent.

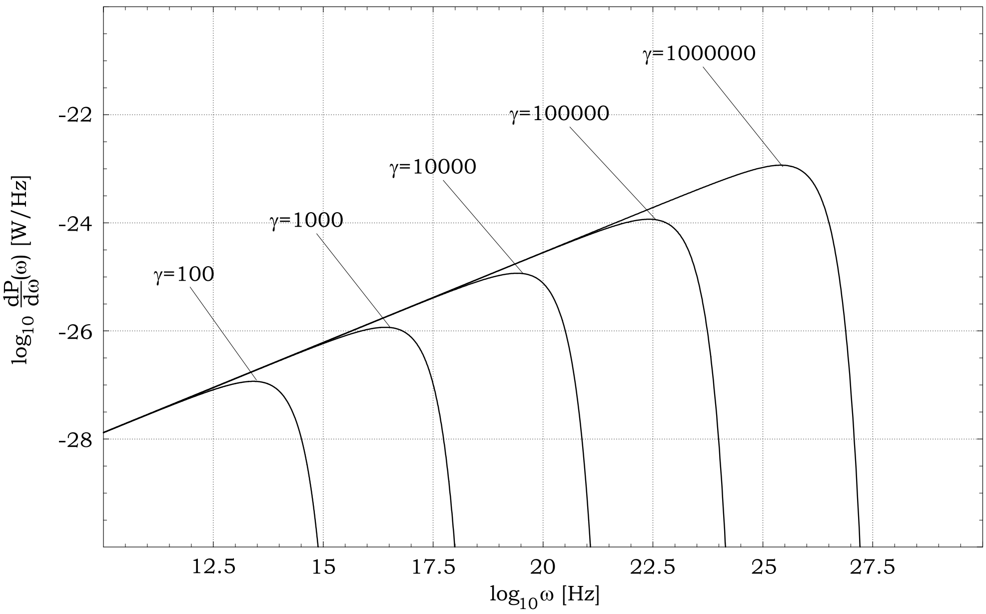

Figure 4.3: *The spectrum of a single electron in circular motion is show for different relativistic factors γ. The radius of curvature is $R = 5\,\mathrm{m}$.*

In general the radiation spectrum of an electron bunch in circular motion is given by [40]

$$\frac{dP}{d\omega}(\omega) = \frac{dP_1}{d\omega}\left(\frac{\omega}{\omega_{\mathrm{c}}}\right)\left(N_{\mathrm{e}} + N_{\mathrm{e}}(N_{\mathrm{e}}-1)e^{-\left(\frac{\sigma_{\mathrm{s}}\omega}{c}\right)^2}\right) \tag{4.4}$$

$$\frac{dP_1}{d\omega}(x) = \frac{\sqrt{3}e_0^2\gamma}{8\pi^2\epsilon_0 R} x \int_x^{+\infty} K_{5/3}(x')dx' \tag{4.5}$$

The critical frequency $\omega_{\mathrm{c}} = \frac{3c}{2R}\gamma^3$ divides the incoherent spectrum in two parts with the same integrated radiation power.

Figure 4.4 shows an example of a partially coherent spectrum. The low frequency part is dominated by coherent radiation whereas the high frequency part is incoherent. The transition from incoherent to coherent radiation depends on the bunch length. Hence, the total radiation power depends on the bunch length (figure 4.5).

The power increases when the bunch length decreases. A comparison of equations (4.1), (4.2) and (4.3) shows that the three radiation regimes are separated at $\sigma_{\mathrm{s}} = \sigma_{\mathrm{c}} \approx \frac{2}{3}\frac{R}{\gamma^3}$

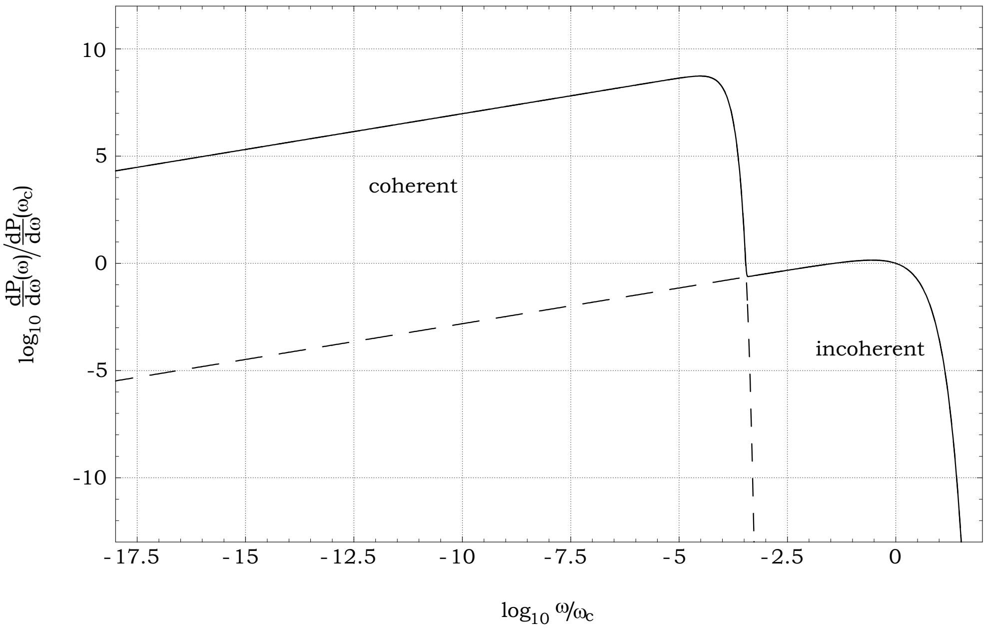

Figure 4.4: *The plot shows a partially coherent synchrotron radiation spectrum. The frequency is normalized to the critical frequency and the spectral power distribution is normalized to the spectral power which is radiated at the critical frequency. The frequency at which the bunch starts to radiate coherently depends on the bunch length. For this plot the parameters are:* $N_e e_0 = 1\,\mathrm{nC}$, $\sigma_s = 50\,\mu\mathrm{m}$, $\gamma = 500$, $R = 5\,\mathrm{m}$.

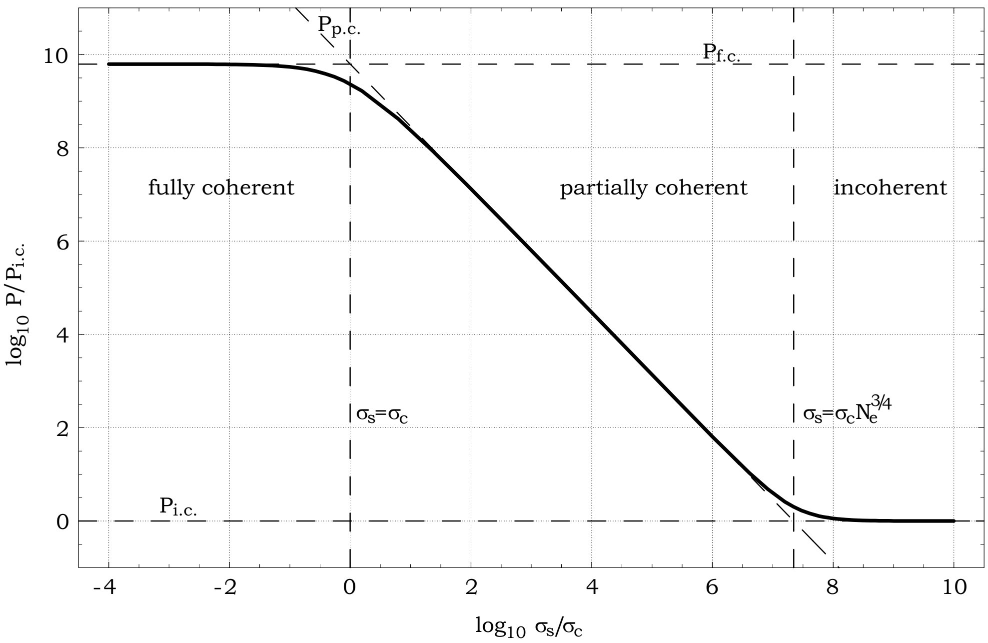

Figure 4.5: *The dependence of the total radiation power on the bunch length is shown. The bunch length is normalized to the critical bunch length* $\sigma_c \approx \frac{2}{3}\frac{R}{\gamma^3}$. *The power is normalized to the incoherent power* $P_{\mathrm{i.c.}}$. *Fully coherent radiation is emitted if* $\sigma_s \ll \sigma_c$. *The bunch radiates incoherently if* $\sigma_s \gg \sigma_c N_e^{3/4}$. *Here a total charge of* $N_e e_0 = 1\,\mathrm{nC}$ *is used and* $\sigma_c = 27\,\mathrm{nm}$.

and $\sigma_s = \sigma_c N_e^{3/4} \approx \frac{2}{3}\frac{R}{\gamma^3} N_e^{3/4}$. At the bunch compressor BC3 σ_s is at least three orders of magnitude larger than σ_c. Thus, the synchrotron radiation which is emitted by the electron bunches inside the dipoles is in the partially coherent regime.

Due to the dependence of the power on bunch length it is easy to understand why it might make sense to reduce the bending angles of the magnets towards the end of a bunch compressor chicane. Since the bunch gets shorter along the chicane the radiation power increases. With a reduction of the bending angles towards the end of the chicane the increase of the radiation power can be counteracted.

The conditions which separate the three regimes can also be derived from simple geometric considerations. When an electron bunch travels along an arc of a circle the radiation emitted by trailing electrons can catch up with electrons in front of them (figure 4.6). Inside an arc of radius R and angle α the electrons can interact if their distance is smaller than the slippage length

$$l_{sl} = z - z^* \approx \frac{R\alpha^3}{24} \tag{4.6}$$

Head and tail of a bunch of length σ_s can interact if the arc is longer than the overtaking length $l_{ov} \approx (24\sigma_s R^2)^{1/3}$.

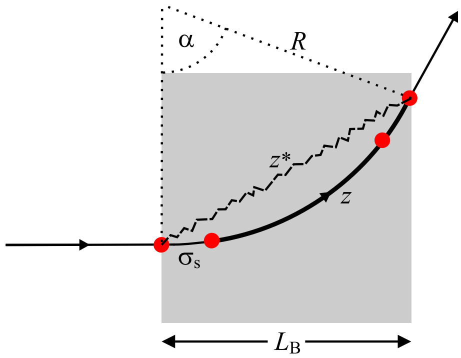

Figure 4.6: *Inside a bending magnet the radiation which is emitted from trailing electrons can catch up with electrons which are less than a slippage length $l_{sl} = z - z^*$ in front of them. Head and tail of a bunch can only interact if the magnet is long enough.*

These simple formulae are based only on geometric considerations and are valid for radiation with an opening angle larger than $\frac{\alpha}{2}$. Otherwise radiation and bunch would not overlap throughout the entire arc. The opening angle of the radiation depends on the frequency [41]. For very low frequencies $\omega \ll \omega_c$ the critical angle θ_c is

$$\theta_c \approx \frac{1}{\gamma}\left(\frac{2\omega_c}{\omega}\right)^{1/3} \tag{4.7}$$

The frequency for which $\theta_c = \frac{\alpha}{2}$ is $\omega_\alpha = \frac{16\omega_c}{\gamma^3\alpha^3} = \frac{c}{l_{sl}}$. If the slippage length l_{sl} is larger than the bunch length σ_s, the radiation with frequencies smaller than ω_α will overlap with the whole bunch throughout the full arc length. In other words, the wavelength of the radiation λ must be larger than $2\pi\sigma_s$ to produce coherent radiation of the bunch. Fully coherent radiation will be reached if the bunch is much shorter than the critical wavelength:

$$2\pi\sigma_s \ll \lambda_c = \frac{4\pi}{3}\frac{R}{\gamma^3} \tag{4.8}$$

This is the same condition which separates equation (4.2) from (4.3). The applicability of (4.3) can now be estimated roughly as

$$\frac{2}{3}\frac{R}{\gamma^3} \ll \sigma_\mathrm{s} \ll \frac{R\alpha^3}{24} \tag{4.9}$$

For a bunch in circular motion the upper limit of this condition can be too low, since, for bunch lengths a little larger than the slippage length, at least a fraction of the bunch can radiate coherently and the total power of the bunch will be already a few orders of magnitude higher than for incoherent radiation. Comparing equations (4.1) and (4.3) shows that the radiation starts to be partially coherent if $\sigma_\mathrm{s} \ll \frac{2}{3}\frac{R}{\gamma^3}N_\mathrm{e}^{3/4}$. This condition usually limits the partially coherent regime at a much higher frequency.

When a bunch of electrons passes a magnet of finite length transient effects have to be taken into account and the upper limit in equation (4.9) might be already too high. The radiation is not in steady state and the formulae for radiation of a bunch in circular motion are not valid. Since the particle energy is very high, relativistic effects have to be taken into account when the interaction of the electrons inside a bunch is determined. An electron at the bunch head is influenced by fields which are emitted at the retarded time $t_\mathrm{r} = t - \frac{1}{c}|\vec{r}(t_\mathrm{r})|$ by a trailing electron. $|\vec{r}(t_\mathrm{r})|$ is the distance of the two electrons at the retarded time. Along the path of the electrons three stages have to be distinguished for the field calculation [39]:

- a) The head of the bunch is inside the magnet but is influenced by fields which are emitted by the bunch tail at a position in front of the magnet (figure 4.7a).
- b1) Head and the position of the tail at the retarded time are both inside the magnet (figure 4.7b1).
- b2) Alternatively, it is also possible that the head is already behind the magnet but at the retarded time the tail was in front of the magnet (figure 4.7b2).
- c) The head is behind the magnet and the position of the tail at the retarded time is inside the magnet (figure 4.7c).

For values typical for BC3 ($\gamma m_0 c^2 = 500$ MeV, $\alpha = 4°$, $R = 7.5$ m, $\sigma_\mathrm{s} = 100\ \mu$m) the condition

$$\frac{1}{\gamma} \ll \left(\frac{24\sigma_\mathrm{s}}{R}\right)^{1/3} \leq \alpha \quad \Leftrightarrow \quad \frac{1}{24}\frac{R}{\gamma^3} \ll \sigma_\mathrm{s} \leq \frac{R\alpha^3}{24} \tag{4.10}$$

given in [39] is fulfilled. In this case the total energy loss due to the longitudinal CSR fields can be calculated by [39]

$$\Delta E_\mathrm{tot} \approx -\left(\frac{3^{1/3}N_\mathrm{e}^2 e_0^2}{4\pi\epsilon_0 R^{2/3}\sigma_\mathrm{s}^{4/3}}\right) R\alpha \left(1 + \frac{3^{1/3}4}{9}\frac{\sigma_\mathrm{s}^{1/3}}{R^{1/3}\alpha}\left(\ln\left(\frac{\sigma_\mathrm{s}\gamma^3}{R}\right) - 4\right)\right) \tag{4.11}$$

The condition given in (4.10) is almost the same condition which was derived earlier for the applicability of equation (4.3). But the total energy loss given by (4.11) is only the same as for the steady state case if, additionally, the condition

$$\frac{\sigma_\mathrm{s}^{1/3}}{R^{1/3}\alpha}\ln\left(\frac{\sigma_\mathrm{s}\gamma^3}{R}\right) \ll 1 \quad \Leftrightarrow \quad \sigma_\mathrm{s} \ll \frac{R\alpha^3}{\left(\ln\frac{\sigma_\mathrm{s}\gamma^3}{R}\right)^3} \tag{4.12}$$

is fulfilled [39]. Therefore the applicability of equation (4.3) is further limited. If this second condition is not fulfilled, i.e. the bunch is too long, the steady state regime cannot

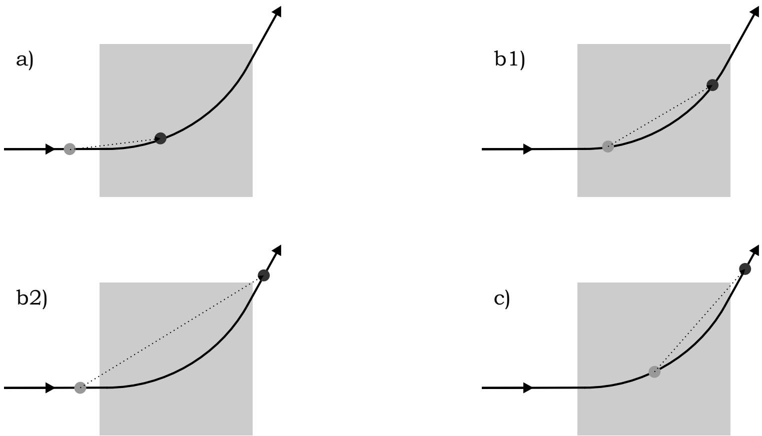

Figure 4.7: *When a bunch of electrons passes a bending magnet an electron at the bunch head (black dot) is influenced by radiation which is emitted by a trailing electron at the retarded time (grey dot). Four different cases have to be distinguished. The head is inside the magnet and is influenced by radiation emitted at a retarded position of the tail which is in front of the magnet (a). Head and retarded position of the tail are inside the magnet (b1). Alternatively, the head can be already behind the magnet but the retarded position of the tail is still in front of the magnet (b2). The head is behind the magnet and the retarded position of the tail is inside the magnet (c).*

be reached inside the magnet. The head of the bunch will be already behind the magnet but it will be strongly influenced by radiation which is emitted by trailing electrons with a retarded position inside or even in front of the magnet. Indeed, this is the case for the typical BC3 parameters given above.

Of course, not only the total radiation power differs from the steady state case when a bunch passes a magnet of finite length. Also the radiation spectrum can be significantly different from the spectrum emitted by a bunch in circular motion. It is found in [42] that only the high frequency part of the spectrum is close to the steady state spectrum whereas the low frequency part is constant for $\omega \to 0$.

Until now only the total energy loss of the whole bunch is outlined but what happens inside the bunch is neglected. If the synchrotron radiation would only cause a uniform energy loss of all electrons, one would have to correct the bending angles of the magnets in the chicane appropriately. The simple compression mechanism explained in chapter 3 would still work. Unfortunately, the energy is not just lost but also redistributed along the bunch. The case of a one-dimensional bunch with gaussian charge density in circular motion was described in [37]. In [39] analytical formulae are derived for the general case of a one-dimensional bunch with arbitrary charge density passing a circular arc. When a bunch of electrons enters a bending magnet a longitudinal force starts to build up due to the generation of the longitudinal CSR fields. The force changes the energy of the electrons and depends not only on the position of the bunch inside the magnet but also on the longitudinal position s of the electrons inside the bunch.

The energy change per distance travelled inside a bending magnet of finite length can be expressed for a bunch with a gaussian charge profile as [39]

$$\frac{dE(s,\rho)}{c\,dt} = -\frac{2N_\mathrm{e}e_0^2}{4\pi\epsilon_0\sqrt{2\pi}3^{1/3}R^{2/3}\sigma_\mathrm{s}^{4/3}}F_0(s/\sigma_\mathrm{s},\rho) \tag{4.13}$$

with the form factor

$$F_0(x,\rho) = \rho^{-1/3}\left(e^{-(x-\rho)^2/2} - e^{-(x-4\rho)^2/2}\right) + \int_{x-\rho}^{x} \frac{-x' e^{-x'^2/2}}{(x-x')^{1/3}} dx' \tag{4.14}$$

where $\rho = \frac{R\alpha^3}{24\sigma_s}$. $R\alpha$ is the length of the path the bunch has travelled inside the magnet. In figure 4.8 the development of the rate of the energy change along a bending magnet for a gaussian bunch of $\sigma_s = 100\,\mu$m is plotted. A clear energy loss from the tail is visible whereas the head gains energy. The radiation is dominated for a long time by the entrance transient. The steady state regime will not be reached within a magnet of $L_B = 0.5$ m, which is the length of the magnets used in BC3.

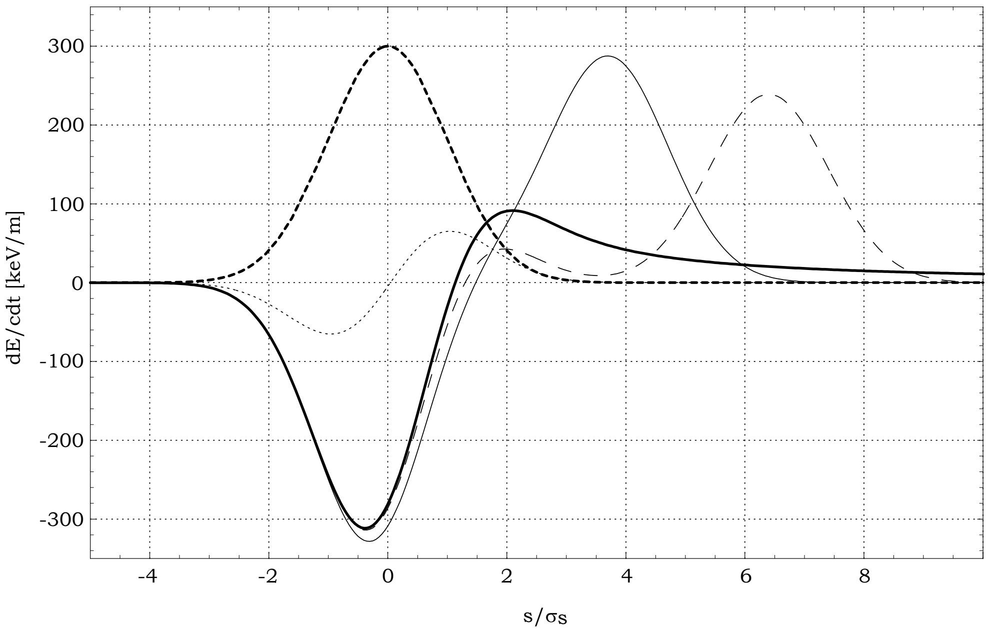

Figure 4.8: *The rate of the energy change along the bunch is plotted at various positions along a bending magnet. A gaussian bunch of* $N_e e_0 = 1$ nC *charge and a length of* $\sigma_s = 100\,\mu$m *(thick dash, a.u.) enters a dipole with a bending radius of* $R = 7.5$ m. *The head of the bunch is at* $\frac{s}{\sigma_s} > 0$. *Inside the dipole the electrons start to change their energy. The rate of the energy change is very weak if the bunch has travelled just* 15 cm *inside the dipole (thin dotted). Even after* 50 cm *(thin solid) the shape of the rate of energy change is considerably different from the steady state case (thick solid). After* 60 cm *(thin dash) the entrance transient has moved in front of the bunch and the final shape of the rate of energy change builds up.*

The nonuniform energy redistribution which is induced by the longitudinal fields is converted into nonuniform transverse electron offsets and angles in the dispersive parts of the bunch compressor chicane. Since the electron energy behind the chicane depends on the longitudinal electron position inside the bunch, only the correlated emittance of the bunch is affected. The slice emittance is influenced by nonlinear effects like the transverse dependence of the longitudinal field or the transverse fields.

When a bunch of electrons passes a bending magnet, transverse CSR fields are also emitted. This was first described for a coasting beam in circular motion in [43]. An analysis for a bunched beam with no transverse extent in circular motion is given in [44].

It is found that the transverse force is mainly proportional to the line charge density $\lambda(s)$ at the observation point and has a logarithmic dependence on the transverse radius σ_{r}:

$$F_{\perp}(s) \propto \frac{\lambda(s)}{R}\left(2\ln\frac{8R}{\sigma_{\mathrm{r}}} - C_0\right) + \frac{1}{R}\int_0^{\infty} \ln s^* \left(\frac{1}{3}\lambda'(s-s^*) - \lambda'(s+s^*)\right) ds^* \qquad (4.15)$$

The constant $C_0 \approx 3.91$ was found numerically, R is the bending radius. The transverse force is always centrifugal.

A detailed analysis of the electromagnetic fields for a bunched beam with no transverse extent moving along an arc of a circle was later given in [45] and [46]. In contrast to the longitudinal fields, which cause a pure tail-head interaction, for the calculation of the transverse fields head-tail effects also have to be taken into account. Another difference to the longitudinal fields is that the transverse fields decrease very fast behind the magnets. In agreement with [44] the force is always centrifugal and has a logarithmic dependence on the radius.

4.3 Particle Dynamics in a Magnetic Chicane under the influence of CSR fields

As we have seen in the previous section, the CSR fields alter the energy of the electrons when they pass a bunch compressor chicane. The trajectories of the electrons along the chicane will differ and consequently the transverse emittance grows. Due to the dependence of the fields on the longitudinal position of the electrons inside the bunch all electrons in a short slice will have similar trajectories and the slice emittance will stay almost constant. However, the final phase space coordinates of the slice centers will differ. Therefore the transverse correlated emittance, i.e. the volume populated by the slice centers, grows.

The full electron distribution can be expressed as the sum of many short slices at the positions of the slice centers. Consequently, the shape of the full distribution depends strongly on the orientation of the phase space distributions of the slices with respect to the phase space distribution of the slice centers. By changing the initial Twiss parameters the phase space distributions of the slices are rotated, whereas the phase space coordinates of the slice centers remain almost unchanged. Thus, the normalized projected emittance can be minimized by adjusting the initial Twiss parameters.

Also the amount of the slice emittance shows a dependence on the Twiss parameters. The longitudinal CSR fields depend on the transverse electron position. Additionally, the transverse CSR fields contribute to the transverse dynamics of the electrons. When the cross-section of the bunch becomes smaller these effects are weaker. Consequently, to reduce the overall effect of the CSR fields on the slice emittance, it is a good choice to minimize the beta function towards the end of a chicane, since there the CSR fields are strongest [47]. But one has to keep in mind that the minima of the slice emittance and the projected emittance are usually not obtained with the same initial Twiss parameters.

The impact of the energy redistribution due to the longitudinal CSR fields on the transverse phase space coordinates of the slice centers can be estimated by geometric considerations. Because of the nonuniform energy distribution, electrons at different longitudinal positions will be deflected differently in the bending magnets of the chicane. Additionally, the deflection in subsequent magnets will differ since the energy of the electrons changes along the chicane (figure 4.9).

To calculate the final transverse phase space coordinates of a particle at a slice center it is assumed that the initial transverse coordinates are $x_{\mathrm{i}} = 0$ and $x'_{\mathrm{i}} = 0$. Behind

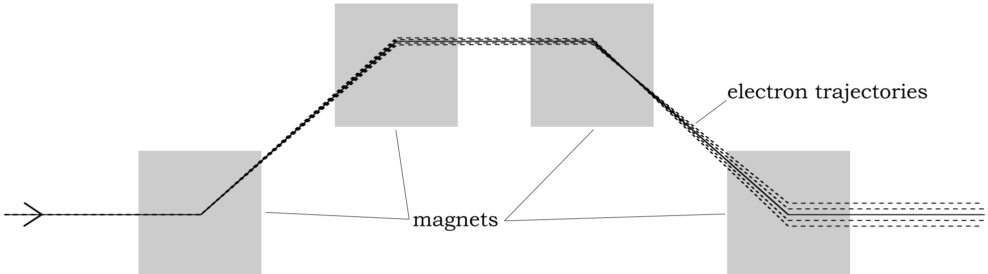

Figure 4.9: *Plotted are the trajectories of different electrons along a C-chicane. Each electron gets individual energy kicks inside the magnets and the trajectories diverge.*

the chicane the transverse position x_f and the angle x'_f of the particle will depend on its energy deviation which builds up along the chicane. Since in S-chicanes stronger magnets are needed than in C-chicanes the total energy deviations of the particles will be stronger. But the strength of the coupling of longitudinal and transverse phase space depends on the chicane geometry. Consequently, the emittance growth depends on the chicane geometry [48].

For a C-chicane the energy deviations of the particle in the four magnets are $\delta_{\mathrm{E},1}$, $(\delta_{\mathrm{E},1}+\delta_{\mathrm{E},2})$, $(\delta_{\mathrm{E},1}+\delta_{\mathrm{E},2}+\delta_{\mathrm{E},3})$ and $(\delta_{\mathrm{E},1}+\delta_{\mathrm{E},2}+\delta_{\mathrm{E},3}+\delta_{\mathrm{E},4})$. The deflection of the particle in a magnet is small and differs from the nominal angle α_0 approximately by the factor $\frac{1}{1+\delta_\mathrm{E}}$. Since the energy deviations are also very small it is a good approximation to set $\frac{1}{1+\delta_\mathrm{E}} \approx 1-\delta_\mathrm{E}$.

To describe the coupling of the particle's energy to its transverse offset and angle in a symmetric C-chicane, formula (3.11) has to be generalized to the case where the bending angles in all four magnets differ. To first order, behind the symmetric C-chicane the offset of a particle at the center of a slice will be

$$x_\mathrm{f}(\alpha_0,\delta_{\mathrm{E},2},\delta_{\mathrm{E},3},\delta_{\mathrm{E},4}) \approx \frac{\alpha_0}{2}\left(\delta_{\mathrm{E},2}(2L_{23}+4L_{12}+7L_\mathrm{B})+2\delta_{\mathrm{E},3}(L_{12}+L_\mathrm{B})-\delta_{\mathrm{E},4}L_\mathrm{B}\right) \quad (4.16)$$

If no energy slope $\frac{dE}{ds}$ was induced in the longitudinal phase space of the incoming bunch, the bunch will not be compressed when it passes the chicane. Then the energy of the particle changes in all magnets by almost the same amount, $\delta_{\mathrm{E},1}=\delta_{\mathrm{E},2}=\delta_{\mathrm{E},3}=\delta_{\mathrm{E},4}$, and we get:

$$x_\mathrm{f}(\alpha_0,\delta_\mathrm{E}) \approx \alpha_0\delta_\mathrm{E}\left(L_{23}+2L_{12}+2L_\mathrm{B}\right) \quad (4.17)$$

The final angle x'_f is the sum of the individual bending angles in the dipoles. They are approximately $\alpha_1=\alpha_0(1-\delta_{\mathrm{E},1})$, $\alpha_2=-\alpha_0(1-(\delta_{\mathrm{E},1}+\delta_{\mathrm{E},2}))$, $\alpha_3=-\alpha_0(1-(\delta_{\mathrm{E},1}+\delta_{\mathrm{E},2}+\delta_{\mathrm{E},3}))$ and $\alpha_4=\alpha_0(1-(\delta_{\mathrm{E},1}+\delta_{\mathrm{E},2}+\delta_{\mathrm{E},3}+\delta_{\mathrm{E},4}))$. To first order x'_f is

$$x'_\mathrm{f}(\alpha_0,\delta_{\mathrm{E},2},\delta_{\mathrm{E},4}) \approx \alpha_0(\delta_{\mathrm{E},2}-\delta_{\mathrm{E},4}) \quad (4.18)$$

Hence, the influence of the energy redistribution on the angle compensates partly and when there is no compression x'_f should vanish. The compensation takes place for every slice along the bunch. If a bunch passes a C-chicane but remains uncompressed, the trajectories of all slices should be parallel to the Z-axis behind the chicane.

For a symmetric 6-bend S-chicane the same considerations lead to a final transverse offset of

$$\begin{aligned} x_\mathrm{f}(\alpha_0,\delta_{\mathrm{E},2},\ldots,\delta_{\mathrm{E},6}) \approx \frac{\alpha_0}{2}&\left(\delta_{\mathrm{E},2}(4L_{23}+8L_{12}+13L_\mathrm{B})+2\delta_{\mathrm{E},3}(L_{12}+L_\mathrm{B})\right. \quad (4.19)\\ &\left.-\delta_{\mathrm{E},4}(2L_{23}+4L_{12}+7L_\mathrm{B})-\delta_{\mathrm{E},5}(2L_{12}+2L_\mathrm{B})+\delta_{\mathrm{E},6}L_\mathrm{B}\right)\end{aligned}$$

and in the case of an uncompressed bunch to

$$x_{\mathrm{f}}(\alpha_0, \delta_{\mathrm{E}}) \approx \alpha_0 \delta_{\mathrm{E}} \left(L_{23} + 2L_{12} + \frac{7}{3} L_{\mathrm{B}} \right) \tag{4.20}$$

Comparing C-chicanes and S-chicanes with the same R_{56} shows that the final transverse offsets of the slices are smaller behind an S-chicane[1]. On the other hand, the angle behind the S-chicane is

$$x'_{\mathrm{f}}(\alpha_0, \delta_{\mathrm{E},2}, \delta_{\mathrm{E},4}, \delta_{\mathrm{E},6}) \approx \alpha_0 (\delta_{\mathrm{E},2} - \delta_{\mathrm{E},4} + \delta_{\mathrm{E},6}) \tag{4.21}$$

When comparing this to equation (4.18) which was derived for the C-chicane one has to keep in mind that the energy changes in the last dipole of the C-chicane by $\delta_{\mathrm{E},4}$ and in the last dipole of the S-chicane by $\delta_{\mathrm{E},6}$. These should have a very similar value. The $\delta_{\mathrm{E},2}$ is a little smaller in the S-chicane since the bunch is still a little longer at the position of the second dipole. Thus, the absolute value of the final angle should be comparable to the one behind a C-chicane but it changes sign. In case of no compression a small residual angle remains behind the S-chicane.

A compensation scheme that is similar to an S-chicane can also be achieved with two C-chicanes. They have to be separated by quadrupoles which flip over the transverse phase space but do not change the absolute values of the coordinates. Such a transformation is also called $-I$-transformation [48].

As we have seen before in chapter 3.3 it is possible to shift the central magnets of an S-chicane without changing the bending angles. In this case neither dispersion nor momentum compaction factors are changed. But if we take the energy redistribution due to the longitudinal CSR fields into account, it can be shown that the final offset x_{f} of a slice center depends on the amount of the longitudinal shift Δl of the central magnets. To first order the final transverse offsets of the slice centers and thus the correlated emittance can be cancelled if the shift is

$$\begin{aligned} \Delta l = \frac{1}{2\delta_{\mathrm{E},2} + 4\delta_{\mathrm{E},4} + 2\delta_{\mathrm{E},5}} & (-\delta_{\mathrm{E},2}(8L_{12} + 4L_{23} + 13L_{\mathrm{B}}) - \delta_{\mathrm{E},3}(2L_{12} + 2L_{\mathrm{B}}) \\ & + \delta_{\mathrm{E},4}(4L_{12} + 2L_{23} + 7L_{\mathrm{B}}) + \delta_{\mathrm{E},5}(2L_{12} + 2L_{\mathrm{B}}) - \delta_{\mathrm{E},6} L_{\mathrm{B}}) \end{aligned} \tag{4.22}$$

A positive Δl is a shift towards the end of the chicane. Using nominal operation parameters of BC3, i.e. a compression of the bunch length by a factor of 5, and assuming that the energy changes inside the dipoles proportional to $\sigma_{\mathrm{s}}^{-4/3}$ (see eqn. (4.3)), a shift of $\Delta l = 35$ cm is needed to cancel the transverse offsets. Indeed, this value is close to the value $\Delta l = 60$ cm, which is used in the simulations in chapter 6. It is the result of a comparison made in [83].

Also the effect of the transverse CSR fields can be estimated by geometric considerations. Under the assumption of no bunch compression the absolute values of the transverse fields will be almost the same in all magnets of the chicane. Due to the logarithmic dependence of the transverse fields on the bunch radius, the change of the beta function along the chicane has a negligible effect. Only the signs of the transverse fields change with the signs of the bending angles. Accordingly, to first order, the influence of the transverse fields on the transverse phase space coordinates should be compensated behind the chicane and the correlated emittance should remain unchanged. Nonlinearities will have a small impact on the slice emittance. In case of compression the transverse fields increase along the chicane and a residual effect even on the correlated emittance can be expected. The

[1] In practice, the value of L_{12} is smaller for the S-chicane than for the C-chicane whereas L_{23} and L_{B} are the same, at least for the chicanes which are compared within this thesis.

impact of the transverse fields is usually smaller than the impact of the longitudinal fields but it is not negligible.

These simple considerations are confirmed by computer simulations which include the CSR fields. A line-distribution of 1 nC total charge and an energy of 450 MeV is tracked with the code TraFiC^{4}2.0 through a symmetric C-chicane and a symmetric 6-bend S-chicane. Initially, the distribution has a gaussian charge profile and an rms length of 250 μm. The line-distribution is represented by gaussian charge distributions, so called sub-bunches. The transverse phase space was not populated. The chicane layouts match the symmetric C-chicane and the symmetric 6-bend S-chicane which are used in chapter 6. They have a momentum compaction factor of $R_{56} = -5$ cm. For general information on the computer simulations refer to chapter 5.

To indicate the influence of the longitudinal and the transverse CSR fields three different cases are compared:

a) longitudinal and transverse CSR fields are included in the simulations
b only longitudinal CSR fields are included in the simulations
c) only transverse CSR fields are included in the simulations

A mono-energetic electron bunch will not be compressed when it passes the chicanes. In this case the influence of the transverse CSR fields on the final phase space coordinates of the sub-bunches is small in both chicanes (figures 4.10 and 4.11). Nevertheless, the transverse sub-bunch offsets are larger behind the C-chicane than behind the S-chicane. On the other hand, the trajectories of the sub-bunches are almost parallel to the Z-axis behind the C-chicane whereas they diverge slightly behind the S-chicane. In the S-chicane the sub-bunches accumulate a stronger energy deviation than in the C-chicane.

If a linear energy slope $\frac{1}{E_0}\frac{dE}{ds} = -16\ \mathrm{m}^{-1}$ is induced along the bunch it will be compressed in to a final rms length of 50 μm. The transverse CSR fields than have a noticeable influence on the final phase space distribution in both chicanes (figures 4.12 and 4.13). The angles x' of the sub-bunches have comparable absolute values behind the two chicanes but the signs are different. The transverse offsets x_f are smaller behind the S-chicane.

The development of the longitudinal and transverse phase space coordinates as well as the longitudinal and transverse CSR fields along the C-chicane is plotted in figure 4.14. For the S-chicane the development is plotted in figure 4.15. The bunch is not compressed. The chicane and bunch parameters are the same as above but the simulations utilized the code CSRTrack (see chapter 5). The pictures are taken just in front of the magnets and at the end of each magnet. The last picture is taken 2 m downstream of the last magnet. The data shown in figures 4.10 and 4.11 corresponds to the second to last row in figures 4.14 and 4.15 respectively. Small differences of the phase space coordinates are due to slightly different positions along the chicanes and due to the different simulation codes. Note the different scale.

The longitudinal CSR fields are very similar in all dipoles of the chicanes (figures 4.14 and 4.15). The transverse CSR fields change sign with the signs of the bending angles. It is interesting to note that the longitudinal CSR fields drop off very slowly along the drift spaces which follow the dipoles. Even in front of the next dipole the longitudinal CSR fields are not negligible. In contrast to this the transverse CSR fields decay very fast in the drifts.

In figure 4.16 the final transverse phase space distributions which are obtained by the computer simulations are compared to the distributions calculated by equations (4.16) and (4.18) for the C-chicane and by equations (4.20) and (4.21) for the S-chicane. The energy deviations which are needed for the analytical calculations are taken from the simulation data. The results agree very well.

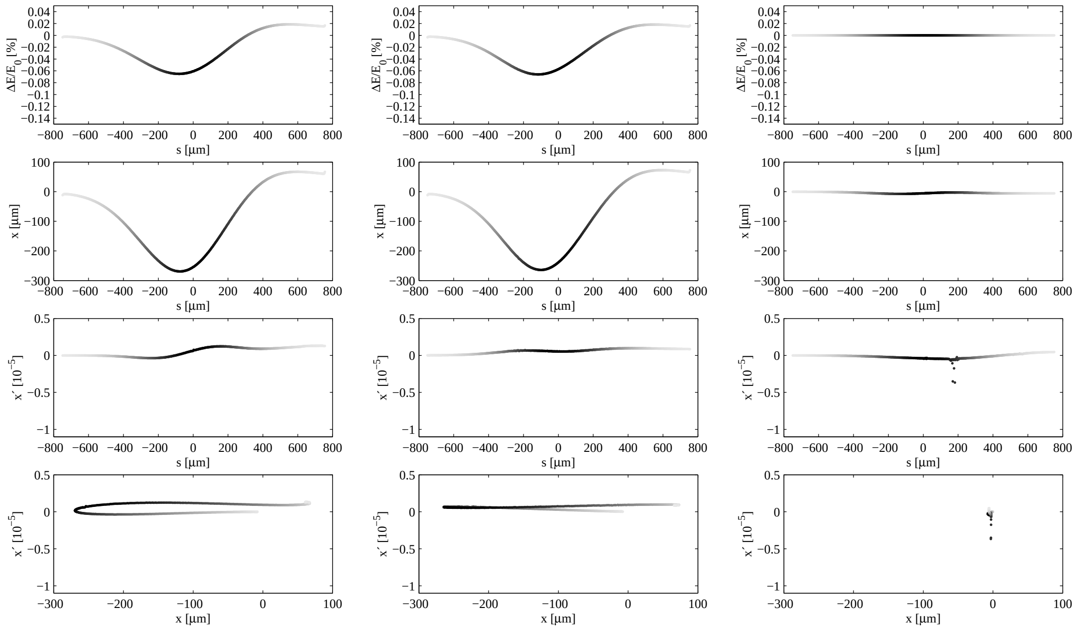

Figure 4.10: *Each column shows the longitudinal and transverse phase space coordinates of a mono-energetic bunch that passed a C-chicane but remained uncompressed. To obtain the results the computer simulations used longitudinal and transverse CSR fields (left column), only longitudinal CSR fields (middle column), only transverse CSR fields (right column). Initially, the bunch had a gaussian charge profile and vanishing transverse phase space coordinates. Dark dots represent particles with a higher charge than lighter dots. In some plots numerical noise is visible.*

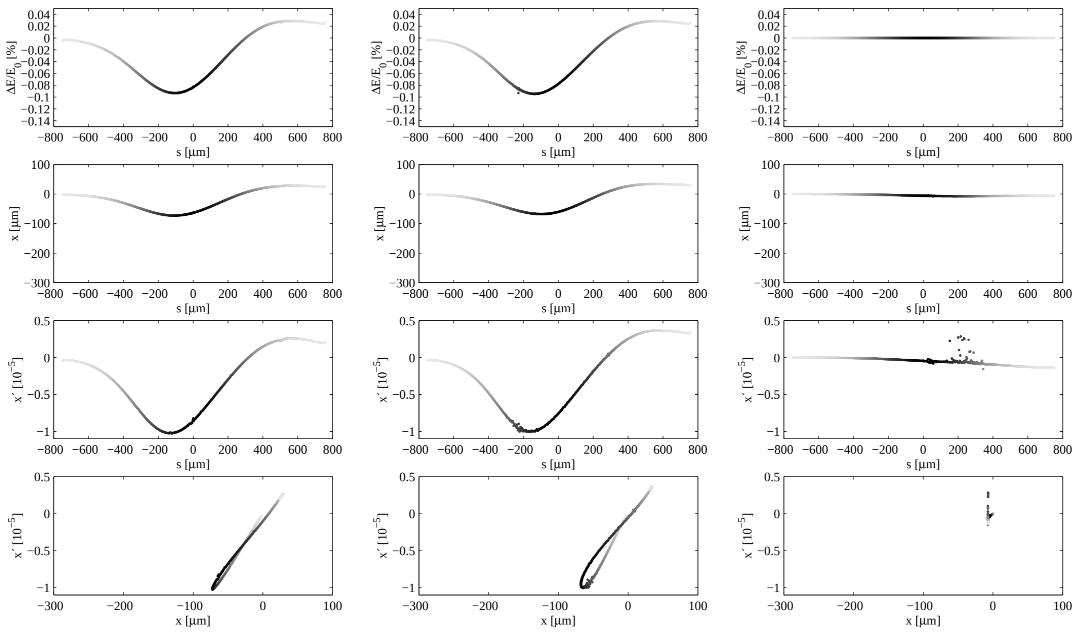

Figure 4.11: *Each column shows the longitudinal and transverse phase space coordinates of a mono-energetic bunch that passed an S-chicane but remained uncompressed. To obtain the results the computer simulations used longitudinal and transverse CSR fields (left column), only longitudinal CSR fields (middle column), only transverse CSR fields (right column). Initially, the bunch had a gaussian charge profile and vanishing transverse phase space coordinates. Dark dots represent particles with a higher charge than lighter dots. In some plots numerical noise is visible.*

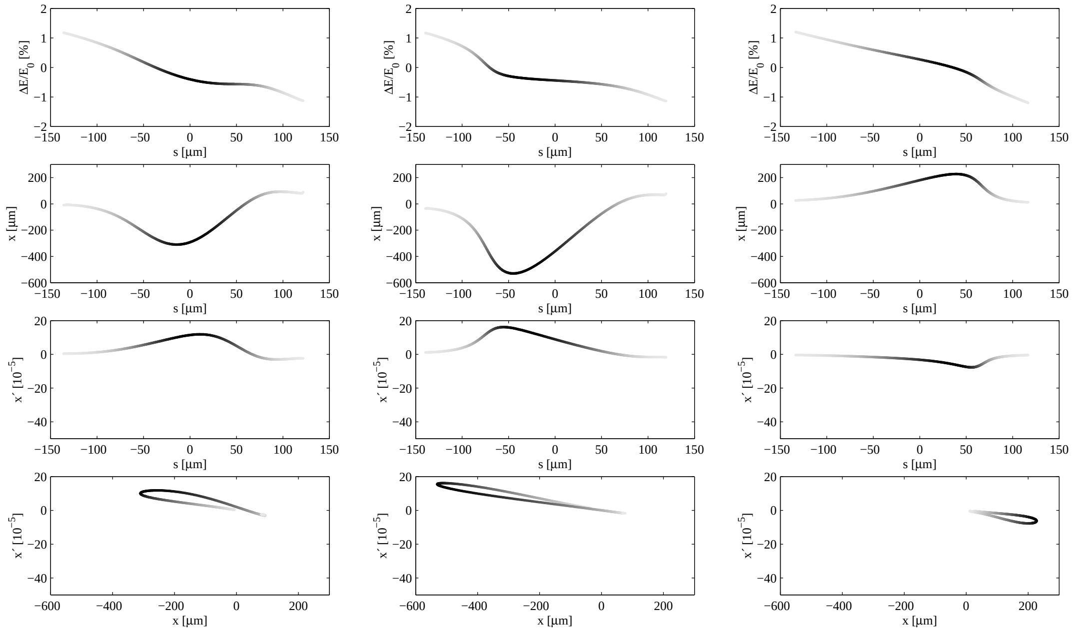

Figure 4.12: *Each column shows the longitudinal and transverse phase space coordinates of a bunch that was compressed in a C-chicane. The compression is achieved by inducing a linear energy slope. To obtain the results the computer simulations used longitudinal and transverse CSR fields (left column), only longitudinal CSR fields (middle column), only transverse CSR fields (right column). Initially, the bunch had a gaussian charge profile and vanishing transverse phase space coordinates. Dark dots represent particles with a higher charge than lighter dots.*

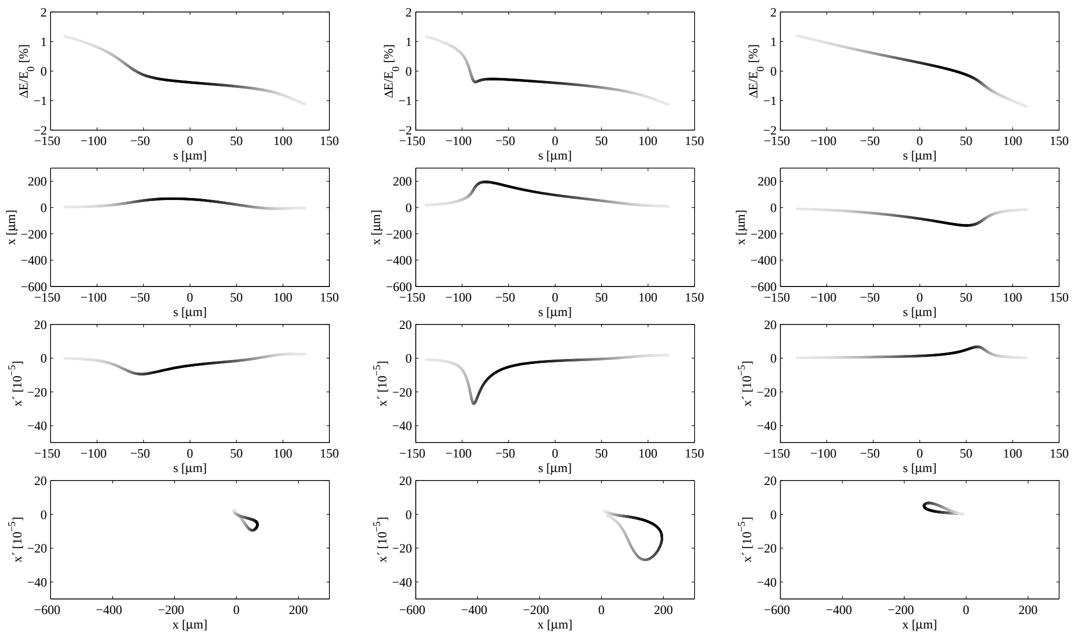

Figure 4.13: *Each column shows the longitudinal and transverse phase space coordinates of a bunch that was compressed in an S-chicane. The compression is achieved by inducing a linear energy slope. To obtain the results the computer simulations used longitudinal and transverse CSR fields (left column), only longitudinal CSR fields (middle column), only transverse CSR fields (right column). Initially, the bunch had a gaussian charge profile and vanishing transverse phase space coordinates. Dark dots represent particles with a higher charge than lighter dots.*

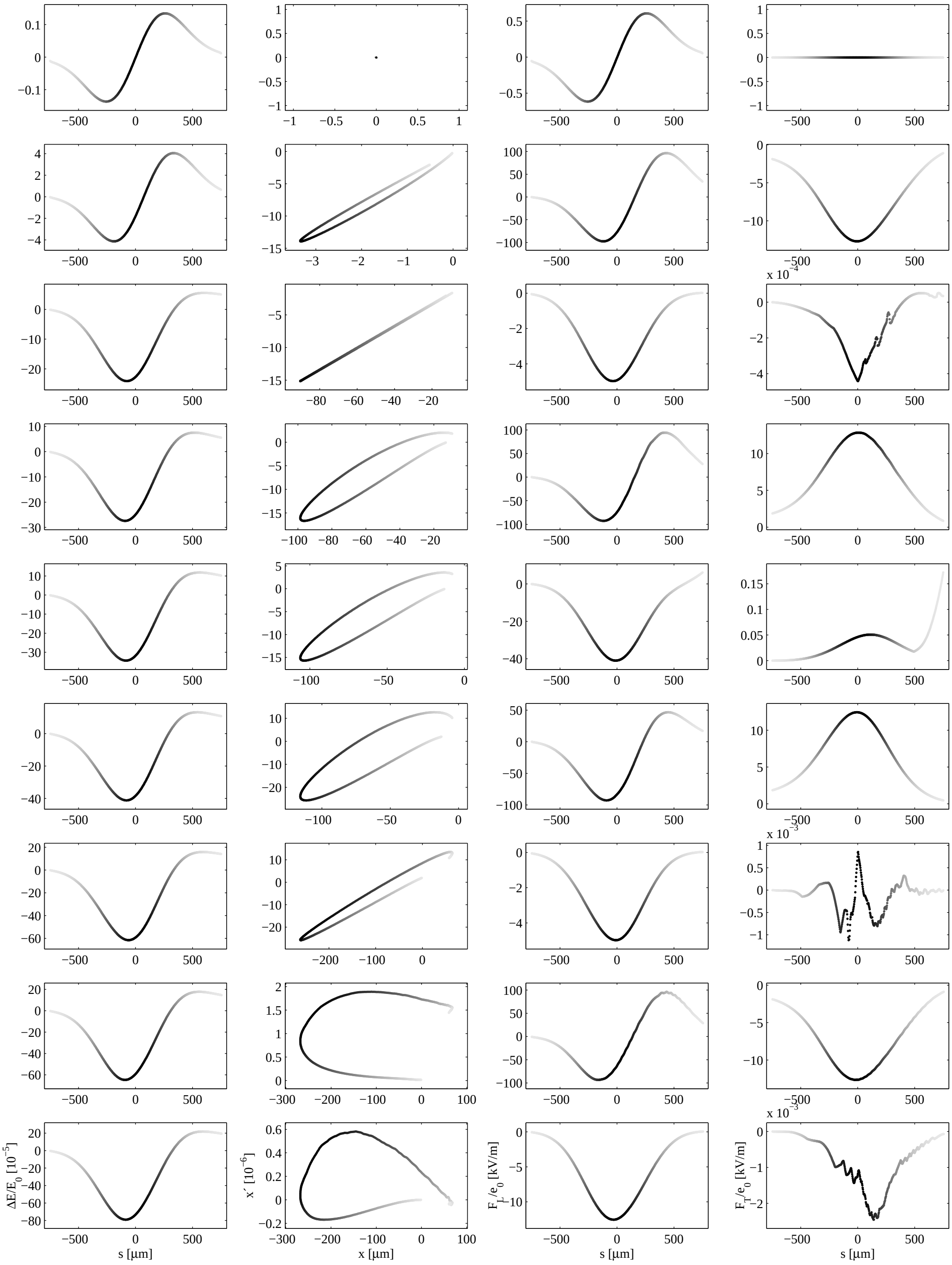

Figure 4.14: *The development of the longitudinal phase space distribution (left column), the transverse phase space distribution (second column), the longitudinal CSR fields (third column) and the transverse CSR fields (right column) along a C-chicane is shown for a bunch that is not compressed. For each of the four magnets the data is plotted right in front of the magnet and at the end of the magnet (rows from top to bottom). The last row contains the data* 2 m *behind the last magnet. The labels of the axes are given only in the last row but are valid for all rows. The noise in the transverse fields is due to the limited simulation accuracy.*

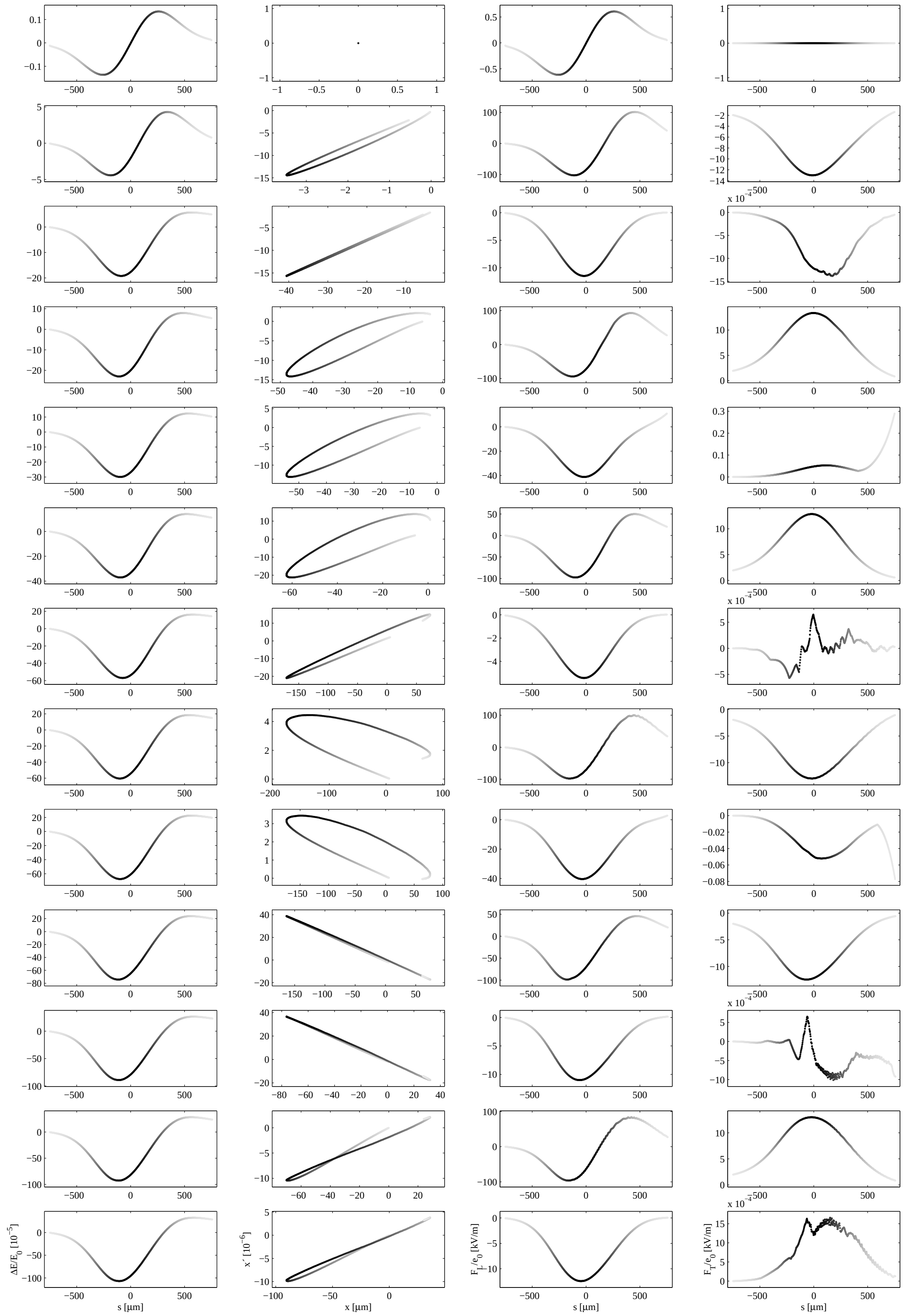

Figure 4.15: *The development of the longitudinal phase space distribution (left column), the transverse phase space distribution (second column), the longitudinal CSR fields (third column) and the transverse CSR fields (right column) along an S-chicane is shown for a bunch that is not compressed. For each of the six magnets the data is plotted right in front of the magnet and at the end of the magnet (rows from top to bottom). The last row contains the data 2 m behind the last magnet. The labels of the axes are given only in the last row but are valid for all rows. The noise in the transverse fields is due to the limited simulation accuracy.*

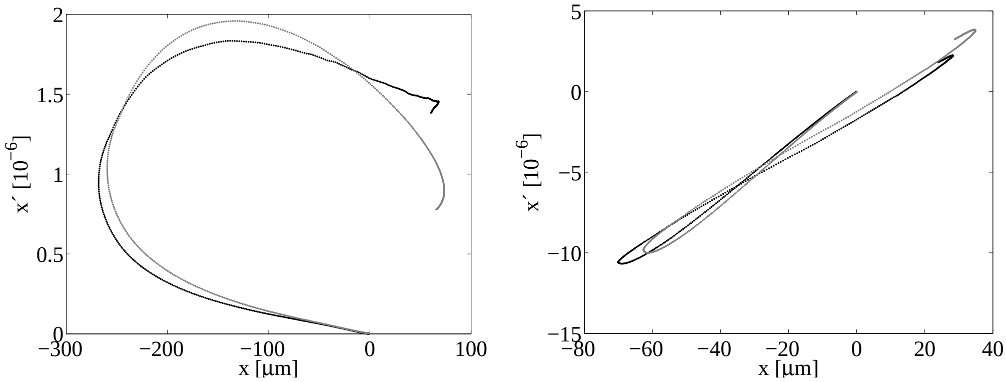

Figure 4.16: *The transverse phase space distributions behind a C-chicane (left) and behind an S-chicane (right) are shown. The data taken from computer simulations (black) is compared to the distributions which are calculated by equations (4.16) and (4.18) for the C-chicane and by equations (4.20) and (4.21) for the S-chicane (grey).*

4.4 Shielding due to the Conductive Walls of the Vacuum Chamber

The electromagnetic fields generated by a bunch of electrons interact with the conducting walls of the vacuum chamber. Inside a narrow vacuum chamber the low frequency part of the fields parallel to the chamber walls is suppressed and the radiation power decreases. Literally speaking, the shielding occurs because wavelengths larger than the size of the vacuum chamber cannot propagate inside the chamber. Since the low frequency part of the spectrum is emitted coherently by the electrons the total power can be strongly reduced by the shielding effect.

The simple model of a bunch circulating between two infinitely large parallel plates with infinite conductivity was discussed in [36] and later the results were generalized for the case of finite parallel plates in [40]. By using image charges a derivation is performed in [38]. Two asymptotic cases can be distinguished. One is the weak shielding regime, which is described in [49], and the other is the strong shielding regime, which is described in [50].

In case of circular motion the spectrum of a bunch moving between two infinitely large, parallel plates with infinite conductivity which are separated by the distance h is [36]

$$\frac{dP_{\rm shield}}{d\omega}(\omega) = \frac{dP^*_{\rm shield}}{d\omega}\left(\frac{\omega R}{c}\right)\left(N_{\rm e} + N_{\rm e}(N_{\rm e}-1)e^{-\left(\frac{\sigma_{\rm s}\omega}{c}\right)^2}\right) \tag{4.23}$$

$$\frac{dP^*_{\rm shield}}{d\omega}(n) = \frac{1}{3\pi^2\epsilon_0}\frac{N_{\rm e}^2 e_0^2}{h}\sum_{p=1,3,5,\ldots}^{nh/\pi R}\frac{g_p^4}{n^3}\left(K^2_{1/3}\left(\frac{g_p^3}{3n^2}\right) + K^2_{2/3}\left(\frac{g_p^3}{3n^2}\right)\right)$$

with $g_p = \frac{p\pi R}{h}$. This formula is valid for $\omega \ll \omega_{\rm c} = \frac{3c}{2R}\gamma^3$. It can also be used for non-circular motion as long as the bending radius R is much larger than the radiation formation length $L_{\rm rad} = 2\sqrt{\pi h R}$ [51]. An analysis for a bunch entering a bending magnet from a straight pass is given in [52].

The shielding becomes important for bunches with a length $\sigma_{\rm s} \gg \frac{h}{\pi}\sqrt{\frac{3h}{2\pi R}}$ otherwise the radiation spectrum is shifted to too high frequencies [51]. Assuming a bunch length of $\sigma_{\rm s} = 100\ \mu$m and a bending radius of $R = 5$ m the height of the vacuum chamber should be less than 1 cm for an efficient shielding. In figure 4.17 one can see that all frequencies below the threshold frequency $\omega_{\mathrm{th}} = \sqrt{\frac{2}{3}\frac{c}{R}}\left(\frac{\pi R}{h}\right)^{3/2}$ are suppressed.

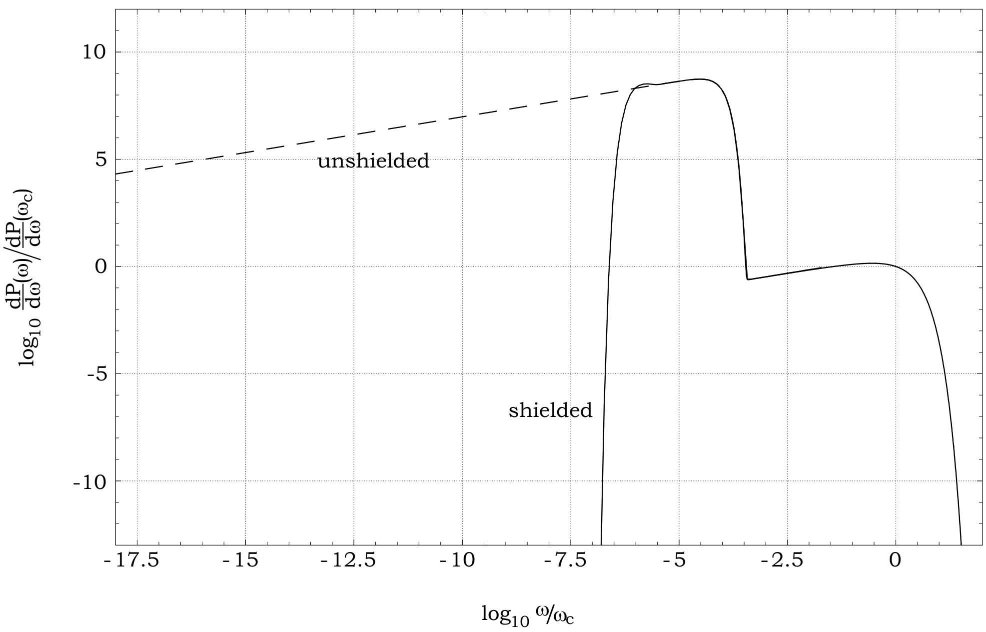

Figure 4.17: *The normalized spectrum of a bunch circulating in free space (dashed) is compared to the normalized spectrum of a bunch circulating between two infinitely large plates which are separated by the distance* $h = 0.1$ m *(solid). Low frequencies are suppressed due to the shielding effect of the plates. If the separation of the plates gets smaller the threshold moves to higher frequencies.*

To study the dependence of the total radiation power on the chamber height approximate functions can be used. The case of strong shielding is given if $n_{\mathrm{th}} > n_{\mathrm{c}}$. Here $n_{\mathrm{th}} = \sqrt{\frac{2}{3}}\left(\frac{\pi R}{h}\right)^{3/2}$ is the threshold harmonic and $n_{\mathrm{c}} = \frac{R}{\sigma_{\mathrm{s}}}$ is the characteristic harmonic. Using BC3 parameters ($R = 7.5$ m, $h = 15$ mm (maximum possible height), $\sigma_{\mathrm{s}} = 250\,\mu$m) we get $n_{\mathrm{th}} \approx 51000$ and $n_{\mathrm{c}} \approx 30000$. Thus the strong shielding formula for the total power is valid. It also gives a good approximation if n_{th} is not too much lower than n_{c}, but the radiation power is underestimated [50]:

$$P_{\mathrm{shield}}(h) = \frac{1}{4\pi\epsilon_0}\frac{4N_{\mathrm{e}}^2 e_0^2 c}{3\pi R h}\sum_{p=1,3,\ldots}^{\infty} I_0(p) \tag{4.24}$$

$$I_0(p) = 3\pi\frac{p\pi R}{h}K_0\left(2\frac{p^{3/2}\sqrt{2/3}(\pi R/h)^{3/2}}{R/\sigma_{\mathrm{s}}}\right) \tag{4.25}$$

The dependence of the radiated power on the chamber height h for a $50\,\mu$m bunch and a $250\,\mu$m bunch of 1 nC charge is plotted in figures 4.18a and 4.18b. Both plots show the power calculated by the strong shielding formula (4.24) and the power obtained by a numerical integration of the spectra. It is obvious that in case of $n_{\mathrm{th}} < n_{\mathrm{c}}$ the power is underestimated by (4.24). For a $50\,\mu$m bunch the chamber has to be very flat to influence the radiation power. The spectrum of a $250\,\mu$m bunch is dominated by lower frequencies and shielding starts to be efficient in chambers which are higher.

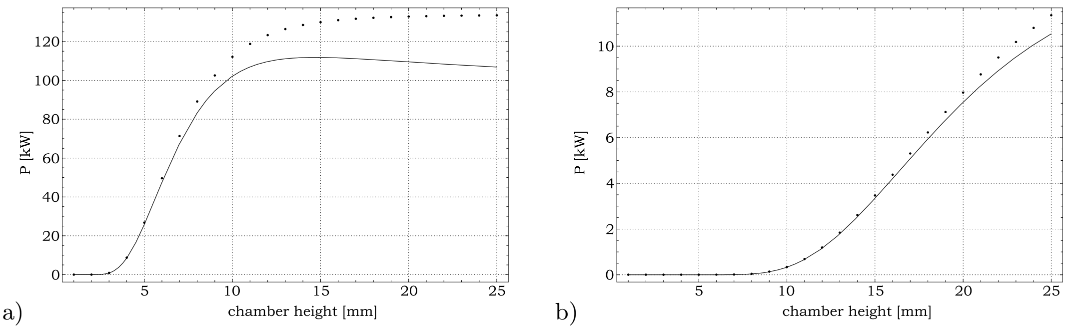

Figure 4.18: *The dependence of the total CSR radiation power on the chamber height is plotted for a bunch of* 50 μm *rms lengths (a) and a bunch of* 250 μm *rms lengths (b). The strong shielding formula (solid) is good for chambers with a small height. But if the chamber height increases the radiation power obtained by numerical integration of the spectra (dots) is underestimated.*

4.5 Wake Fields

In the preceding section the conductivity of the vacuum chamber was assumed to be infinite. Additionally, the surface of the chamber was assumed to be perfectly smooth. In reality of course this is not given and additional effects can become important. These are the resistive wall wake fields, which depend on the resistivity of the chamber walls, the surface roughness wake fields, which depend on the structure of the surface of the chamber, and the wake fields which are emitted due to steps and tapers in the cross section of the chamber.

In contrast to CSR, which is mainly a tail-head interaction, the wake fields are a head-tail interaction. Also the wake fields lead to an energy redistribution along the bunch and to an emittance growth. In some cases the modification of the phase space distribution due to the longitudinal wake fields can be utilized. This is for example done at the Sub-Picosecond Photon Source (SPPS) at the Stanford Linear Accelerator Center (SLAC) [53].

A finite conductivity of the chamber walls decreases the phase velocity of the fields travelling with the electron bunch. Thus, they fall behind and trailing particles will consequently travel through fields emitted by particles ahead of them [54, 55, 56]. If the surface resistivity is high, e.g. in stainless steel chambers, the longitudinal and transverse forces exerted by the fields can have a considerable effect on the dynamics of the beam [57]. Narrow chambers are therefore build of aluminium or copper. For mechanical reasons sometimes stainless steel chambers with a copper coated surface are used, e.g. in BC3. The influence of the resistive wall wake fields on the beam dynamics in BC3 is expected to be a lot smaller than the influence of the CSR fields.

The impact of surface roughness wake fields on the beam is studied in several theoretical approaches for different structures of the surface (for a summary see [58] and [59]). The agreement of the experiments which were performed at DESY with some of the theories is good [60]. For the undulator chambers of the VUV-FEL it is expected that the effect of the surface roughness wake fields is small in comparison to the resistive wall wake fields. These aluminium chambers have an inner diameter of 9.5 mm and a measured rms surface roughness of 0.6 μm. The copper coated BC3 chambers have an inner height of 8 mm and the surface roughness is specified to be better than 0.8 μm. Measurements of the surface profile, which were done by the manufacturer [61], result in an rms roughness of just 0.32 μm (figure 4.19). One can conclude that the effect of surface roughness wake fields should be small for these chambers.

Steps in the cross section of a vacuum chamber can strongly influence the fields travelling with the bunch. To reduce their impact smooth tapers are usually used in beam lines [55, 62, 63, 64, 65]. Tapers can be found at the beginning and the end of the BC3 vacuum chambers, since their height is smaller than the diameter of the attached beam pipes. Steps are not used in the chicane, but at the bellows which connect the individual parts of the chamber there are short gaps. Also the slits for the vacuum pumps might have a small impact on beam dynamics.

The influence of the wake fields on beam dynamics strongly depends on the mechanical and electrical properties of the chamber as well as the properties of the electron beam. A thorough analysis for the vacuum chambers which are used at BC3 was not done. The decision to use a copper coated surface with a roughness better than 0.8μm is based only on quick estimates of the effects and reflects mainly a common agreement that stainless steel chambers with a small height should be avoided. The good surface quality is achieved with a standard production process (milling and galvanic copper coating). During the production of the chambers it was not possible to coat the full inner surface with copper. The outermost millimeters of the surface had to be left out. This might influence the beam if the dipoles of BC3 are operated with very high or very low bending angles.

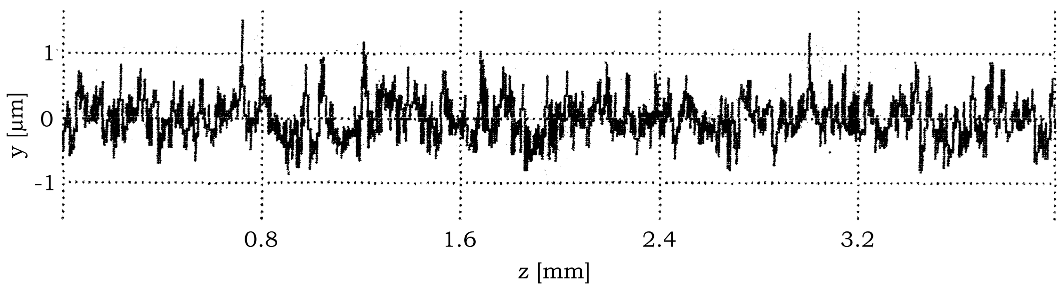

Figure 4.19: *The measured surface profile of the copper coated chamber for BC3 is plotted. Almost all points lie within* $\pm 1\mu$m *and the rms value of the surface roughness is* $0.32\ \mu$m.

Chapter 5

CSR Simulation codes

In the usual optics and tracking codes for accelerator development the bunch self interaction due to synchrotron radiation and also due to space charge fields is neglected. Therefore special CSR tracking codes (e.g. TraFiC^4 [66], CSRTrack [67] and a code by R. Li [78]) have been developed or existing codes have been expanded (e.g. Elegant [68], TREDI [69, 70]). An overview of the existing codes and their current status can be found in [71], [72] and [73].

The main difference between these codes is the description of the electromagnetic fields and the electron distributions. The simplest and therefore fastest way to calculate the CSR fields is the one-dimensional (1D) method which is also called projected method. It is based on analytical formulae derived for the longitudinal CSR fields of a 1D charge distribution moving in an arc of a circle [39]. Further derivations are given in [74] and [75]. The code Elegant uses this CSR model [76] and it is also implemented in the code CSRTrack.

For point-like particles the full three-dimensional (3D) integration of the retarded Lienard-Wiechert potentials would be the correct calculation of the electromagnetic fields. Unfortunately, many particles are needed to reduce noise. Additionally, the fields diverge at the positions of the particles. A better way to describe a bunch of charged particles is to use smooth charge distributions, so called sub-bunches. The shape of the sub-bunches is elliptical and they have a gaussian charge density. Also their electromagnetic fields can be obtained at each observation point by 3D integration. A direct implementation of such a model in tracking codes is, unfortunately, impractical since the calculation effort is very high and only few sub-bunches can be tracked in a reasonable time. To reduce the calculation effort, the 3D sub-bunches are described as a convolution of a 1D longitudinal profile and a two-dimensional (2D) transverse density function. Then the fields can be approximately calculated by 1D integration and the solution of analytical functions [77]. This is called the convolution method. It is implemented in the codes TraFiC^4 and CSRTrack.

When the vertical plane[1] is neglected the integration of the electromagnetic fields can be simplified to a 2D calculation. The formalism is described in [78]. There also its application in a tracking code is outlined.

A third way of calculating the electromagnetic fields is to use a Green's function approach. To obtain the longitudinal and horizontal fields at the observation points the Green's functions are calculated on a 2D mesh which is interpolated in a second step [79]. Calculating the fields on a mesh is a lot less time consuming than 3D integration for all particle to particle interactions and also the time needed for the mesh interpolation is negligible.

We can already see the main difference between these methods. The 1D method uses a very simple calculation of the electromagnetic fields, but can track a complex bunch consisting of some 100000 particles. The 3D method, on the other hand, uses a complex calculation of the fields, but can only track a simple bunch made of some 1000 sub-bunches, even when making use of the convolution method. The calculation effort of the

[1] The horizontal plane is the plane in which the charge distributions are deflected in the dipoles. The vertical plane is perpendicular to it.

2D Green's function method lies in between the other two methods. The resulting fields are more realistic than those obtained with the 1D method and a relatively complicated beam consisting of some 10000 sub-bunches can be tracked.

5.1 Description of the Simulation Methods and their Application in Codes

In chapter 4.2 we have already seen that the energy of the electrons changes due to the coherent synchrotron radiation when they pass a bending magnet. The energy change depends on the position of the electron bunch in the bending magnet and on the position of the electrons with respect to the bunch center. For bunches with a general longitudinal density profile $\lambda(s)$ the rate of energy change due to the longitudinal CSR fields along the magnet is [39]:

$$\frac{dE(s,\alpha)}{c\,dt} \approx -\frac{2e^2}{4\pi\epsilon_0 3^{1/3} R^{2/3}} \left(\left(\frac{24}{R\alpha^3}\right)^{1/3} \left(\lambda\left(s - \frac{R\alpha^3}{24}\right) - \lambda\left(s - \frac{R\alpha^3}{6}\right)\right) + \int_{s-R\alpha^3/24}^{s} \frac{ds'}{(s-s')^{1/3}} \frac{d\lambda(s')}{ds'} \right) \tag{5.1}$$

The first part describes the influence of an entrance transient which overtakes the bunch and fades out in a sufficiently long dipole. The second part describes the transition to the steady state result and reflects that a particle can only be influenced by particles less than a slippage length behind. The CSR fields in a drift behind a bending magnet can also be described analytically within this model [39].

To make use of the analytical formulae at a time t the 3D distribution, which is used in the simulations, is projected onto a reference trajectory $\vec{r}_{\mathrm{ref}}(s,t)$. From this projection the longitudinal charge density $\lambda(s,t)$ is calculated (figure 5.1). Before the density profile can be inserted in the analytical formula one has to make sure that noise due to the limited number of particles is smoothed. Otherwise the results would be artificially distorted. The code CSRTrack uses gaussian 3D sub-bunches for the description of the charge distribution. The user himself has to make sure that the initial distribution of the sub-bunches results in a good profile. When point-like particles are tracked, as in the code Elegant, a smoothing algorithm has to be implemented. The smoothing parameters as well as the number of particles have to be carefully checked in order to make sure that only the noise is suppressed but real density fluctuations are not taken out.

Within this model transverse dependencies of the longitudinal CSR fields and the transverse CSR fields are not taken into account. Since the derivation of the analytical formulae is based on the electromagnetic fields of point-like particles, the singularities in the fields at the positions of the particles had to be removed by a renormalization [39]. This is done by subtracting the longitudinal fields between electrons in uniform linear motion. Thus, only the radiated fields are described and the space charge fields are ignored.

The advantage of the 1D approach is that the effort of the calculations scales linearly with the number of particles or sub-bunches inside the bunch. Very complicated bunches which are built of some 100000 particles or sub-bunches can be tracked on a single CPU.

By numerically integrating the 3D retarded scalar and vector potentials

$$\Phi(\vec{r},t) = \frac{1}{4\pi\epsilon_0} \int \frac{\rho(\vec{r}',t')}{|\vec{r}-\vec{r}'|} dV' \ , \quad \vec{A}(\vec{r},t) = \frac{\mu_0}{4\pi} \int \frac{\vec{J}(\vec{r}',t')}{|\vec{r}-\vec{r}'|} dV'$$

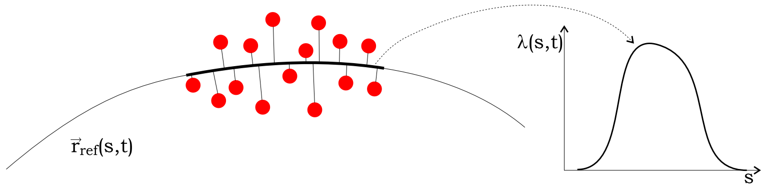

Figure 5.1: *For the 1D field calculation the charge distribution (grey dots) is projected onto a reference path $\vec{r}_{\mathrm{ref}}(s,t)$ to get the longitudinal density profile $\lambda(s,t)$.*

of a bunch consisting of several sub-bunches, the bunch shape, including transverse dimensions, is taken into account correctly. The full 3D fields $\vec{E}(\vec{r},t) = -\vec{\nabla}\Phi(\vec{r},t) - \frac{\partial \vec{A}(\vec{r},t)}{\partial t}$ and $\vec{B}(\vec{r},t) = \vec{\nabla} \times \vec{A}(\vec{r},t)$ are obtained at the time t for an observation point at $\vec{r}$. The space charge fields are included implicitly.

In general, one has to calculate the electromagnetic fields for each sub-bunch acting on every other sub-bunch. The computation effort thus scales with the square of the number of sub-bunches. Since each 3D integration of the potentials is very time consuming, usually approximations are used in simulation codes. Only if the sub-bunches are spherical, can the 3D integrations be reduced to the solution of 1D integrations and analytical functions, without making any approximations [75].

The codes TraFiC[4] and CSRTrack adopt a calculation method that was developed in [77]. A 3D sub-bunch is interpreted as the convolution[2] of a longitudinal 1D profile $\lambda(s,t)$ with a transverse 2D density function $\eta(x,y)$, which is usually chosen to be gaussian (figure 5.2). Then the 3D electromagnetic fields of the sub-bunch can also be calculated by a convolution of 1D fields with the 2D density function:

$$\vec{E}(\vec{r},t) = \eta(x,y) * \vec{E}^{1\mathrm{D}}(\vec{r},t)\ ,\quad \vec{B}(\vec{r},t) = \eta(x,y) * \vec{B}^{1\mathrm{D}}(\vec{r},t)$$

The fields of a 1D line distribution $\vec{E}^{1\mathrm{D}}$, $\vec{B}^{1\mathrm{D}}$ can be split into singular parts $\vec{E}^{1\mathrm{D}}_{\mathrm{s}}$ and $\vec{B}^{1\mathrm{D}}_{\mathrm{s}}$, which are dominated by local effects, and non-singular parts $\vec{E}^{1\mathrm{D}}_{\mathrm{ns}}$ and $\vec{B}^{1\mathrm{D}}_{\mathrm{ns}}$, which depend mainly on long-range interactions:

$$\vec{E}^{1\mathrm{D}}(\vec{r},t) = \vec{E}^{1\mathrm{D}}_{\mathrm{s}}(\vec{r},t) + \vec{E}^{1\mathrm{D}}_{\mathrm{ns}}(\vec{r},t)\ ,\quad \vec{B}^{1\mathrm{D}}(\vec{r},t) = \vec{B}^{1\mathrm{D}}_{\mathrm{s}}(\vec{r},t) + \vec{B}^{1\mathrm{D}}_{\mathrm{ns}}(\vec{r},t)$$

The singular parts can be expressed analytically and the non-singular parts can be calculated numerically [77]. The 3D fields are then given by

$$\begin{aligned}\vec{E}(\vec{r},t) &= \eta(x,y) * \vec{E}^{1\mathrm{D}}_{\mathrm{s}}(\vec{r},t) + \eta(x,y) * \vec{E}^{1\mathrm{D}}_{\mathrm{ns}}(\vec{r},t)\\ &\approx \eta(x,y) * \vec{E}^{1\mathrm{D}}_{\mathrm{s}}(\vec{r},t) + \vec{E}^{1\mathrm{D}}_{\mathrm{ns}}(\vec{r},t)\end{aligned} \tag{5.2}$$

and

$$\begin{aligned}\vec{B}(\vec{r},t) &= \eta(x,y) * \vec{B}^{1\mathrm{D}}_{\mathrm{s}}(\vec{r},t) + \eta(x,y) * \vec{B}^{1\mathrm{D}}_{\mathrm{ns}}(\vec{r},t)\\ &\approx \eta(x,y) * \vec{B}^{1\mathrm{D}}_{\mathrm{s}}(\vec{r},t) + \vec{B}^{1\mathrm{D}}_{\mathrm{ns}}(\vec{r},t)\end{aligned} \tag{5.3}$$

The approximation is justified if the transverse dimensions of the sub-bunch are of the same order or smaller than its length. Then the transverse dependence of the non-singular part is negligible. If the transverse dimensions are larger, the small transverse dependence can be sampled by an interpolation of a few solutions at different transverse coordinates. The

[2]The convolution is denoted with "$*$" in the formulae.

transverse sampling is not implemented in the codes TraFiC[4] and CSRTrack. Therefore the transverse size of the sub-bunches should not be too much larger than their length.

In comparison to the full 3D integration the calculation effort for the fields is reduced by about two orders of magnitude, but the scaling with N^2 is unchanged. Typically some thousand sub-bunches can be tracked this way when several CPUs are used in parallel. For CSR simulations at DESY a LINUX cluster with 22 CPUs can be used. Even on this computer only up to about 10000 sub-bunches can be tracked through a bunch compressor chicane within several days.

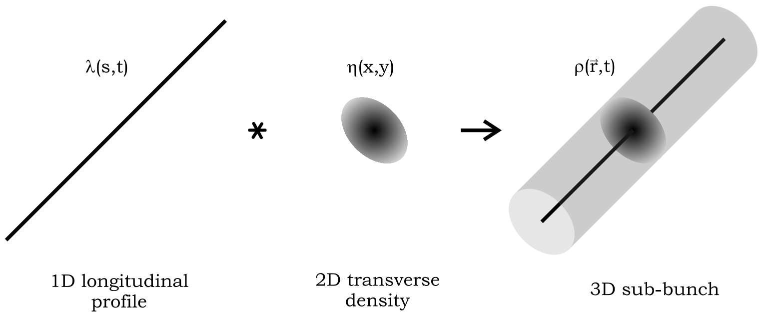

Figure 5.2: *A 3D sub-bunch can be represented as a convolution of a 1D profile and a 2D density function.*

Since the effort for calculating the CSR fields is very high, the number of sub-bunches has to be reduced and a careful modelling of the bunch profile is needed. Random or quasi-random distributions cannot be used since they produce too much noise. A common approach is to describe the bunch by two different distributions. One distribution is the so called generating bunch which is used to calculate the CSR fields. It is tracked self-consistently, i.e. under the influence of its own CSR fields, through the beam line. Usually the generating bunch is just a 1D line distribution of 3D sub-bunches whose distances and lengths are chosen to give a smooth profile. In this case the transverse phase space coordinates of the sub-bunches are zero. The second distribution is the sampling bunch. It consists of randomly distributed point-like particles which are tracked within the fields generated by the generating bunch but do not radiate themselves. Often the sampling bunch represents only a short slice in the center of the generating bunch (figure 5.3).

Splitting the bunch into these two distributions is in many cases in good agreement with the usage of a full 3D generating bunch [67]. But there are also cases where this simplification is not applicable and the transverse phase space of the generating bunch has to be populated (e.g. see chapter 7).

In most cases a lot more than 1000 sub-bunches are needed to populate the full 6D phase space. Thus the applicability of the 3D method is limited unless very many CPUs are available. On the other hand, the very fast 1D method uses overly simple fields. The need for a fast but accurate field calculation is met by the 2D Green's function method [80]. The electromagnetic fields generated by a moving charge distribution, i.e. a sub-bunch, are calculated by using a Green's function approach:

$$\vec{E}_{\mathrm{sb}}(\vec{r},t) = \frac{q_{\mathrm{sb}}}{q_0}\mathbf{M}^{-1}\vec{E}^{(\mathrm{green})}(\vec{r}_{\mathrm{ref}} + \mathbf{M}(\vec{r}-\vec{r}_{\mathrm{sb}}),t)$$
$$\vec{B}_{\mathrm{sb}}(\vec{r},t) = \frac{q_{\mathrm{sb}}}{q_0}\mathbf{M}^{-1}\vec{B}^{(\mathrm{green})}(\vec{r}_{\mathrm{ref}} + \mathbf{M}(\vec{r}-\vec{r}_{\mathrm{sb}}),t)$$

The observation point is at $\vec{r}$ and the sub-bunch of charge q_{sb} is at $\vec{r}_{\mathrm{sb}}$. The Green's

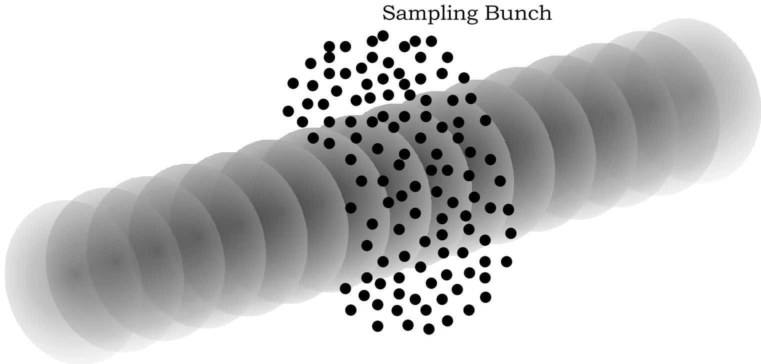

Figure 5.3: *For 2D and 3D simulations the bunch is split into two distributions. The generating bunch consists of sub-bunches which are lined up. The charge of the sub-bunches is adjusted to match the desired charge profile. The generating bunch is used to calculate the electromagnetic fields and it is tracked under the influence of these fields. A second distribution, the sampling bunch, is a random distribution of point-like particles. It is tracked under the influence of the fields which are generated by the generating bunch but does not radiate itself.*

functions $\vec{E}^{(\mathrm{green})}(\vec{r}_\mathrm{g}, t)$ and $\vec{B}^{(\mathrm{green})}(\vec{r}_\mathrm{g}, t)$ describe the electromagnetic fields at a distance $\vec{r}_\mathrm{g} - \vec{r}_\mathrm{ref}$ from a reference charge q_0 travelling on a reference trajectory $\vec{r}_\mathrm{ref}$. By making use of the convolution method, the longitudinal and horizontal electromagnetic fields

$$\begin{aligned}\vec{E}^{(\mathrm{green})}(\vec{r}_\mathrm{g}, t) &= E_x^{(\mathrm{green})}(x, y)\vec{e}_x + E_y^{(\mathrm{green})}(x, y)\vec{e}_y \\ \vec{B}^{(\mathrm{green})}(\vec{r}_\mathrm{g}, t) &= B_z^{(\mathrm{green})}(x, y)\vec{e}_z\end{aligned}$$

of the reference charge are calculated once on a 2D mesh. To get the fields of the reference charge at the position $\vec{r}_\mathrm{g} - \vec{r}_\mathrm{ref}$ of the observation point with respect to the reference charge q_0 the mesh is interpolated. $\vec{r}_\mathrm{g} - \vec{r}_\mathrm{ref}$ is obtained by the shift $\vec{r}_\mathrm{ref}$ and the rotation transformation $\mathbf{M}$. The scaling $\frac{q_\mathrm{sb}}{q_0}$ and the rotation $\mathbf{M}^{-1}$ result in the longitudinal and horizontal electromagnetic fields at the observation point $\vec{r}$ generated by a sub-bunch of charge q_sb moving on its trajectory $\vec{r}_\mathrm{sb}$.

The advantage of the Green's function method is that the convolution method is used only to calculate the electromagnetic fields at the mesh points and not for each interaction between the sub-bunches. The number of mesh points is usually a lot smaller than the square of the number of sub-bunches. The calculation time needed for the interpolations and transformations is small.

For the Green's function method the description of the 3D charge distribution is the same as for the convolution method. However, the Green's function method is fast enough to populate at least the horizontal phase space of the generating bunch. As for the convolution method the transverse size of the sub-bunches is limited. Both methods are implemented in such a way that the sub-bunches always have the same orientation with respect to the bunch trajectory. Due to dispersive effects the bunch itself can be rotated. Thus, the orientation of the sub-bunches with respect to the bunch axis changes and, consequently, an incorrect effective bunch shape is used for the field calculation. For the Green's function method the incorrect orientation of the sub-bunches leads to an additional error in the field calculation. The retarded sub-bunch trajectories which are used in the Green's function solver depend on the sub-bunch orientation. Thus, not only an inaccurate bunch shape but also inaccurate sub-bunch trajectories are assumed for the field calculation. Both errors can be minimized by using sub-bunches with small transverse dimensions. As long as the bending angles of the dipoles are of the order of some degrees, the transverse size of the sub-bunches can be about an order of magnitude larger than their length.

On the other hand, one has to take care that the transverse size of the sub-bunches is not too small. Otherwise the transverse fields get artificially strong close to the sub-bunches. Usually the transverse dimensions of the generating bunch have to be similar to the transverse dimensions of the sampling bunch. Thus, in most cases, at least the horizontal cross section of the generating bunch should be populated with some sub-bunches. Their horizontal size must be large enough that they overlap and give a smooth transverse profile. Their vertical size can be as large as the vertical diameter of the sampling bunch. The initial transverse dimensions of the sampling bunch are given by the initial Twiss parameters.

5.2 Particle Tracking

To include the calculation of the longitudinal CSR field in the code Elegant, special beam line elements were implemented by M. Borland [76]. The point-like particles are tracked through a short slice of these elements without the influence of CSR. In a second step, the CSR fields are calculated based on the particle distribution behind the slice and on the particle trajectories along the slice. It is assumed that the longitudinal distribution is fixed and does not change at retarded times, i.e. the retardation is not taken into account correctly. The effect of the CSR field is applied as an energy kick behind the slice. Since the influence of CSR on beam dynamics within the slice is neglected, the slice length must be very short to reduce the error. Usually each element of the beam line which includes CSR fields has to be cut in $10 - 100$ slices.

The code CSRTrack [67] tracks 3D sub-bunches through a beam line consisting only of drifts and horizontal bending magnets. The field calculation can be either the 1D projected method, the 2D Green's function method or the 3D convolution method. This makes the code very flexible. Unfortunately, an early version of the code was used in this thesis which neglected vertical sub-bunch coordinates. Each tracking step includes a self-consistent loop for the field and trajectory calculation. At a given time t_0 the sub-bunch coordinates and the CSR fields are known. From this the trajectories of the sub-bunches through a slice of the beam line can be extrapolated. Knowing the trajectories of the sub-bunches along the slice makes it possible also to extrapolate the development of the CSR fields. These fields are then used to track the sub-bunches through the slice and the final phase space coordinates are compared to the extrapolated coordinates already obtained. If their difference is smaller than a pre-determined error, the same calculation steps can be repeated for the next beam line slice. Otherwise, the fields and trajectories of the sub-bunches are calculated again, as long as the deviation between two successive tracking steps is too large. If the slice length is small enough convergence should be reached within very few iterations, often already with the first iteration.

The new TraFiC^4 2.0 [81] uses a similar self-consistent tracking algorithm. In the field solver only the convolution method is implemented. The field calculation is almost the same as the convolution part in CSRTrack. Indeed, both field solvers were initially written by M. Dohlus. TraFiC^4 2.0 can track the full 6D phase space coordinates of the sub-bunches through drifts, quadrupoles and bending magnets with an arbitrary orientation in space. That means, not only horizontal but also vertical bends are possible.

The rewriting of TraFiC^4 became necessary after an error in the implementation of the self-consistent loop in the old TraFiC^4 was found. The original idea was to track two distributions by using a leap-frog scheme. One distribution is the generating bunch and the second is initially just a copy of it. These two distributions are than iteratively tracked through each slice of the beam line. If the tracking is not accurate enough both distributions accumulate different errors with each tracking step and eventually they diverge. This of course leads to unusable results.

5.3 Comparison of the Models

Since the three calculation methods are based on different assumptions it is interesting to compare the simulation obtained. A line-distribution is tracked through a single dipole and through a C-chicane. The same initial conditions and chicane settings are used in the simulations which are performed with the code CSRTrack. The distribution has a gaussian charge profile and is compressed from an initial peak current of 500 A to a peak current of 2500 A in the chicane. The total charge of the distribution is 1 nC. The electron energy is 450 MeV.

The three methods result in almost the same longitudinal fields behind a single bending magnet (figure 5.4 a). Also the transverse fields calculated by the Green's function method and the convolution method are the same (figure 5.4 b). But behind the last magnet of a C-chicane the projected method results in considerably different longitudinal fields (figure 5.5 a), whereas the other two methods still show the same results for the longitudinal and the transverse fields (figure 5.5 a and b). The results obtained with the projected method differ because the bunch shape develops differently along the chicane. Accordingly, the shape of the final profile varies from profiles which are obtained with the Green's function method and the convolution method (figure 5.6).

The differences of the methods also become obvious when the longitudinal and transverse phase space distributions behind the C-chicane are compared. The longitudinal phase space distributions are almost the same for the Green's function method and the convolution method. But if the projected method is used the longitudinal phase space distribution is deformed (figure 5.7 a). In the transverse phase space the difference is even more pronounced (figure 5.7 b). Consequently, not only the correlated emittance will be influenced, but also the slice emittance. For the simulations shown here the projected method results in a normalized slice emittance of 0.988 mm mrad and a normalized correlated emittance of 0.982 mm mrad whereas the Green's function method results in 1.042 mm mrad and 1.658 mm mrad. The normalized emittances are 1.037 mm mrad and 1.723 mm mrad if the convolution method is used. When the electron energy increases the deviation of the projected method from the other two methods gets smaller.

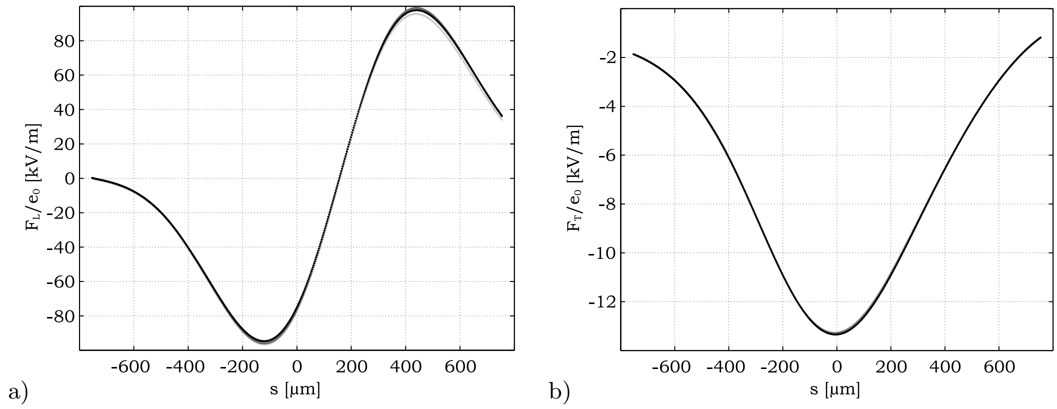

Figure 5.4: *The longitudinal (a) and transverse (b) CSR fields along the bunch are plotted behind a single dipole. The curves which are obtained from the three calculation models agree very well and lie almost on top of each other.*

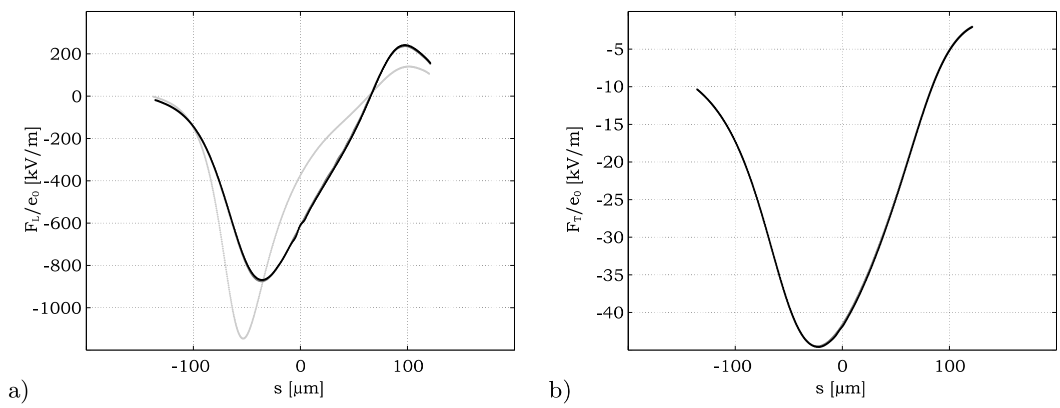

Figure 5.5: *The longitudinal (a) and transverse (b) CSR fields along the bunch are plotted behind a C-chicane. The results obtained with Green's function method (grey) and the convolution method (black) agree very well and lie on top of each other. But the results from the projected method differ (light grey).*

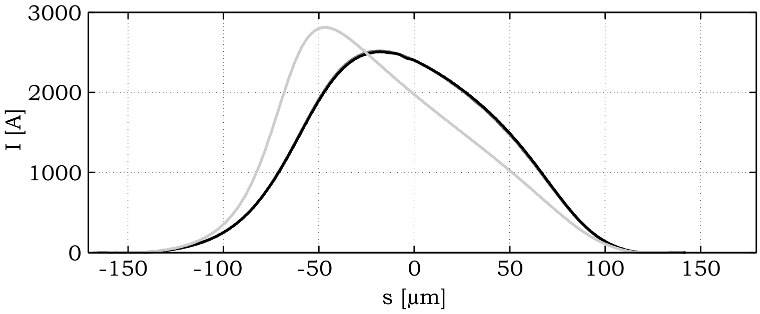

Figure 5.6: *The longitudinal current profile is plotted for an initially gaussian bunch that passed a C-chicane. The results from the Green's function method (grey) and the convolution method (black) are the same. They lie on top of each other. The profile that is obtained with the projected method differs (light grey).*

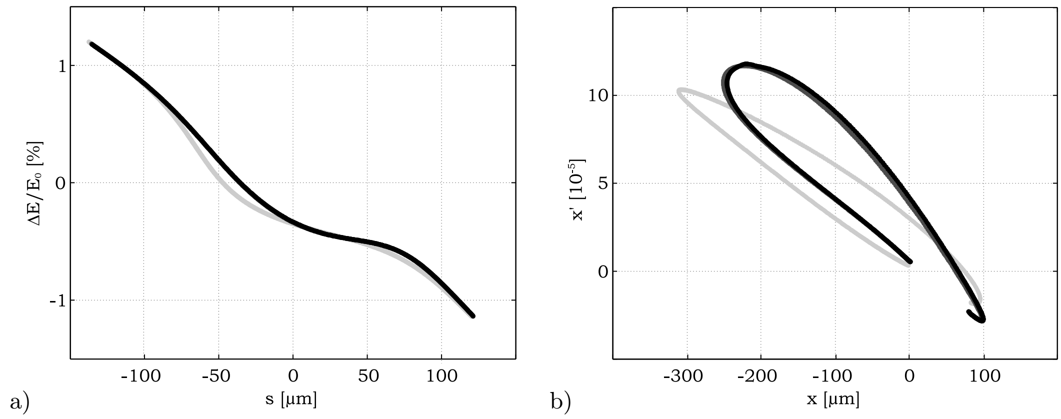

Figure 5.7: *The longitudinal (a) and transverse (b) phase space distributions behind the C-chicane are shown. They are almost the same for the convolution method (black) and the Green's function method (dark grey). The curves lie on top of each other. For the projected method (light grey) the phase space distributions differ.*

Chapter 6

The second Bunch Compressor at TTF2

TTF2 will include two bunch compressors, a C-chicane and an S-chicane. These two chicanes have to compress the electron bunches longitudinally to achieve the required peak current of up to 2500 A. At the same time they have to be flexible enough to also deliver bunches with only about 500 A peak current. The first compression stage is based on the bunch compressor 2 (BC2) which was already used at TTF1. The second stage is a new bunch compressor called BC3. Requirements on the electron beam and design constraints for BC3 are given in the first section of this chapter. Also the geometries of the simulated chicanes are described there. The different chicanes are compared in section 6.2. Simulation results for different initial electron distributions and chicane settings are given. It is shown, that a symmetric 6-bend S-chicane matches our requirements very well. Section 6.3 describes some technical aspects of BC3 and gives an overview of the whole bunch compressor beam line including diagnostics and other components.

6.1 Requirements on the Electron Beam and Remarks on the Chicane Layouts

The requirements on performance and beam quality of the TTF2 linac are determined by the VUV-FEL (see also chapter 2). It is foreseen that the FEL will cover a wavelength range from $\lambda = 6.4$ nm to $\lambda = 120$ nm [14]. For this purpose the beam energy has to be tunable from $E_0 = 1000$ MeV to $E_0 = 230$ MeV. A bunch peak current of $I = 2500$ A is needed to produce laser-like radiation with wavelengths smaller than $\lambda = 30$ nm. In this case the electron bunches with a charge of 1 nC have to be compressed to an rms length of 50 μm, assuming a gaussian charge distribution. A normalized transverse emittance lower than 2 mm mrad and a total rms energy spread of less than 1 MeV have to be preserved throughout the whole linac. In reference [14] various other operational modes are described, but the values given here are the most challenging ones. Therefore I will focus on these in my comparison.

As a starting point for the design of BC3 the nominal conditions have been defined. Gaussian electron bunches are compressed from an rms length of 250 μm to 50 μm. This change in bunch length is achieved with $R_{56} = -5$ cm and $\frac{\sigma_E}{E_0} = 0.004$. To keep some flexibility for different operational modes the R_{56} should be tunable in the range of -2.5cm to -10 cm. Since the R_{56} has mainly a quadratic dependence on the bending angle, it has to be possible to change the bending angle of the dipoles by a factor of two. The nominal beam energy at the entrance of BC3 is $E_0 = 450$MeV. The relative rms uncorrelated energy spread in front of BC3 is assumed to be $\frac{\sigma_\epsilon}{E_0} = 1 \cdot 10^{-4}$ and the normalized transverse slice emittance is assumed to be $\varepsilon_x = 1$ mm mrad.

The length of the full BC3 section is limited to 21.9 m since it is located between the accelerating modules ACC3 and ACC4. Some of this space is needed for quadrupoles, steerers and diagnostics both in front of and behind the magnetic chicane. For the chicane itself therefore only 14 m can be used.

Within these boundary conditions different chicane layouts are compared. They all have the same overall length of 14 m. Since the peak current rather than the bunch length is important for the FEL, the bending angles are slightly adjusted so that all chicanes compress the bunch to the same final peak current. This means, the deformation of the longitudinal phase space due to the CSR fields is taken into account in the simulation settings.

The work on BC3 was started by A. Loulergue and A. Mosnier from CEA Saclay (Commisariat à l'Energie Atomique in Saclay, France). They compared some bunch compressor chicanes in computer simulations and gave a recommendation for BC3 [82, 83, 84, 85]. The comparison made within my thesis covers not only these chicanes but also includes some additional layouts. For my comparison all layouts and the initial electron distributions match the constraints discussed earlier. Since it was proposed to use dipoles for BC3 which have the same design and the same properties as the BC2 dipoles, all simulations are based on dipoles of 0.5 m length. The gap height of these dipoles is $H = 25$ mm and sets a limit on the maximum possible vacuum chamber height. More information on the dipoles is given later in this chapter.

Some basic features of the chicanes which I compare within my thesis were discussed in chapters 3 and 4. Sketches of the chicanes are shown in figure 3.4. Here I will only point out some properties of the chicanes which were simulated. The symmetric C-chicane uses four dipoles of equal strength. For the symmetric 4-bend S-chicane the two central dipoles have twice the strength of the outer two dipoles. In the asymmetric 4-bend S-chicane the two central dipoles are shifted by $\Delta l = 0.6$ m towards the end of the chicane. The bending angles of the dipoles remain unchanged. Splitting the central dipoles of both S-chicanes in pairs of dipoles leads to the 6-bend S-chicanes. All six magnets have the same strength. The asymmetric 4-bend S-chicane proposed by A. Loulergue and A. Mosnier with dipoles of 0.3 m (outer dipoles) and 0.6 m (inner dipoles) length was also simulated. This layout is 0.26 m longer than the other chicanes. Asymmetric layouts with modified bending angles were initially not simulated and were therefore not taken into account for the comparison on which the decision for BC3 is based. But to get a complete comparison, simulations of an asymmetric C-chicane and a 6-bend S-chicane with modified bending angles were performed later. The lengths of dipoles and drifts[1] for the various chicanes are given in table 6.1. To distinguish the two asymmetric cases of the 6-bend S-chicane the case where the bending angles of the six dipoles are the same is called first asymmetric case (AC1) and the case where the bending angles of the dipoles differ is called second asymmetric case (AC2). The longitudinal dipole offset of $\Delta l = 0.6$ m, which is used for three of the asymmetric chicanes, was found to be a good solution in ref. [83]. This value agrees well with an estimation I performed later. It makes use of eqn. (4.23) and results in a value of 0.35 m (see chapter 4.3).

6.2 Simulations of the Bunch Compressor Chicanes

The comparison of the different chicanes presented in this section is divided into two parts. The first part compares simulation results of the chicanes with the nominal settings which were given in the previous section. The only parameter variation that was done is a variation of the chamber height. In the second part additional simulations were performed with different chicane settings and electron bunch parameters.

[1]The length of a magnet is the yoke length and not the arc length. With the length of a drift I always mean the length of the projection onto the Z-axis (see figures 3.5 and 3.6). Therefore both values are independent of the bending angle.

	C-chicanes		S-chicanes					Saclay
			4 bends		6 bends			S-chicane
	sym.	asym.	sym.	asym.	sym.	AC1	AC2	
L_B [m]	0.5	0.5	0.5	0.5	0.5	0.5	0.5	0.3/0.6
L_{12} [m]	5.75	5.15	2.875	6.475	2.375	2.975	2.375	3.64
L_{23} [m]	0.5	0.5	6.2495	6.2495	0.5	0.5	0.5	6.3797
L_{34} [m]	5.75	6.35	2.875	2.275	5.2495	5.2495	5.2495	2.44
L_{45} [m]	-	-	-	-	0.5	0.5	0.5	-
L_{56} [m]	-	-	-	-	2.375	1.775	2.375	-

Table 6.1: *For the different chicanes the lengths of the dipoles and the drift spaces are given. See figures 3.5 and 3.6 for the nomenclature.*

6.2.1 Initial Simulations for BC3

The electron distribution was created by tracking a particle distribution from the RF gun up to 1m in front of the entrance of BC3 with the computer code ASTRA [86]. For the CSR simulations the 3D distribution was projected to a 1D line distribution [87]. It has a peak current of about 400 A. The rms bunch length is $\sigma_s = 266\,\mu$m and the relative rms energy spread is $\frac{\sigma_E}{E_0} = 0.004$. The current profile is not gaussian. The bunch parameters allow a compression to a peak current of 2500 A with an R_{56} close to -5 cm. The distribution consists of 405 sub-bunches. The basic bunch parameters and the initial longitudinal phase space distribution are shown in figure 6.1. In the simulations this distribution was used only to generate the CSR fields. Thus, it is called the generating bunch.

To calculate the transverse slice emittance and the slice energy spread, a short sampling bunch was generated which consists of randomly distributed test particles in the middle of the generating bunch. It has an initial length of $10\,\mu$m and an uncorrelated energy spread of 10^{-4}. The energy slope along the slice is the same as the energy slope in the middle of the generating bunch. The slice was tracked inside the fields which were generated by the generating bunch but does not generate any electromagnetic fields itself. The transverse density distribution of the slice is gaussian (figure 6.2). The initial Twiss parameters of the slice 1 m in front of the chicane are taken from TTF2 beam optics data. The values are $\beta_x = 75.52$ m, $\alpha_x = 5.36$, $\beta_y = 51.29$ m and $\alpha_y = 2.82$. The normalized slice emittance is $\varepsilon_x = 1$ mm mrad. Since the slice only contains 501 randomly distributed electrons it does not match these values exactly.

To estimate the effect of shielding, simulations of the symmetric 6-bend S-chicane were performed with different heights of the vacuum chamber. The maximum height is given by the gap height of the magnets. Since some of the space is needed for the chamber walls the maximum inner height is 15 mm.

The simulations were done with the old version of the code TraFiC^4 (see chapter 5). The projected emittance is calculated from a convolution of the generating bunch and the sampling bunch (see chapter 4.1).

6.2.1.1 Simulation Results

The simulation results for the horizontal emittances as well as the slice and the total energy spread are summarized in table 6.2. The growth of the correlated and the projected emittance is much higher in the C-chicanes than in the S-chicanes. Also the slice emittance grows more in the C-chicanes. The values of the slice energy spread and the total energy spread are similar for all chicanes. This matches the expectations from chapter 4.3.

When comparing the results for the various chicanes it becomes obvious that the asym-

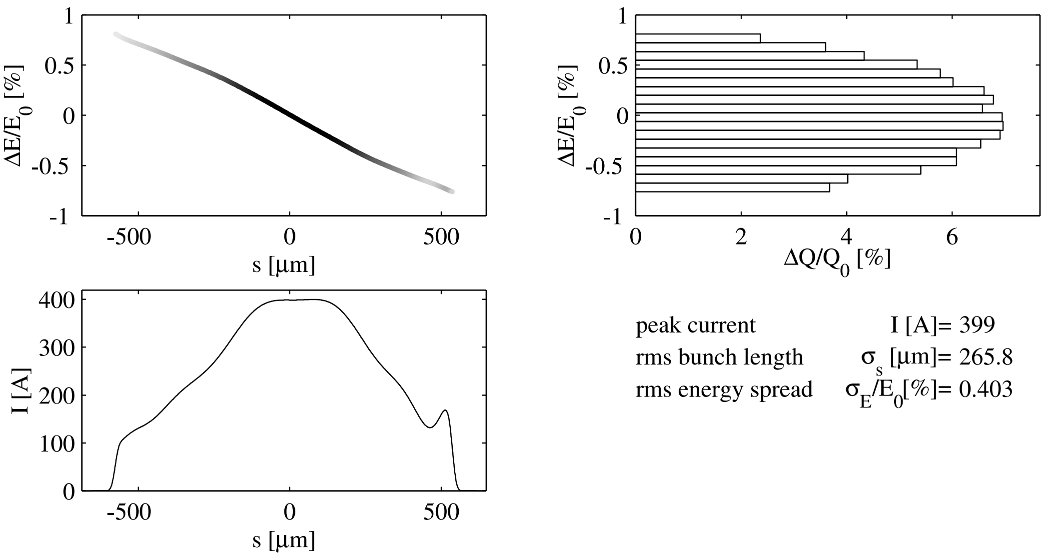

Figure 6.1: *Shown here are the longitudinal phase space distribution of the generating bunch (upper left), its energy distribution (upper right) and its current profile (lower left). In the upper left plot bright dots represent sub-bunches with a low charge and dark dots represent sub-bunches with a high charge.*

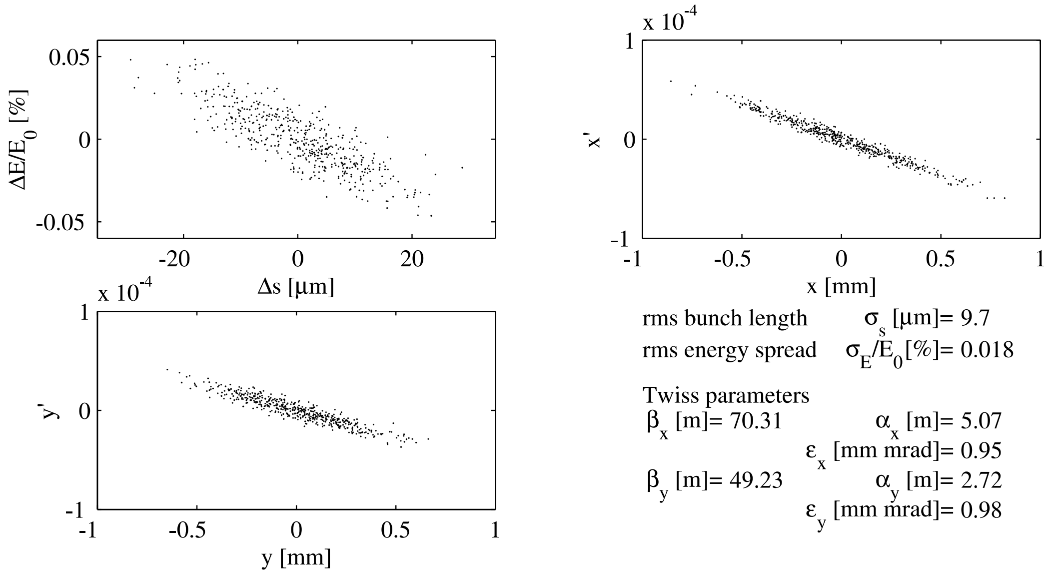

Figure 6.2: *The longitudinal (upper left), horizontal (upper right) and vertical (lower left) phase space distributions of the sampling bunch are plotted.*

metric chicanes have only a slight advantage. Also the difference between 4-bend and 6-bend chicanes is small. The growth of the emittance in the vertical phase space is very similar for all chicanes (table 6.3).

	slice emit. [mm mrad]	corr. emit. [mm mrad]	proj. emit. [mm mrad]	slice $\frac{\sigma_E}{E_0}$ $[10^{-4}]$	total $\frac{\sigma_E}{E_0}$ $[10^{-3}]$
initial values	0.952	0.009	1.001	1.797	4.030
Saclay S-chicane	1.054	0.389	2.255	2.806	3.820
4-bend S-ch. asym.	1.050	0.411	2.243	2.729	3.814
6-bend S-ch. AC1	1.061	0.554	2.557	2.998	3.747
4-bend S-ch. sym.	1.065	0.386	2.386	2.772	3.821
6-bend S-ch. sym.	1.067	0.509	2.724	2.897	3.753
C-chicane sym.	1.146	1.541	4.172	3.137	3.975
C-chicane asym.	1.142	1.453	4.089	3.143	3.965
6-bend S-ch. AC2	1.072	0.510	2.420	3.061	3.746

Table 6.2: *The horizontal normalized emittances as well as the slice energy spread and the total energy spread calculated from the simulation results for the different chicanes.*

	slice emit. [mm mrad]	proj. emit. [mm mrad]
initial values	0.983	0.990
Saclay S-chicane	1.011	1.050
4-bend S-chicane asym.	1.012	1.052
6-bend S-chicane AC1	1.014	1.059
4-bend S-chicane sym.	1.010	1.046
6-bend S-chicane sym.	1.012	1.054
C-chicane sym.	1.016	1.045
C-chicane asym.	1.018	1.044
6-bend S-chicane AC2	1.015	1.059

Table 6.3: *The vertical normalized emittances behind the different chicanes are given.*

In figures 6.3 and 6.4 the final longitudinal phase space distributions of the generating bunch behind the symmetric C-chicane and the symmetric 6-bend S-chicane are shown. The differences are very small. But when the horizontal phase space distributions are compared the difference between the two chicanes becomes obvious (figure 6.5). Behind the C-chicane the area occupied by the distribution in the horizontal phase space is larger than the area occupied behind the S-chicane. Hence, the transverse emittance is larger behind the C-chicane. Figures 6.3 and 6.4 also show that it could be possible to compress the bunch further and to achieve a higher peak current. The minimum bunch length is limited by the uncorrelated energy spread. Since the strength of the CSR fields scales with the peak current, they will dilute the transverse emittance more strongly when the peak current increases. Additionally, the absolute jitter of the peak current due to jitter in the mean energy or the energy slope will increase.

For all simulations the bending angles of the magnets have been adjusted to closely match a final peak current of 2500 A (see table 6.4).

The influence of the shielding (see chapter 4.4) due to the conducting walls of the vacuum chamber on the emittances and the energy spread is shown in figure 6.6. The simulations were done for a symmetric 6-bend S-chicane. Since the total radiation power is smaller in flat chambers, the correlated and the projected emittance drop. The slice emittance and the slice energy spread are almost independent of the chamber height. Also the total rms energy spread shows only a weak dependence on chamber height. It is always higher than for the unshielded case.

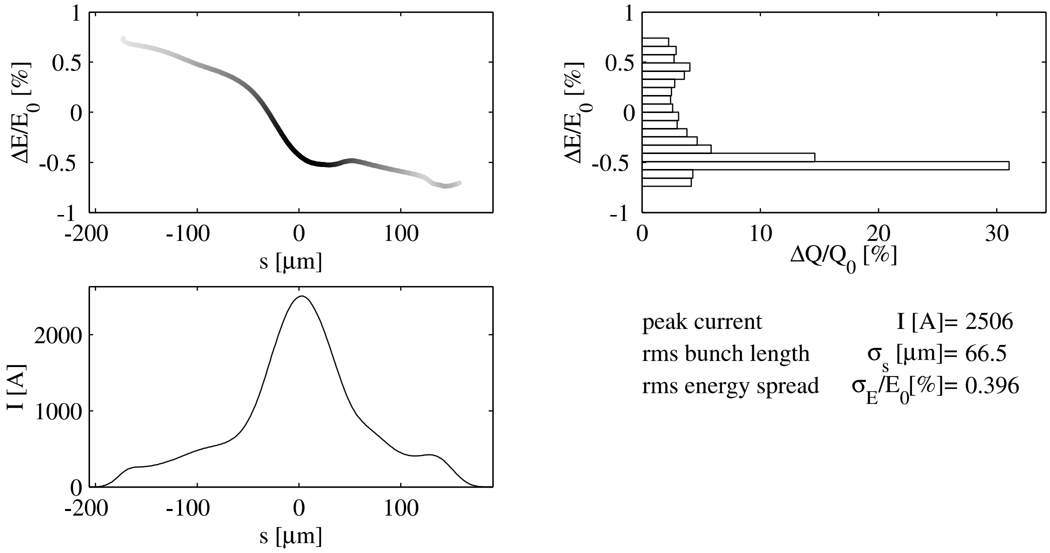

Figure 6.3: *The longitudinal phase space distribution (upper left), the energy distribution (upper right) and the current profile (lower left) are shown for a bunch that passed the symmetric C-chicane. In the upper left plot bright dots represent sub-bunches with low charge and dark dots represent sub-bunches with high charge.*

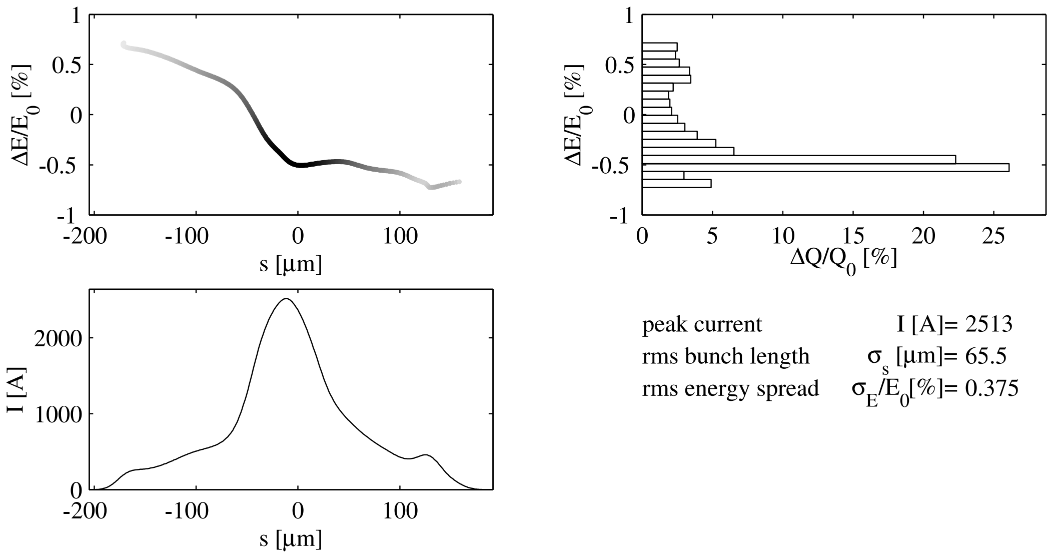

Figure 6.4: *The longitudinal phase space distribution (upper left), the energy distribution (upper right) and the current profile (lower left) are shown for a bunch that passed the symmetric 6-bend S-chicane. In the upper left plot bright dots represent sub-bunches with low charge and dark dots represent sub-bunches with high charge.*

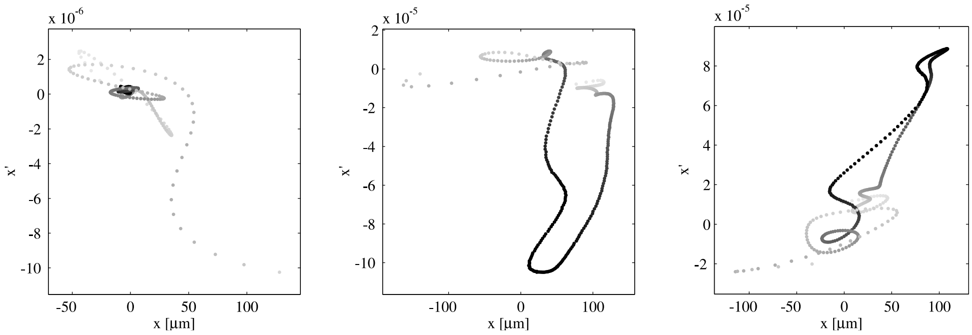

Figure 6.5: *The initial horizontal phase space distribution of the generating bunch is shown in the left plot. The horizontal phase space distribution behind a symmetric C-chicane is shown in the middle plot and the right plot shows the horizontal phase space distribution behind a symmetric 6-Bend S-chicane. Bright dots represent sub-bunches with a lower charge than dark dots.*

	bending angles [deg]	R_{56} [cm]	I_{peak} [A]
Saclay S-chicane	3.57/7.14	−5.10	2519
4-bend S-chicane asym.	3.63/7.26	−5.11	2530
6-bend S-chicane AC1	3.91	−5.15	2519
4-bend S-chicane sym.	3.63/7.26	−5.11	2529
6-bend S-chicane sym.	3.91	−5.15	2513
C-chicane sym.	3.69	−5.07	2508
C-chicane asym.	4.06/3.35	−5.06	2506
6-bend S-chicane AC2	4.30/3.90/3.50	−5.15	2517

Table 6.4: *For the different chicanes the bending angles of the dipoles, the R_{56} and the final peak current of the generating bunch are given.*

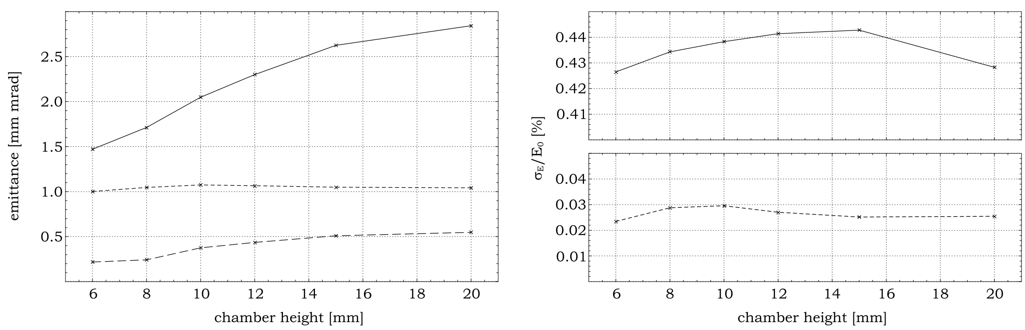

Figure 6.6: *In the left plot the normalized slice emittance (short dash), the normalized correlated emittance (long dash) and the normalized projected emittance (solid) are given for different heights of the vacuum chamber. The right plots show the total energy spread (upper right) and the slice energy spread (lower right) for different chamber heights.*

Based on the simulation results presented here, a symmetric 6-dipole S-shaped chicane was found to be a good compromise between different constraints. The reduction of the emittance growth in the asymmetric chicanes is insignificant. Also the difference between a 4-bend S-chicane and a 6-bend S-chicane is insignificant. The growth of the projected emittance and to a certain extent that of the slice emittance is considered to be too high only for the C-chicanes.

The influence of the vacuum chamber was simulated only for the symmetric 6-bend S-chicane. It was decided to use a vacuum chamber at BC3 with an inner height of 8 mm. The stronger shielding of the CSR due to the vacuum chamber (see chapter 4.4) reduces the projected and correlated emittances by about 30% in comparison to a vacuum chamber with the maximum possible height of 15 mm.

6.2.2 Simulations with different Chicane Settings and Bunch Parameters

For a comparison of the different chicanes with a larger range of settings gaussian distributions were used to generate the CSR fields. The value of the R_{56} was varied and also the dependence of the final longitudinal and transverse phase space distributions on the bunch charge was studied. These simulations were done with the computer code CSRTrack and make use of the Green's function method (see chapter 5).

In the simulations of the chicanes with different values of R_{56} the generating bunch has an initial length of $\sigma_{\rm s} = 250\ \mu$m and consist of 601 equally spaced sub-bunches. Each sub-bunch has a length of $\sigma_{\rm sb} = 2.5\ \mu$m and the distance between their centers is also $2.5\ \mu$m. The charge of the sub-bunches is matched to obtain a gaussian profile in the longitudinal direction with a peak current of 500 A. The full distribution has a length of $\pm 3\sigma_{\rm s}$. The linear energy slope $\frac{dE}{ds}$ along the bunch is adjusted so that the chicanes always compress the bunch to a peak current of 2500 A.

When the charge is varied the bunch length is adjusted accordingly to always achieve the same initial peak current of 500 A. The longitudinal phase space of a 1 nC bunch of $250\ \mu$m rms length is plotted in figure 6.7.

The sampling bunches for the emittance calculation always consist of 1000 normally distributed particles (figure 6.8). All simulations use the same Twiss parameters 1.0 m in front of the chicane. The horizontal values are the same as before: $\beta_x = 75.52$ m, $\alpha_x = 5.36$. Vertical phase space coordinates are not tracked by the version of the code CSRTrack used in this thesis. The sampling bunch has an initial length of $10\ \mu$m and an uncorrelated energy spread of 10^{-4}. The energy slope along the slice is the same as the energy slope along the generating bunch.

6.2.2.1 Comparison of the Chicanes for various R_{56}

To check the influence of the strength of the bending magnets on the phase space development, the R_{56} of the chicanes was chosen as -2.5cm, -5cm and -10cm in the simulations. The energy slope was simultaneously changed from $\frac{1}{E_0}\frac{dE}{ds} = -32\,\mathrm{m}^{-1}$ to $\frac{1}{E_0}\frac{dE}{ds} = -16\,\mathrm{m}^{-1}$ and $\frac{1}{E_0}\frac{dE}{ds} = -8\,\mathrm{m}^{-1}$ to keep the compression factor the same. These values correspond to a total relative energy spread of the generating bunch of $\frac{\sigma_{\rm E}}{E_0} = 0.008$, $\frac{\sigma_{\rm E}}{E_0} = 0.004$ and $\frac{\sigma_{\rm E}}{E_0} = 0.002$. The bending angles are slightly adjusted so that the final peak current is always about 2500 A (table 6.5).

In figure 6.9 the dependence of the normalized emittances and the slice energy spread on the R_{56} is plotted. The emittances produced by the C-chicanes show a stronger dependence on the R_{56} than those produced by the S-chicanes. As long as the R_{56} is small the

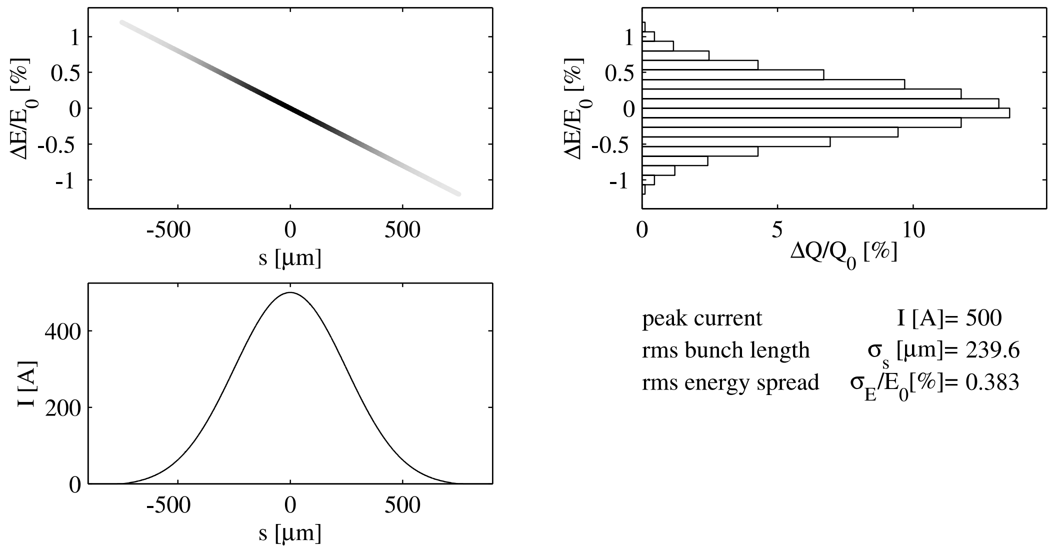

Figure 6.7: *The initial longitudinal phase space distribution of the generating bunch is shown (upper left). Also the energy distribution (upper right) and the current profile (lower left) are plotted. Bright dots represent sub-bunches with lower charge than dark dots.*

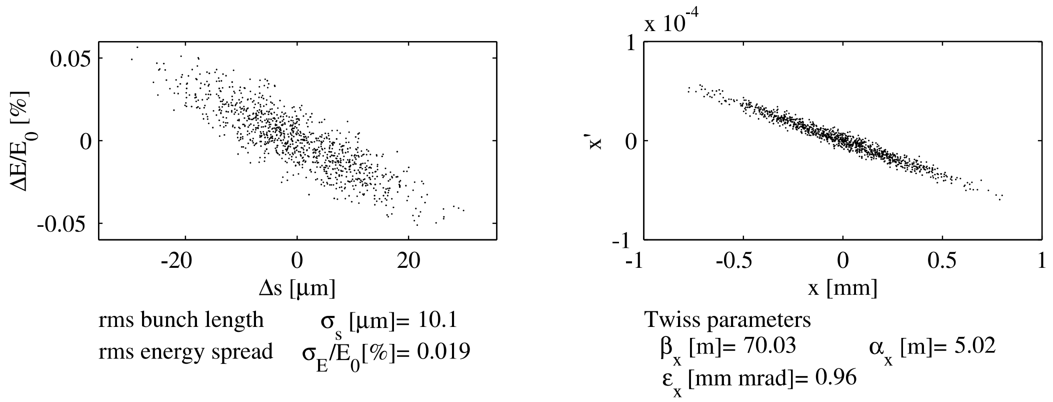

Figure 6.8: *The initial longitudinal (left) and transverse (right) phase space distributions of the sampling bunch are plotted.*

	bending angles [deg]		
	$R_{56} = -2.5$ cm	$R_{56} = -5$ cm	$R_{56} = -10$ cm
Saclay S-chicane	2.53/5.06	3.59/7.18	4.94/9.88
4-bend S-ch. asym.	2.57/5.14	3.64/7.28	5.01/10.02
6-bend S-ch. AC1	2.77	3.91	5.32
4-bend S-ch. sym.	2.57/5.14	3.64/7.28	5.01/10.02
6-bend S-ch. sym.	2.77	3.90	5.31
C-chicane sym.	2.62	3.74	5.24
C-chicane asym.	2.88/2.38	4.11/3.39	5.76/4.75
6-dip. S-ch. AC2	3.15/2.75/2.35	4.29/3.89/3.50	5.70/5.30/4.91

Table 6.5: *The bending angles of the dipoles in the different chicanes are given for the different values of* R_{56}.

emittances are very similar for all chicanes. But if the R_{56} is increased the emittances behind the C-chicanes grow faster than those behind the S-chicanes. The slice energy spread develops similarly for all chicanes. The differences between the symmetric and the asymmetric chicanes as well as between the 4-bend and 6-bend S-chicanes are small. All results agree well with the results obtained in the previous section. It is also confirmed that for BC3 a symmetric 6-bend S-chicane is a good choice. The simulation results for the three R_{56} values are summarized in tables 6.6, 6.7 and 6.8. The slice emittance and the slice energy spread are the emittance and the energy spread of the sampling bunch. Thus, the slice energy spread changes with the energy slope.

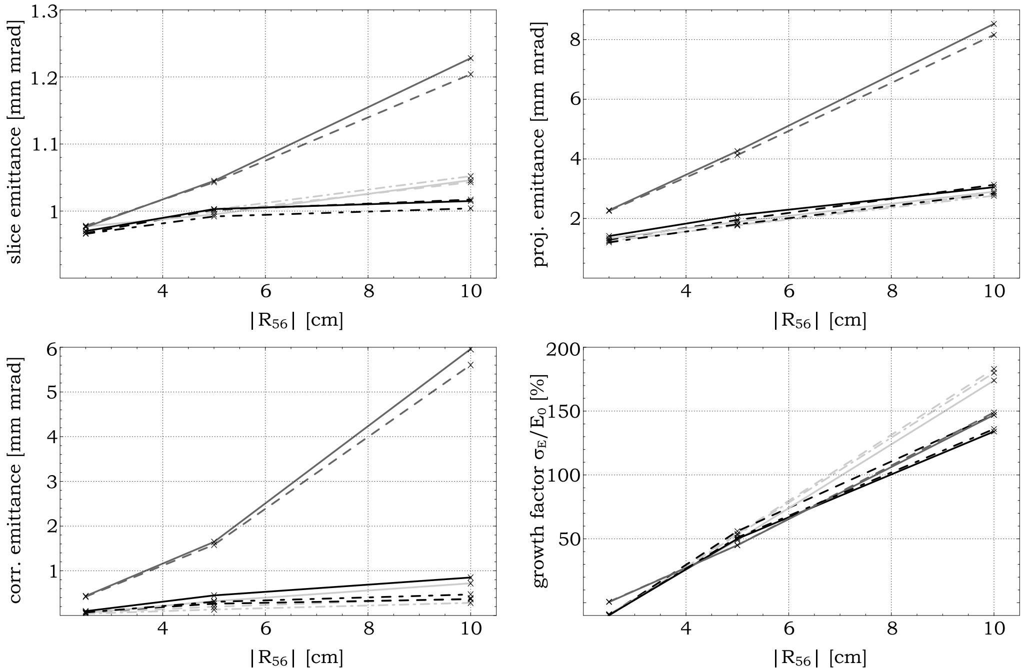

Figure 6.9: *Plots of the normalized slice emittance (upper left), the normalized projected emittance (upper right), the normalized correlated emittance (lower left) and the growth factor of the slice energy spread (lower right) in dependence of the R_{56} are given. The results for the 6-bend S-chicanes are shown in black, the results for the C-chicanes are shown in dark grey and for the 4-bend S-chicanes the results are shown in light grey. Asymmetric chicanes are marked with a dashed line and symmetric designs are marked with a solid line.*

	slice emit. [mm mrad]	corr. emit. [mm mrad]	proj. emit. [mm mrad]	slice $\frac{\sigma_E}{E_0}$ $[10^{-4}]$	total $\frac{\sigma_E}{E_0}$ $[10^{-3}]$
initial values	0.959	0.0	0.959	3.398	7.668
Saclay S-chicane	0.970	0.040	1.244	3.083	7.093
4-bend S-ch. asym.	0.971	0.052	1.245	3.078	7.086
6-bend S-ch. AC1	0.967	0.075	1.289	3.068	6.973
4-bend S-ch. sym.	0.977	0.059	1.336	3.094	7.100
6-bend S-ch. sym.	0.970	0.096	1.410	3.069	6.990
C-chicane sym.	0.976	0.435	2.275	3.414	7.249
C-chicane asym.	0.978	0.420	2.254	3.426	7.243
6-bend S-ch. AC2	0.966	0.068	1.197	3.066	6.989

Table 6.6: *The normalized emittances as well as the slice energy spread and the total energy spread are given for the case of $R_{56} = -2.5$ cm.*

	slice emit. [mm mrad]	corr. emit. [mm mrad]	proj. emit. [mm mrad]	slice $\frac{\sigma_E}{E_0}$ $[10^{-4}]$	total $\frac{\sigma_E}{E_0}$ $[10^{-3}]$
initial values	0.959	0.0	0.959	1.911	3.834
Saclay S-chicane	1.002	0.133	1.765	2.926	3.044
4-bend S-ch. asym.	0.999	0.197	1.775	2.943	3.032
6-bend S-ch. AC1	1.002	0.263	1.949	2.976	2.898
4-bend S-ch. sym.	0.995	0.320	1.886	2.839	3.052
6-bend S-ch. sym.	1.003	0.448	2.106	2.875	2.923
C-chicane sym.	1.045	1.645	4.259	2.764	3.412
C-chicane asym.	1.043	1.581	4.128	2.777	3.400
6-bend S-ch. AC2	0.992	0.305	1.805	2.890	2.913

Table 6.7: *The normalized emittances as well as the slice energy spread and the total energy spread are given for the case of* $R_{56} = -5\,\text{cm}$.

	slice emit. [mm mrad]	corr. emit. [mm mrad]	proj. emit. [mm mrad]	slice $\frac{\sigma_E}{E_0}$ $[10^{-4}]$	total $\frac{\sigma_E}{E_0}$ $[10^{-3}]$
initial values	0.950	0.0	0.950	1.251	1.917
Saclay S-chicane	1.052	0.283	2.763	3.504	1.184
4-bend S-ch. asym.	1.043	0.386	2.838	3.539	1.174
6-bend S-ch. AC1	1.017	0.365	3.132	3.085	1.160
4-bend S-ch. sym.	1.046	0.720	2.898	3.433	1.164
6-bend S-ch. sym.	1.015	0.849	3.051	2.928	1.136
C-chicane sym.	1.228	5.961	8.531	3.088	1.648
C-chicane asym.	1.204	5.603	8.160	3.113	1.627
6-bend S-ch. AC2	1.004	0.471	2.838	2.949	1.137

Table 6.8: *The normalized emittances as well as the slice energy spread and the total energy spread are given for the case of* $R_{56} = -10\,\text{cm}$.

6.2.2.2 Charge dependence of the final Phase Space Distribution

In chapter 4.2 we have seen that the CSR fields depend on the total charge of the bunch. Consequently, the effect of charge variation was studied. Simulations of the symmetric C-chicane and the symmetric 6-bend S-chicane were performed with a bunch charge of $q_{tot} = 0.5\,\text{nC}$, 1 nC, 2 nC and 3 nC. The charge variation was obtained by changing the bunch length but keeping the initial peak current at 500 A. Two cases are distinguished. For the first comparison the energy slope $\frac{dE}{ds}$ and the R_{56} are kept constant. The total energy spread changes in proportion to the bunch length. In the second comparison the total energy spread is constant and thus the energy slope and the R_{56} have to be adjusted accordingly. The compression factor is always 5.

If the bunch charge is varied but the energy slope is kept constant, a strong influence on the shape of the final longitudinal phase space distribution and the profile is observed (figure 6.10). A peak develops in the profile when the charge decreases. The reason for this behavior is that the total energy spread decreases when the bunch charge decreases and the energy spread which is induced by the CSR fields becomes more dominant. The total strength of the CSR fields should decrease when the bunch charge decreases since the field strength is proportional to $\frac{q_{\text{tot}}^2}{\sigma_s^{4/3}}$ (see eqn. (4.3)).

If the total energy spread is kept constant during the charge variation the final longitudinal phase space distributions and profiles do not show a strong dependence on the charge (figure 6.11). But now not only the bunch length but also the R_{56} has to be increased when the bunch charge increases to keep the final peak current at 2500 A. Consequently, also the CSR fields depend more strongerly than before on the charge variation since they scale proportional to $\frac{q_{\mathrm{tot}}^2 R_{56}^{1/3}}{\sigma_{\mathrm{s}}^{4/3}}$ (see eqn. (4.3)). The dependence on the bending radius $\frac{1}{R^{2/3}}$ is replaced by $R_{56}^{1/3}$ (see eqn. (3.23), (3.40), (3.43)).

Since the charge variation has a different influence on the CSR fields for the two cases which were discussed, also a different influence on the transverse emittance can be expected. When the energy slope is constant the emittances and the enlargement of the slice energy spread decrease slowly with increasing charge (figure 6.12). On the other hand, if the total energy spread stays constant and the R_{56} is varied with the charge the increasing CSR fields lead to a growth of the emittance when the charge increases (figure 6.13). An S-chicane is always a better choice than a C-chicane.

The two comparisons show that in terms of the emittance and the slice energy spread it is preferable to keep the total energy spread of the bunch constant and to vary the R_{56} of the chicane when the bunch charge is lowered below 1 nC. But if the bunch charge should be increased above 1 nC, it is a better choice to keep the R_{56} constant and to vary the energy spread of the bunch. Unfortunately, then also the total energy spread of the bunch increases. Since the energy spread has a strong correlated contribution the spectral width of the FEL increases (see chapter 2). This limits the maximum allowed energy spread.

In the comparison of differently charged bunches the initial normalized slice emittance was always assumed to be 1 mm mrad. This is of course not true since the emittance is strongly influenced by the space charge fields in the RF gun and the first accelerating module. One can expect that the emittance of bunches with a low charge will be smaller than the emittance of bunches with a high charge. Accordingly, it might be interesting to decrease the charge when operating the VUV-FEL. As we have seen in the second comparison (figure 6.13), it is possible to compress short bunches with a low charge to the desired peak current of 2500 A without diluting the transverse emittance too much.

A jitter in the bunch charge can be produced by the RF gun in two ways. First, the bunch shape is constant and the peak current changes. Then the emittance and the energy spread will jitter correspondingly. Second, the bunch shape changes and the peak current is constant. This case is similar to the first comparison I made in this section. The peak current will be stable but the emittance increases with decreasing charge.

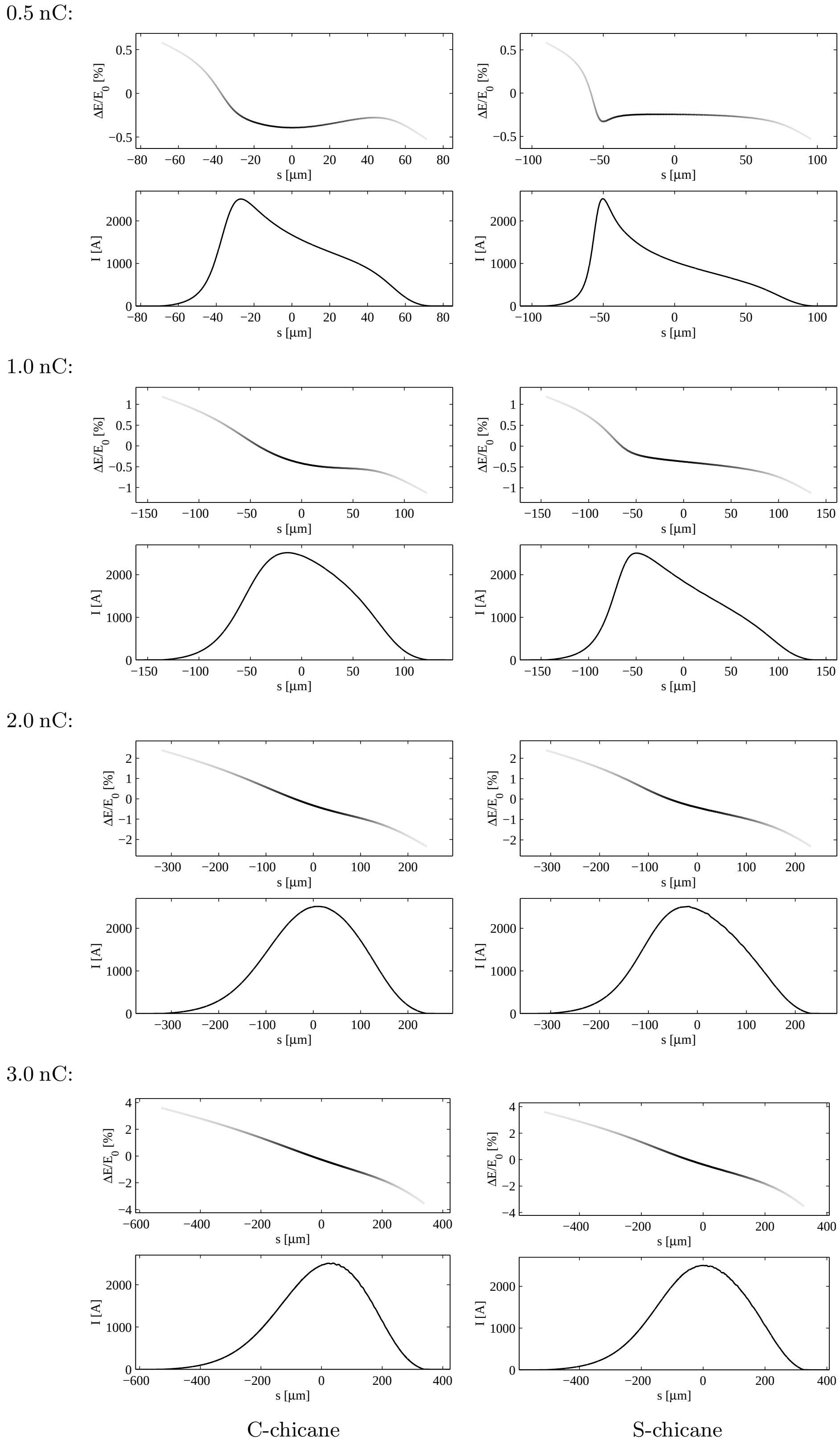

Figure 6.10: *The final longitudinal phase space distributions and the current profiles are given for bunch charges of* $q_{\text{tot}} = 0.5,\ 1.0,\ 2.0,\ 3.0\,\text{nC}$. *The left column shows the results behind a C-chicane and the right column shows the results behind an S-chicane. The initial energy slope* $\frac{dE}{ds}$ *is the same for all simulations. In the phase space plots sub-bunches with a high charge are represented by darker dots than sub-bunches with lower charge.*

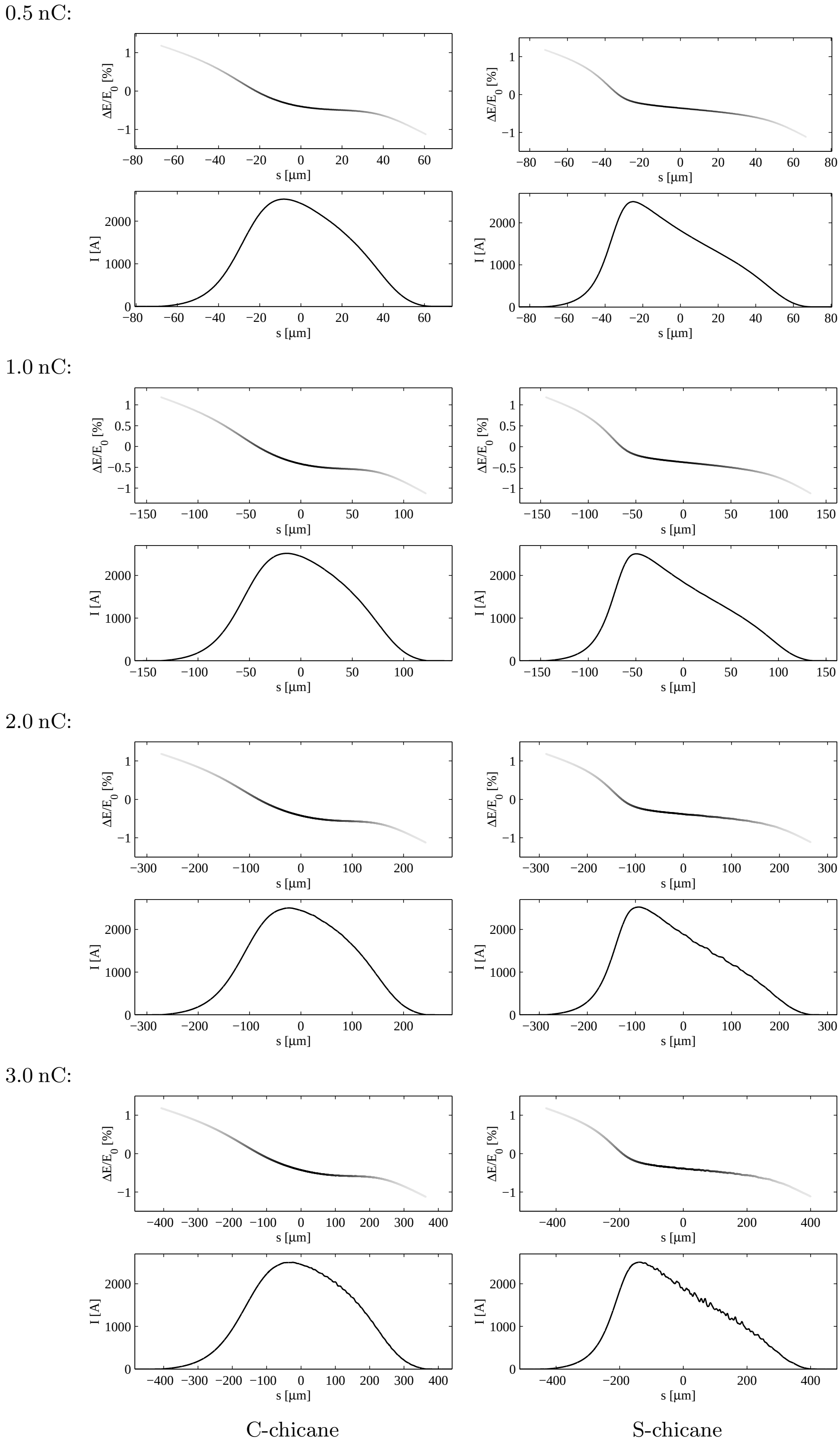

Figure 6.11: *The final longitudinal phase space distributions and the current profiles are given for bunch charges of $q_{\mathrm{tot}} = 0.5,\ 1.0,\ 2.0,\ 3.0$ nC. The left column shows the results behind a C-chicane and the right column shows the results behind an S-chicane. The initial total energy spread σ_{E} is the same for all simulations. In the phase space plots sub-bunches with a high charge are represented by darker dots than sub-bunches with lower charge. The noise in some of the the profiles is a numerical error of the simulations.*

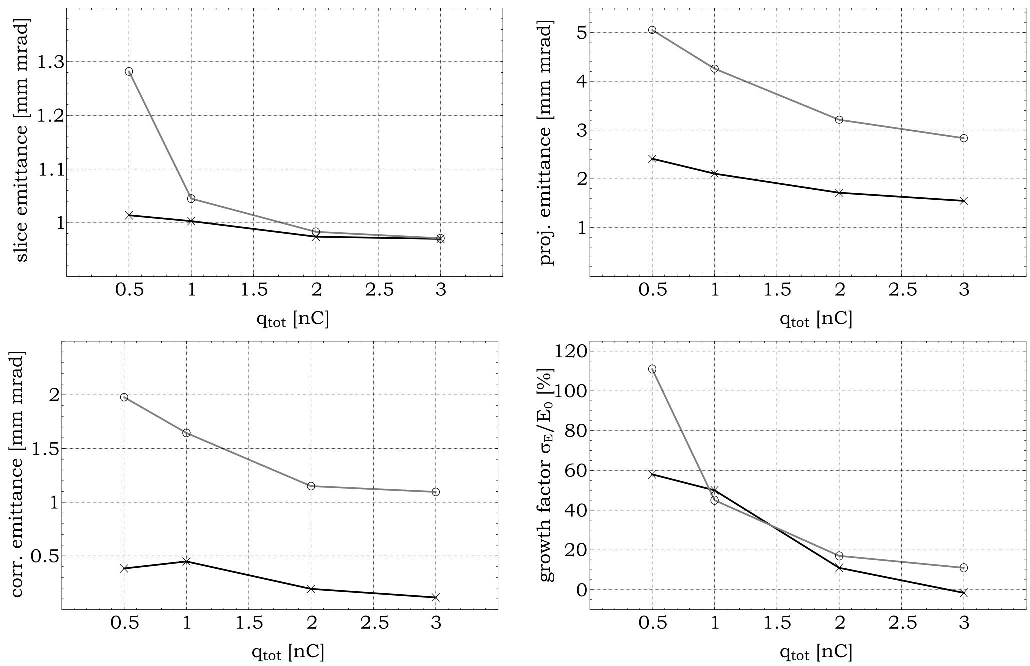

Figure 6.12: *The dependence of the normalized slice emittance (upper left), the normalized projected emittance (upper right), the normalized correlated emittance (lower left) and the growth factor of the slice energy spread (lower right) on the bunch charge is plotted. The energy slope is the same for all simulations. The results for a C-chicane are given in grey and the results for an S-chicane are given in black. Note that bunches with a lower charge are shorter.*

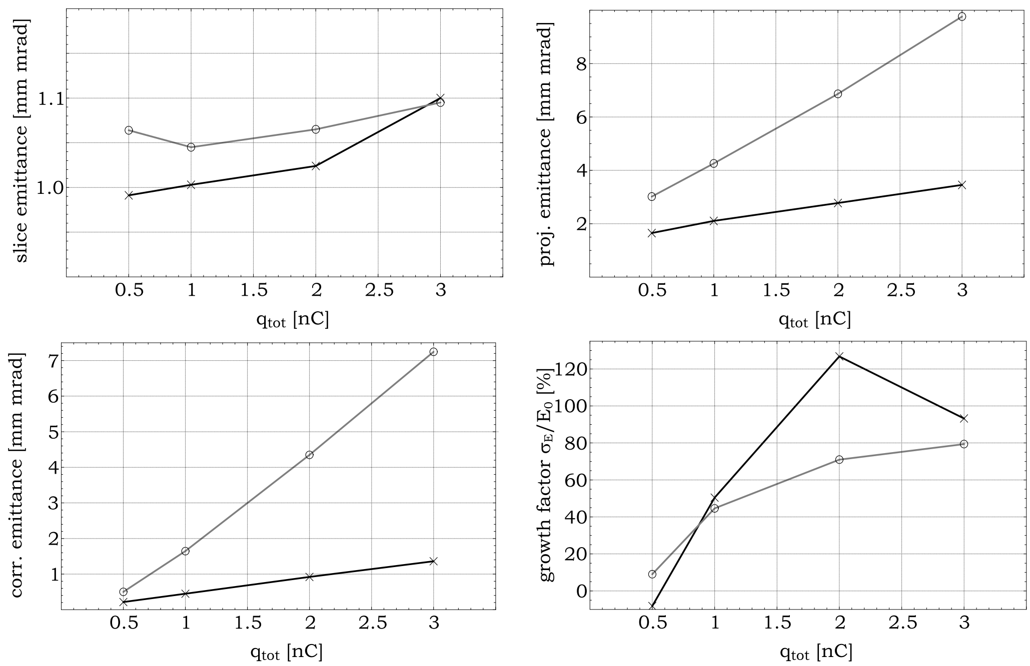

Figure 6.13: *The dependence of the normalized slice emittance (upper left), the normalized projected emittance (upper right), the normalized correlated emittance (lower left) and the growth factor of the slice energy spread (lower right) on the bunch charge is plotted. The total energy spread is the same for all simulations. The results for a C-chicane are given in grey and the results for an S-chicane are given in black. Note that the R_{56} increases with the charge.*

6.3 Layout of the Bunch Compressor Chicane

We have seen that a symmetric 6-bend S-chicane is a good choice for BC3. In this section I will give an overview of the final layout of BC3. Some technical aspects are discussed connected with the chosen layout and with the use of magnets of the same design as the BC2 dipoles. The mechanical and magnetic properties of these magnets are verified, to ensure that they fit the requirements of BC3. Firstly, the iron yoke has to be wide enough for the broad vacuum chamber that is needed in the dispersive sections to cover the large R_{56} range. Additional space is required for a straight beam pipe if the dipoles are switched off. Secondly, the field errors have to be small enough to ensure tolerable emittance growth. An estimation of the needed field quality and a comparison of these results with field measurements made at the BC2 dipoles is given.

At BC3 the length of the outer drifts of the chicane is 2.38 m and the central drift has a length of 5.259 m which agrees within the alignment tolerances of $\pm 0.2 - 0.3$ mm with the exact value of 5.2594m obtained from equation (3.25). The second and third dipole as well as the fourth and fifth dipole are separated by 0.5 m. The nominal bending angle of the dipoles is $\alpha = 3.85°$. Then the first order momentum compaction factor is $R_{56} = -5$ cm. The total length of the chicane is 14.019 m. The positions of the dipoles and the lengths of the drift spaces are given in figure 6.14.

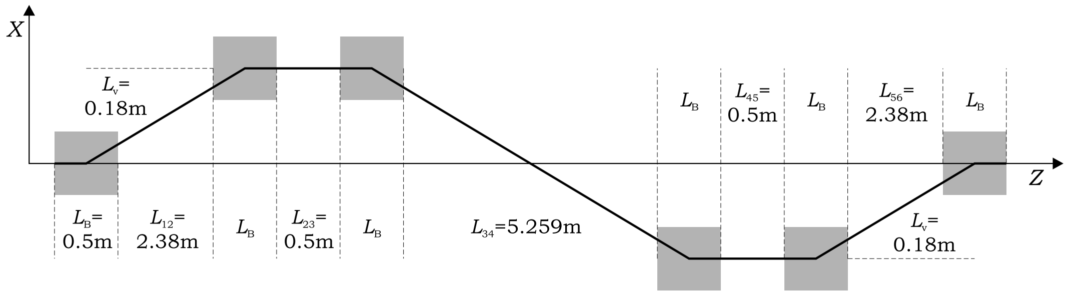

Figure 6.14: *Layout of the bunch compressor chicane.*

The total gap width of the dipoles is 221 mm and the usable width inside the chamber in dipoles $2-5$ is 208mm. The mid-point of these four dipoles is transversely displaced by 180mm with respect to the Z-axis. The chicane can be operated with an R_{56} ranging from -1.5 cm to -10 cm. These values correspond to a minimum bending angle of $\alpha = 2.1°$ and a maximum of $\alpha = 5.4°$. Figure 6.15 shows the cross section of one of the central dipoles. The horizontal beam positions for different R_{56} values are given. Dispersion variation inside the dipole is taken into account and a small safety margin is added. For nominal settings ($R_{56} = -5$ cm) the beam will not pass the central magnets exactly in the middle.

Plots of the maximum dispersion, the maximum offset, the final dispersion, the final offset, the path length with respect to the straight pass and the first order momentum compaction factor versus the bending angle are shown in figure 6.16. The graphs are calculated with the equations derived in chapter 3.3. The final transverse bunch offset is always small enough to be neglected. The final dispersion might not be negligible when the bending angle becomes large. The path length travelled by the bunch increases by some 10mm in comparison to the projected length of the chicane. This results in a change of the arrival time at the accelerating cavities downstream of the chicane and has to be taken into account in their phase settings. For further information on beam dynamics in both TTF2 bunch compressors refer to [17].

For mechanical reasons BC3 will have a vacuum chamber which is built of copper plated stainless steel. It combines the low surface resistivity of copper with the high mechanical stability of stainless steel. Since the total height of the dipole gap is 25 mm and the walls of the chamber have to be 5 mm thick for stability reasons, the maximum usable height is 15 mm. To get a stronger suppression of the CSR fields due to the shielding effect, the inner height of the chamber is only 8 mm (see chapters 4.4 and 6.2). As was already pointed out in chapter 4.5 the influence of wake fields in such a narrow chamber was only estimated. A thorough analysis was not performed. Additionally, the production process of the chambers only allowed to put a copper coating on the central part of the upper and lower surfaces. The short vertical walls of the chamber as well as the outermost parts of the upper and lower surfaces are not copper coated. Thus, an increase of the resistive wall wake fields can be expected when the beam passes the chamber close to these regions.

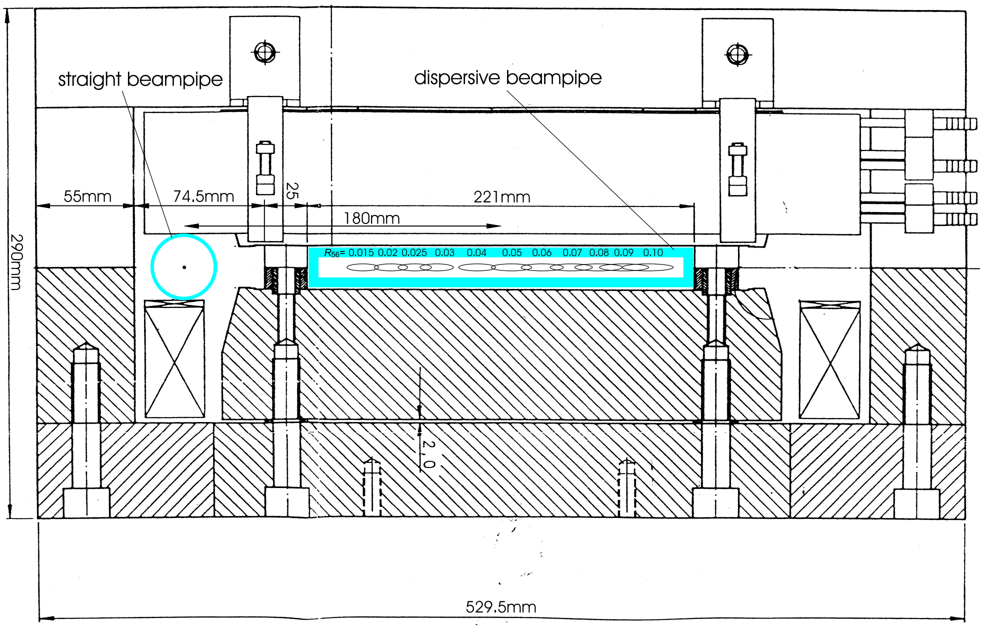

Figure 6.15: *A cross-section of a central dipole is shown. There is enough space between the coils of the dipole for a beam pipe passing straight on. The vacuum chamber between the poles is wide enough to use the bunch compressor with an R_{56} ranging from -1.5 cm to -10 cm. Both beam pipes are sketched in light grey. The ellipses inside the rectangular vacuum chamber show projections of the horizontal beam positions for different R_{56} and take into account the change in dispersion throughout the dipole. The height of the ellipses is arbitrarily chosen to make them visible.*

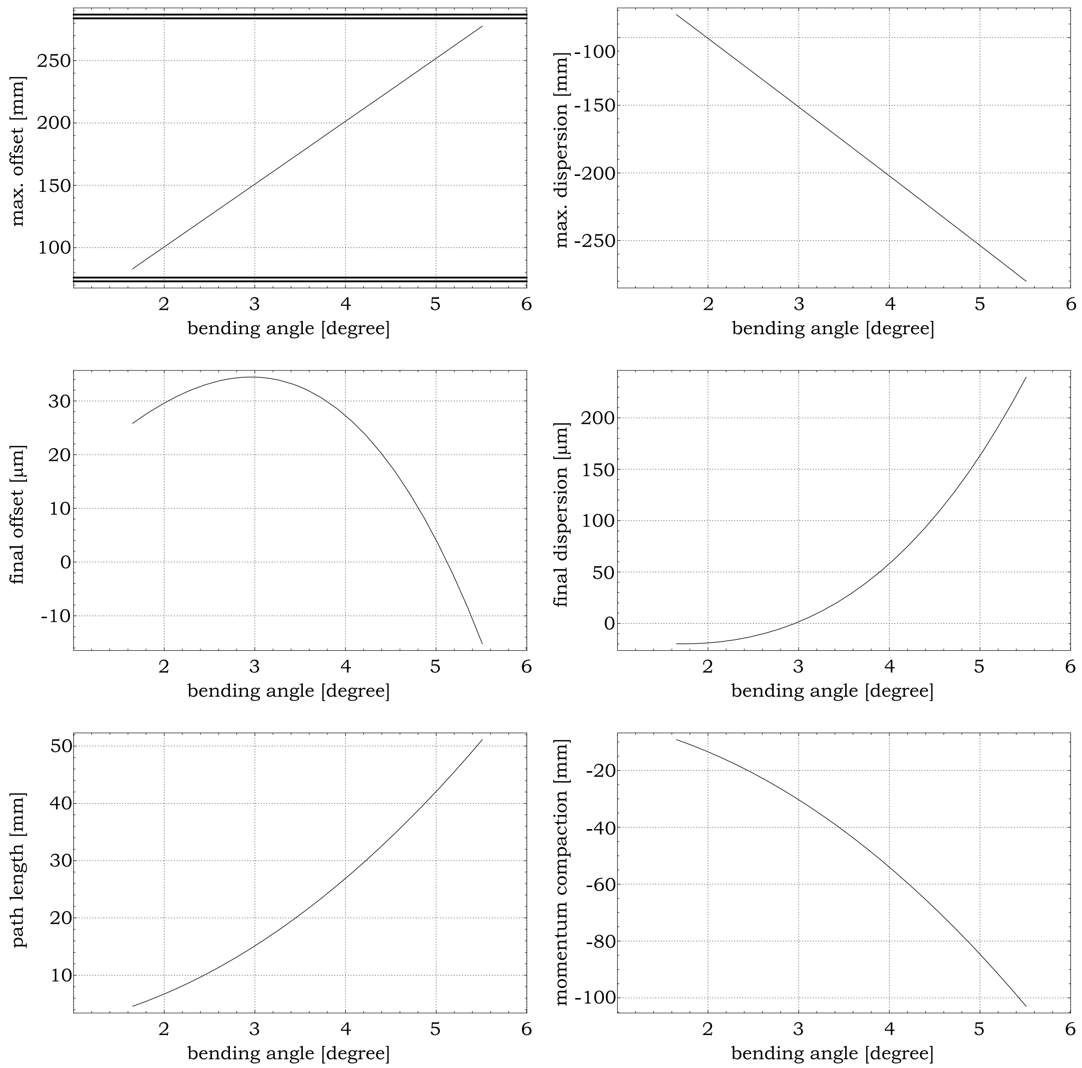

Figure 6.16: *The dependence on the bending angle is given for the maximum transverse bunch offset (upper left), the maximum dispersion (upper right), the final offset (middle left), the final dispersion (middle right), the path length which is travelled by the bunch with respect to the chicane length (lower left) and the first order momentum compaction factor (lower right).*

6.3.1 Estimation of Field Quality and Alignment Tolerances needed for the Dipoles

Besides the mechanical constraints, the field specifications of the dipoles have also to match the needs of BC3. When running BC3 with $R_{56} = -10$ cm a bending angle of $\alpha = 5.4°$ is needed. Since the maximum possible beam energy is about $E_0 = 500$ MeV and the magnets have a length of $L_\mathrm{B} = 0.5$ m, the dipoles should be able to produce a magnetic field of $B = \frac{E_0}{c\,e_0}\frac{\alpha}{L_\mathrm{B}} = 0.32$ T. The dipoles are designed for a maximum field of $B_\mathrm{max} = 0.375$ T.

The magnetic properties of the dipoles which were built for BC2 were measured at DESY [88]. The maximum field of these dipoles is about $B_\mathrm{max} = 0.41$ T with an error of $\Delta B \approx 0.05$ mT over almost the whole width of the yoke (figure 6.17). The relative field error is then $\frac{\Delta B}{B} = 1.2 \cdot 10^{-4}$. The field accuracy needed for BC3 is estimated from analytical formulae [89, 90] and by particle tracking simulations in the following section.

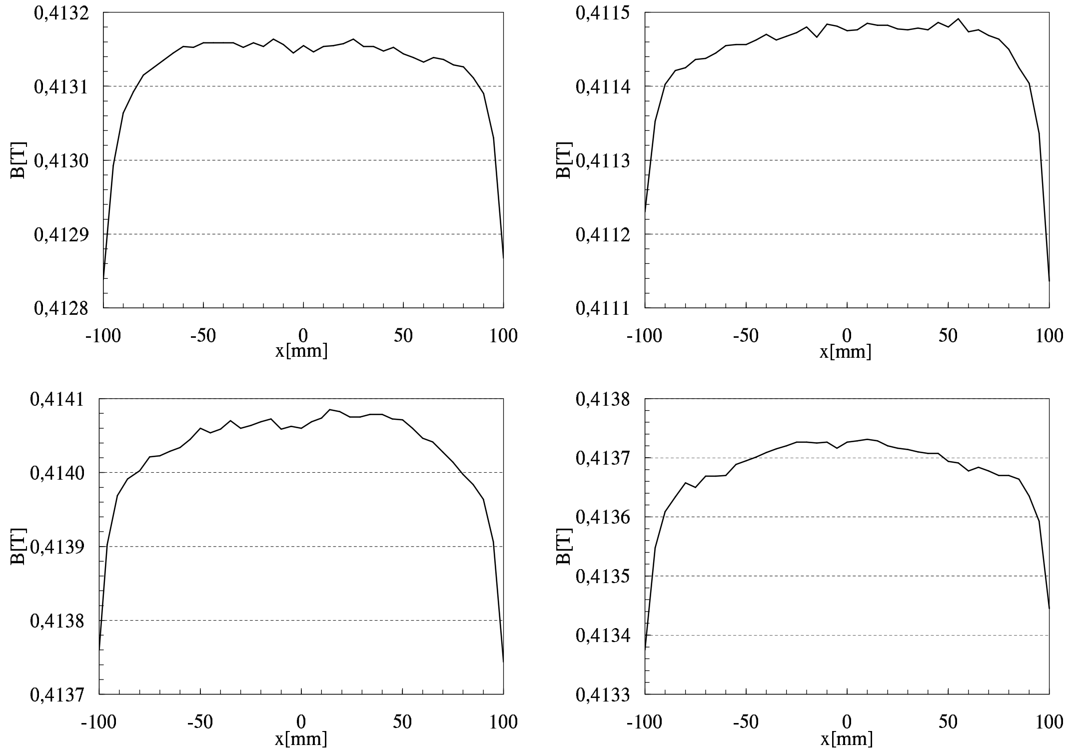

Figure 6.17: *The transverse field profiles of the four dipoles which were built for BC2 are shown for the case that they produce their maximum magnetic field. During standard operation of the bunch compressor the beam will pass the dipoles close to the mid-axis at* $x = 0$ mm. *Here the field varies less than* $\Delta B = 0.05$ mT.

Also the magnet alignment has to stay within certain limits (see also [91] and [89]). Assuming typical alignment tolerances of $\pm 0.2 - 0.3$ mm [92] errors of the transverse position of the dipoles are uncritical. A longitudinal misalignment will add only a small amount to the residual dispersion of the chicane and to the final transverse bunch offset. Also a small rotational error around the vertical or horizontal dipole axis is of no importance. But if a dipole has a roll error, i.e. a rotation around the Z-axis, a coupling of the magnetic fields into the vertical plane might dilute the vertical emittance. The upper limit for the roll angle of a single dipole of bending angle α at a position with a beta function β_y can be estimated as [89]

$$\Delta\phi < \frac{E_0}{\sigma_{\mathrm{E}}|\alpha|}\sqrt{\frac{2\Delta\varepsilon_{\mathrm{y}}}{\gamma\beta_{\mathrm{y}}}} \tag{6.1}$$

Then the growth of the normalized vertical emittance will be less than $\Delta\varepsilon_{\mathrm{y}}$. The initial vertical beta function at the first dipole is $\beta_{\mathrm{y}} \approx 50$ m. Assuming a bending angle of $\alpha = 5.4°$ and a relative rms energy spread of $\frac{\sigma_{\mathrm{E}}}{E_0} = 0.002$ the roll angle of the first dipole should not exceed $\Delta\phi = 0.2°$ to keep the emittance growth below $\Delta\varepsilon_{\mathrm{y}} = 0.01$ mm mrad. Since the beta function at the other magnets is lower, their roll angle is allowed to be larger.

6.3.1.1 Field Errors in Dipole Magnets

Inside a horizontally deflecting dipole magnet the magnetic field B_{y} consists of a strong dipole term B_{dip} and weak higher order terms B_n which can be expressed by an expansion of the field in the horizontal mid plane ($y = 0$):

$$B_{\mathrm{y}}(x, y=0) = B_{\mathrm{y}}(0) + \frac{x}{1!}\left.\frac{\partial B_{\mathrm{y}}}{\partial x}\right|_{x=0} + \frac{x^2}{2!}\left.\frac{\partial^2 B_{\mathrm{y}}}{\partial x^2}\right|_{x=0} + \ldots \tag{6.2}$$

Within a circle of radius r_0, which is usually chosen to be half the gap height, the magnetic field can be expressed as a sum of multipole components $B_{\mathrm{dip}}\, b_{n+1} = \left.\frac{\partial^n B_{\mathrm{y}}}{\partial x^n}\right|_{x=0}\frac{r_0^n}{n!}$:

$$B_{\mathrm{y}}(x, y=0) = B_{\mathrm{dip}}\left(b_1 + b_2\frac{x}{r_0} + b_3\frac{x^2}{r_0^2} + \ldots\right) \tag{6.3}$$

The coefficients b_n are called multipole coefficients. b_2 is the quadrupole coefficient and b_3 is the sextupole coefficient. The normalized multipole strength K_n is given by $K_n = \frac{c\,e_0}{E}\left.\frac{\partial^n B_{\mathrm{y}}}{\partial x^n}\right|_{x=0} = \frac{1}{B_{\mathrm{dip}}R}\left.\frac{\partial^n B_{\mathrm{y}}}{\partial x^n}\right|_{x=0}$. R is the bending radius of the magnet. With these definitions the multipole components can be expressed as:

$$b_2 = RK_2r_0,\ b_3 = \frac{1}{2!}RK_3r_0^2,\ \ldots \tag{6.4}$$

Each multipole component of the magnetic field inside a dipole adds to the emittance. The emittance growth is either due to an enlargement, e.g. caused by a dispersion mismatch, or due to a nonlinear deformation of the horizontal phase space distribution. As long as the horizontal beam size $\sigma_{\mathrm{x}} = \sqrt{\frac{\varepsilon_{\mathrm{x}}\beta_{\mathrm{x}}}{\gamma} + R_{16}^2\left(\frac{\sigma_{\mathrm{E}}}{E_0}\right)^2}$ is dominated by the dispersive contribution, $\sigma_{\mathrm{x}} \approx R_{16}\,\frac{\sigma_{\mathrm{E}}}{E_0}$, uncorrelated error kicks $\Delta x'$ add statistically to the horizontal phase space coordinates:

$$\sigma_{\mathrm{x}'} \approx \sqrt{\frac{\varepsilon_{\mathrm{x}}}{\gamma\,\beta_{\mathrm{x}}} + \sigma_{\Delta\mathrm{x}'}^2} \tag{6.5}$$

The growth $\Delta\varepsilon_{\mathrm{x}}$ of the normalized horizontal emittance ε_{x} is[2]:

$$\Delta\varepsilon_{\mathrm{x}} \approx \gamma\beta_{\mathrm{x}}\sigma_{\Delta\mathrm{x}'}^2 \tag{6.6}$$

[2]If the horizontal beam size is dominated by the horizontal beam optics, $\sigma_{\mathrm{x}} \approx \sqrt{\frac{\varepsilon_{\mathrm{x}}\,\beta_{\mathrm{x}}}{\gamma}}$, the emittance growth is $\frac{\Delta\varepsilon_{\mathrm{x}}}{\varepsilon_{\mathrm{x}}} \approx 2\frac{\sigma_{\Delta\mathrm{x}'}}{\sigma_{\mathrm{x}'}}$. A quadrupole component can only dilute the emittance due to a dispersion mismatch.

It depends on the beta function β_x at the location of the dipole and the relativistic factor γ. $\sigma^2_{\Delta x'}$ is a small additional divergence induced by the multipole component. In the four central dipoles of BC3 the horizontal beam size is dominated by the dispersion and the emittance growth is given by (6.6). Since the horizontal beam size is very small in the outer dipoles their contribution to the emittance can be neglected. In case of the quadrupole component the divergence error is given by a dispersion kick $\Delta R_{26} = K_2 L_B R_{16}$:

$$\sigma_{\Delta x',\mathrm{quad}} = \Delta R_{26}\frac{\sigma_E}{E_0} = K_2 L_B R_{16}\frac{\sigma_E}{E_0} \tag{6.7}$$

L_B is the length of the dipole, R_{16} is the dispersion at the location of the dipole. The divergence error due to a sextupole error is:

$$\sigma_{\Delta x',\mathrm{sext}} = \frac{1}{2}K_3 L_B R_{16}^2 \left(\frac{\sigma_E}{E_0}\right)^2 \tag{6.8}$$

Substituting (6.7) in (6.6) results in the growth of the normalized horizontal emittance induced by a quadrupole component:

$$\Delta\varepsilon_{x,\mathrm{quad}} \approx \gamma\,\beta_x\,K_2^2\,L_B^2\,R_{16}^2\,\left(\frac{\sigma_E}{E_0}\right)^2 \tag{6.9}$$

The emittance growth induced by a sextupole component is

$$\Delta\varepsilon_{x,\mathrm{sext}} \approx \frac{1}{4}\gamma\,\beta_x\,K_3^2\,L_B^2\,R_{16}^4\,\left(\frac{\sigma_E}{E_0}\right)^4 \tag{6.10}$$

For the quadrupole and sextupole coefficients it can now be estimated that their values should not exceed

$$b_2 \approx \frac{r_0}{\alpha\frac{\sigma_E}{E_0}}\sqrt{\frac{\Delta\varepsilon_x}{\gamma}\frac{1}{\beta_x\,R_{16}^2}} \tag{6.11}$$

and

$$b_3 \approx \frac{r_0^2}{\alpha\left(\frac{\sigma_E}{E_0}\right)^2}\sqrt{\frac{\Delta\varepsilon_x}{\gamma}\frac{1}{\beta_x\,R_{16}^4}} \tag{6.12}$$

in a dipole of bending angle α. The contribution of each multipole component to the normalized emittance is $\Delta\varepsilon_x$. In a row of m identical dipoles the total emittance growth is the sum of the contributions in each dipole. Only dipoles at positions with high dispersion R_{16} and high beta function β_x contribute to the emittance growth.

I specify that the quadrupole component and the sextupole component in the dipoles of BC3 should each add $\Delta\varepsilon_x \leq 0.05$ mm mrad to the normalized emittance. To estimate the maximum allowed multipole coefficients b_2 and b_3 for the BC3 dipoles we only have to consider the four inner dipoles. The outer two are at positions with vanishing dispersion. The values of the beta function at the locations of the four dipoles are $\beta_1 \approx 45$m, $\beta_2 \approx 40$m, $\beta_3 \approx 7$ m and $\beta_4 \approx 7$ m. For symmetry reasons the absolute value of the dispersion is always $R_{16} \approx 0.275$ m. The bending angle is $\alpha = 5.4°$. The beam has an energy of $E_0 = 500$ MeV or $\gamma \approx 1000$ and a relative energy spread of $\frac{\sigma_E}{E_0} = 0.002$.

Using these values we get a maximum allowed quadrupole coefficient of $b_2 = 1.7 \cdot 10^{-4}$ within a radius of $r_0 = \pm 12.5$ mm. An analysis of tracking data which I obtained with the code MAD [93] for a gaussian particle distribution using the same parameters as above results in an allowed quadrupole coefficient of $b_2 = 1.8 \cdot 10^{-4}$. For the sextupole coefficient the formula results in $b_3 = 3.9 \cdot 10^{-3}$ and the simulations result in $b_3 = 3.1 \cdot 10^{-3}$. One can see that the acceptable values for the field errors in the dipoles are larger than the field errors measured in the dipoles of BC2.

6.3.2 Influence of Jitter on Beam Dynamics in BC3

In addition to the static errors jitter can also have an influence on the beam dynamics. In a bunch compressor chicane two sources of jitter can be identified. One is the power supply ripple which influences the bending angle of the magnets and the second is the jitter of the accelerating phase and amplitude in the upstream accelerating modules which change the bunch energy and the energy slope $\frac{dE}{ds}$ along the bunch.

All dipoles are connected to a single power supply. The current of this power supply is stable within $\frac{\Delta I}{I_0} \leq 10^{-4}$ [94]. When the current changes by such a small amount the small hysteresis of the dipoles is not negligible and the magnetic field will jitter less than the current [88]. To first order, the bending angle depends linearly on the magnetic field. Thus, the power supply ripple produces a jitter of the bending angle by $\frac{\Delta\alpha}{\alpha} < 10^{-4}$. For a nominal bending angle of $\alpha = 3.85°$ the path length jitter which is induced is less than $4\,\mu$m and influences the timing by less than 10 fs. The effect on beam dynamics due to the change in the compression factor and the CSR fields is insignificant.

A change ΔE in the bunch energy E_0 due to jitter in the RF amplitude and the RF phase has an impact on the mean bending angle α by which the electron are deflected. Accordingly, a jitter in the energy has a similar influence as the power supply ripple. The bending angle is proportional to $\frac{1}{E_0}$. Thus, an energy jitter will transform into an angle jitter $\frac{\Delta\alpha}{\alpha} = \frac{\Delta E}{E_0}$. Since the R_{56} as well as the path length depend quadratically on the bending angle they will jitter by twice the amount. For a single accelerating module the jitter of the RF amplitude is expected to be $\frac{\Delta V_{\mathrm{acc}}}{V_{\mathrm{acc}}} = 10^{-3}$ [95] and the phase jitter is about $\Delta\phi = 0.1°$ [96]. The beam is accelerated in ACC2 and ACC3 from an energy of 130 MeV to 450 MeV. The influence of the phase jitter on the energy is found to be small. Thus, the relative energy jitter in front of BC3 is the same as the relative jitter of the RF amplitude: $\frac{\Delta E}{E_0} = 10^{-3}$. The impact of such an energy jitter on the bunch compression and the CSR fields in the chicane is small. But the path length will jitter by about $40\,\mu$m and the timing will jitter by about 130 fs assuming a bending angle of $\alpha = 3.85°$.

An additional effect of the phase jitter σ_ϕ is that it changes the total energy spread of the bunch and consequently the final bunch length [97]. The energy slope $u = \frac{dE}{ds}$ along the bunch behind an accelerating module is approximately the same for all electrons within the bunch. It depends on the RF phase ϕ and a phase error $\Delta\phi$.

$$u(\Delta\phi) = (E_{\mathrm{f}} - E_{\mathrm{i}})\,\frac{2\pi}{\lambda_{\mathrm{RF}}}\frac{\sin(\phi + \Delta\phi)}{\cos\phi} \tag{6.13}$$

In the accelerating module the bunch is accelerated from an energy of E_{i} to an energy of E_{f}. The wavelength of the RF field is λ_{RF}. The bunch has a length of $\sigma_{\mathrm{s,i}}$ in front of the bunch compressor chicane and is compressed to a final length of

$$\sigma_{\mathrm{s,f}} = \sigma_{\mathrm{s,i}} - R_{56}\sigma_{\mathrm{s,i}}\left(1 - \frac{E_{\mathrm{i}}}{E_{\mathrm{f}}}\right)\frac{2\pi}{\lambda_{\mathrm{RF}}}\frac{\sin(\phi + \Delta\phi)}{\cos\phi} \tag{6.14}$$

A phase jitter σ_ϕ will lead to an error in the final bunch length of

$$\Delta\sigma_{\mathrm{s,f}} = \left|\frac{d\sigma_{\mathrm{s,f}}}{d\Delta\phi}\right|\sigma_\phi \tag{6.15}$$

$$\approx \left|(\sigma_{\mathrm{s,f}} - \sigma_{\mathrm{s,i}})\cot\phi\right|\sigma_\phi \tag{6.16}$$

Assuming typical BC3 parameters of $\sigma_{\mathrm{s,i}} = 250\ \mu$m, $\sigma_{\mathrm{s,f}} = 50\ \mu$m, a nominal phase in ACC2 and ACC3 of $\phi = 15°$ and a phase jitter of $\sigma_\phi = 0.1°$ this results in a jitter of the final bunch length of $1.3\ \mu$m or 2.6%.

If the bunch has a gaussian profile the peak current will jitter also by 2.6%. Since the strength of the CSR fields depends on the bunch shape also a jitter in the transverse emittance, beam position and direction is induced. If the bunch is not gaussian but contains charge concentrations the jitter of the peak current and the CSR fields will be stronger [98].

6.3.3 Overview of the Bunch Compressor Section

BC3 is located between the accelerating modules ACC3 and ACC4. The available space is 21.9 m. The chicane itself has a length of 14 m and the remaining space contains various diagnostic systems and quadrupoles for optics matching. Horizontal and vertical steering magnets are included to correct the beam orbit. The diagnostic section in front of the chicane has a length of 3.1 m and the diagnostic section behind the chicane has a length of 4.8m.

The transverse beam position and beam profile can be measured at various positions along BC3. The transverse emittance, the bunch length and the bunch current can be measured in front of the chicane and behind it.

Two quadrupoles are installed in front of the chicane to match the optics of the incoming beam. The transverse beam position can be measured with two beam position monitors (BPM) of the strip-line type. The beam trajectory may be adjusted with a horizontal and a vertical steering magnet. At the end of ACC3 there is an additional BPM, a pair of steerers and a pair of quadrupoles. They can also be used for optics matching and for trajectory corrections.

To measure the incoming beam profile a screen which emits optical transition radiation (OTR) is located in front of the first dipole of the chicane. In combination with the quadrupoles it can be used for a determination of the emittance. To measure the transmission of the chicane, current monitors (so called toroids) are built in at the beginning and at the end of the BC3 section.

For beam profile measurements inside the chicane, one OTR screen is located at the zero crossing of the transverse beam offset. Here also the dispersion vanishes. Another OTR screen is located between the fourth and the fifth dipole, i.e. at a position with maximum dispersion. Special arrays of pick-up BPMs are located behind the second and the fourth dipole. These enable measurements of the beam position over almost the whole width $\Delta X = \pm 100$ mm of the chamber. The drift space between the second and third dipole can be used later for additional diagnostics or collimation. Since the BPMs and one of the OTRs are located in dispersive sections they can be used for energy and energy spread measurements.

The synchrotron radiation which is emitted in the dipoles can be used for diagnostic purposes at three synchrotron radiation ports. Their positions are chosen for a nominal operation of BC3 with a bending angle of 3.85°. Two are located inside the chicane behind the third and the fifth dipole. The first port points at a position 24 cm behind the start of the second dipole. The second port points at a position 24cm behind the start of the fourth dipole. The positions of the source points correspond to a deflection of 1.85°. The distance between the source points of the radiation and the windows is about 2.2 m. Since the two ports have a width of 24 mm and a height of 8 mm only a narrow radiation cone is visible. This limits their usability but due to mechanical constraints no better solution was found. The third synchrotron radiation port is located a short distance behind the last dipole. It points at a position 8.4 cm behind the start of this dipole. This corresponds to a deflection of 0.65°. The distance between the window and the source point is 1.3m. The port is 8mm high and 26 mm wide. As was shown in chapter 4.2 the coherent synchrotron radiation is not in steady state inside the dipoles of BC3. Accordingly, if the synchrotron radiation ports are used for diagnostic purposes the total radiation power and the spectrum have to be carefully calculated. Also the effect of shielding due to the vacuum chamber should be included.

In the diagnostics section behind the chicane two strip-line BPMs and two pairs of steerers can be used for trajectory corrections. A quadrupole triplet is available for optics matching and emittance measurements. For the emittance measurements an OTR screen is included. Additionally, the beam profile can be measured by a wire scanner. A diffraction radiation screen can be used for bunch length measurements. A wall current monitor and a phase monitor are also present. In figure 6.18 the whole BC3 section is sketched.

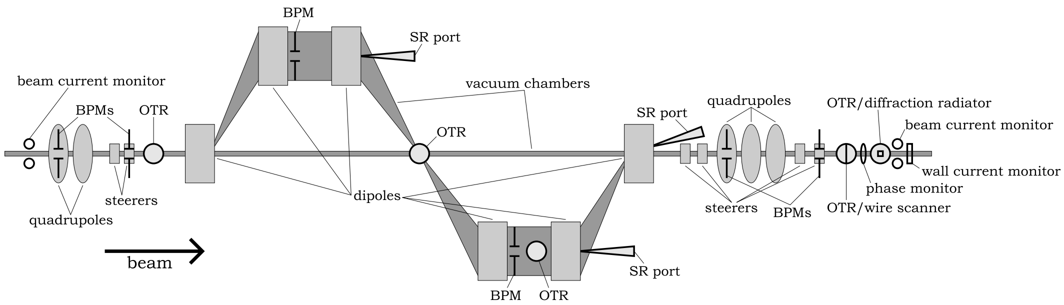

Figure 6.18: *The sketch shows the magnets and the diagnostic components that are included in the BC3 section.*

Chapter 7

CSR Microbunch Instability

As was pointed out in [99], [100] and [101], coherent synchrotron radiation can lead to an amplification of density and energy fluctuations in an electron bunch that passes a bunch compressor chicane. This leads to a growth of the transverse emittance and, eventually, to a fragmentation of the phase space distribution.

A theoretical analysis, as described in the next section, shows that the amplification of a sinusoidal modulation depends on its wavelength. Shorter modulations will be more strongerly amplified than longer modulations. The uncorrelated energy spread and the transverse emittance of the electron bunch will suppress the amplification. In section 7.2 the simulation results for a special C-chicane, the so called benchmark chicane, are compared to the theoretical predictions. Section 7.3 compares simulation results for a symmetric C-chicane and a symmetric 6-bend S-chicane. In the last section of this chapter the modulation amplification is studied for a beam line which consists of the two bunch compressor chicanes at TTF2.

7.1 Theoretical Description of the Modulation Amplification

The basic idea of the amplification mechanism is that a modulation in the longitudinal beam profile induces an energy modulation at the same frequency due to the CSR fields generated in the dipoles. The energy modulation is, in turn, converted back to a charge density modulation since the path lengths of the electrons differ due to the dispersive effects in the bunch compressor chicane. Behind the chicane the density modulation can exceed the initial one by a large amplification factor. This mechanism can start from either a density or an energy modulation.

Equations which describe the amplification of a sinusoidal modulation as a function of its wavelength are derived in [102] for a one-dimensional beam of infinite length passing a 3-bend chicane. The lengths of the drift spaces in the chicane are assumed to be much longer than the dipoles. If the separation of the two central dipoles of a 4-bend C-chicane is small the equations can also be applied to this case. The equations cannot be used to calculate the amplification in S-chicanes. The beam model includes neither transverse emittance nor an energy slope along the bunch. That means, the bunch is not compressed when it passes the chicane. The initial density modulation has to be small in comparison to the mean charge density.

For the derivation of the equations some additional simplifications are made. It is assumed that transient effects in the dipoles can be neglected and the CSR fields are in steady state. In [102] the condition

$$L_{\mathrm{B}} \gg \left(\frac{24R^2}{k}\right)^{1/3} \Leftrightarrow \lambda \ll 2\pi\frac{R\alpha^3}{24} \tag{7.1}$$

is given. L_{B} is the length of the outer two dipoles. The central dipole has twice the length. The bending radius of the dipoles is R. $k = \frac{2\pi}{\lambda}$ is the wave number of the modulation. In case of the BC3 dipole parameters ($L_{\mathrm{B}} = 0.5$ m, $R = 7.5$ m) the modulation wavelength λ must be much smaller than 580 μm. Also the effect of CSR shielding by the vacuum chamber as well as the transverse size of the bunch are not taken into account. Thus, the condition

$$\left(\frac{R}{h^3}\right)^{1/2} \ll \frac{2\pi}{\lambda} \ll \left(\frac{R}{\sigma_{\mathrm{x}}^3}\right)^{1/2}$$

has to be fulfilled [102]. The chamber height at BC3 is $h = 8\,\mathrm{mm}$ and the transverse beam size is roughly $\sigma_{\mathrm{x}} = 0.1$ mm. Hence, the applicability of the equations is limited to the range $1600\,\mu\mathrm{m} \gg \lambda \gg 2\,\mu\mathrm{m}$.

Along a 3-bend chicane the density modulation develops in five stages. In the first dipole the initial density modulation induces an energy modulation due to the CSR fields which are produced by the electrons. Consequently, the electrons will travel along paths with different lengths in the following drift space. In the second dipole the path length differences are converted into a density modulation. This new density modulation has the same wavelength as the initial modulation and adds to it. At the same time, the density modulation will again enlarge the energy modulation as in the first dipole. These processes are repeated in the second drift space and the third dipole.

When the density modulation and the energy modulation amplify each other inside a dipole we expect an exponential growth of both modulations. But since the energy modulation influences the density modulation only via dispersive effects the energy modulation can be assumed to be constant along the dipole for the calculation of development of the density modulation. Only if

$$L_{\mathrm{B}} \gg \left(\frac{\gamma_0 I_{\mathrm{A}}}{I_0}\right)^{1/4} \frac{\lambda^{1/3}}{(2\pi)^{1/3}} R^{2/3} \tag{7.2}$$

will an exponential growth take place inside a dipole [102]. I_0 is the peak current of the unmodulated current profile. $I_{\mathrm{A}} = \frac{4\pi m_{\mathrm{e}} c}{\mu_0 e_0} \approx 17045$ A is the Alfven current. γ_0 is the relativistic Lorentz factor. Using BC3 parameters the wavelength of the modulation must be less than $5\,\mu$m for an exponential growth of the modulation. We will see later that the amplification of these short modulations will be suppressed by the uncorrelated energy spread and the emittance. Thus, the regime of exponential growth is not reached and the modulation grows linearly along a dipole.

In [102] the amplification factor, which is also called gain, of a small density modulation on top of a bunch with no uncorrelated energy spread is found to be

$$G(\lambda) = \frac{2\Gamma^2\left(\frac{2}{3}\right)}{3^{5/3}} \left(\frac{I_0}{\gamma_0 I_{\mathrm{A}}}\right)^2 \frac{(2\pi)^{8/3} \left|R_{56}\right|^2 L_B^2}{\lambda^{8/3} R^{4/3}} \tag{7.3}$$

R_{56} is the first order momentum compaction factor of the chicane. One can see that for small wavelengths λ the gain diverges whereas for long wavelengths the gain vanishes.

When the electron bunch has an uncorrelated energy spread $\frac{\sigma_\gamma}{\gamma_0}$ the modulation amplitude is reduced in the dispersive parts of the chicane due to the nonuniform motion of the electrons. Especially, very short modulations will be strongly suppressed. The amplification factor is found to be [102]

$$G(\lambda) = \frac{2\Gamma^2\left(\frac{2}{3}\right)}{3^{5/3}} g_0^2\, f\left(\frac{2\pi\sigma_\gamma}{\gamma_0\lambda}\left|R_{56}\right|\right) \tag{7.4}$$

Here

$$g_0 = \frac{I_0}{\sigma_\gamma I_{\mathrm{A}}} \left(\frac{\gamma_0}{\sigma_\gamma}\right)^{1/3} \frac{L_{\mathrm{B}}}{\left(R^2 \left|R_{56}\right|\right)^{1/3}} \tag{7.5}$$

depends only on chicane and bunch parameters. The wavelength dependence is described by

$$f(\hat{k}) = 3\hat{k}^{2/3} e^{-\frac{\hat{k}^2}{2}} \left(1 + \frac{\sqrt{\pi}\hat{k}^2 - 2\sqrt{\pi}}{2\hat{k}} e^{\frac{\hat{k}^2}{4}} \mathrm{erf}(\hat{k}/2) \right) \tag{7.6}$$

It has a maximum at $\hat{k} \approx 2.15$. The exponential term $e^{-\frac{\hat{k}^2}{2}}$ suppresses the gain for high $\hat{k}$, i.e. for short wavelength modulations (figure 7.1).

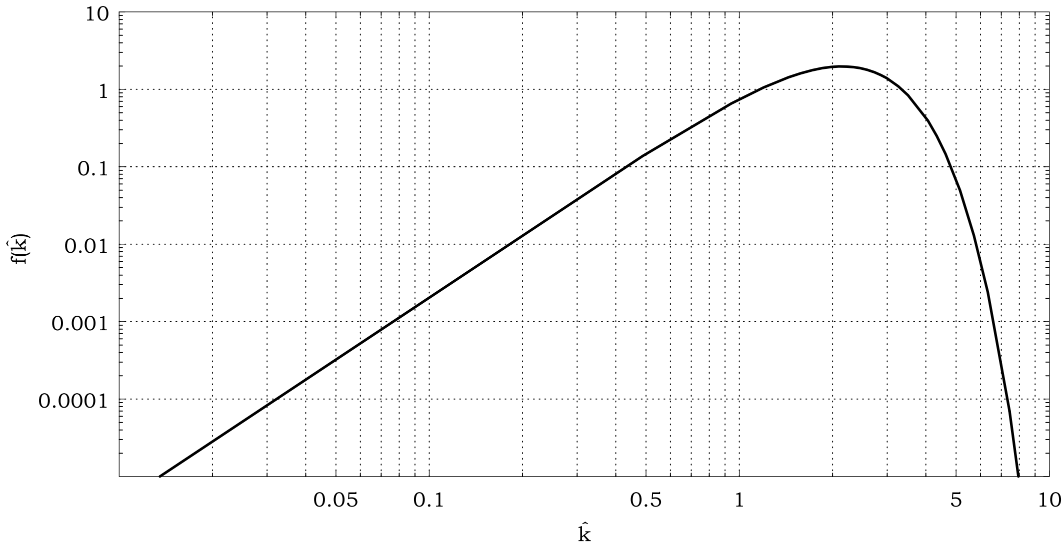

Figure 7.1: *The function $f(\hat{k})$ is plotted versus the normalized wave number $\hat{k}$. It describes the frequency dependence of the modulation amplification for a bunch which includes uncorrelated energy spread.*

Due to the assumptions made on the electron bunch and the chicane geometry equations (7.3) and (7.4) cannot be used if the influence of transverse emittance or compression of the bunch length on the amplification of modulations should be studied. The equations cannot be used at all to calculate the amplification of modulations in S-chicanes.

In [103] a theoretical approach is presented that is based on the solution of a linearized Vlasov equation. An integral equation is derived that describes the development of a modulation in the longitudinal charge density of an electron bunch along a bunch compressor chicane. The bunch can have a linear energy slope, uncorrelated energy spread and emittance. No assumptions are made on the layout of the chicane. Thus, the integral equation can be applied to S-chicanes. In [104] a simplification of the integral equation is given that is only applicable to C-chicanes.

Some simplifications which I discussed before are also applicable within this model. Transient effects in short magnets are neglected, i.e. the CSR fields are in steady state. The shielding effect of the vacuum chamber is not included. The wavelength of the modulation is shorter than the bunch length. The transverse charge distribution and the energy distribution are both gaussian. The longitudinal charge distribution is uniform with a small sinusoidal modulation.

Along the chicane the amplification factor of a small initial density modulation of amplitude $A_k^{(0)}$ is defined as [103]

$$G_k(z) = \frac{|A_k(z,s)|}{c_\mathrm{f}(z) A_k^{(0)}} \tag{7.7}$$

z is the longitudinal bunch position along the chicane and s is the electron position inside the bunch. The wave number of the modulation is k. $c_{\mathrm{f}}(z) = \frac{1}{1-u_{\mathrm{r}}R_{56}(z)}$ is the compression factor which depends on the relative energy slope $u = \frac{1}{E_0}\frac{dE}{ds}$ and the momentum compaction factor R_{56}. The development of the modulation amplitude is given by

$$A_k(z,s) = c_{\mathrm{f}}(z) g_k(z) e^{ikc_{\mathrm{f}}(z)s} \tag{7.8}$$

The factor $g_k(z)$ for a given wave number k is obtained from a numerical integration of

$$g_k(z) = g_k^{(0)}(z) + \int_0^z K(z,z')g_k(z')dz' \tag{7.9}$$

The function

$$g_k^{(0)} = A_k^{(0)} e^{-\frac{c_{\mathrm{f}}(z)^2k^2\varepsilon_{\mathrm{x}}}{2\beta_0}(\beta_0^2R_{51}^2(z)+R_{52}^2(z))-\frac{1}{2}c_{\mathrm{f}}(z)^2k^2\frac{\sigma_\gamma^2}{\gamma_0^2}R_{56}^2(z)} \tag{7.10}$$

depends on the matrix elements $R_{51}(z)$, $R_{52}(z)$, $R_{56}(z)$ which relate the longitudinal electron position inside the bunch to its initial transverse coordinates x, x' and its reletive energy deviation $\frac{\delta_{\mathrm{E}}}{E_0}$. The beta function at the entrance of the chicane is β_0. The initial uncorrelated energy spread is σ_γ and the initial transverse emittance is ε_{x}. The kernel

$$\begin{aligned} K(z,z') = {} & \frac{ikI_0}{I_{\mathrm{A}}\gamma}\frac{c^2\epsilon_0}{R(z)^2}\, Z(kc_{\mathrm{f}}(z'),z')\, c_{\mathrm{f}}(z')\, c_{\mathrm{f}}(z)\, R_{56}(z'\to z) \\ & e^{-\frac{k^2\varepsilon_{\mathrm{x}}}{2\beta_0}\left(\beta_0^2R_{51}^2(z,z')+R_{52}^2(z,z')\right)-\frac{k^2\sigma_\gamma^2}{2\gamma_0^2}R_{56}^2(z,z')} \end{aligned} \tag{7.11}$$

depends on the initial beam current I_0 and the matrix elements $R_{51}(z,z') = c_{\mathrm{f}}(z)\, R_{51}(z) - c_{\mathrm{f}}(z')\, R_{51}(z')$, $R_{52}(z,z') = c_{\mathrm{f}}(z)\, R_{52}(z) - c_{\mathrm{f}}(z')\, R_{52}(z')$ and $R_{56}(z,z') = c_{\mathrm{f}}(z)\, R_{56}(z) - c_{\mathrm{f}}(z')\, R_{56}(z')$. The factor

$$R_{56}(z'\to z) = -\int_{z'}^{z}\frac{R_{16}(z',z^*)}{R(z^*)}dz^* \tag{7.12}$$

is an element of the first order transfer matrix between the points z' and z along the chicane. It is given by the dispersion $R_{16}(z)$ and the bending radius $R(z)$. The synchrotron radiation impedance $Z(k,z) = -i\frac{R(z)^2}{c^2\epsilon_0}\frac{k^{1/3}3^{-1/3}\Gamma(\frac{2}{3})(\sqrt{3}i-1)}{4\pi\epsilon_0 R(z)^{2/3}}$ relates the spectral synchrotron radiation power generated by a single circulating electron $P_k = \mathrm{Re}(Z(k,z))\, \bar{I}_{\mathrm{e}}^2$ to the mean current $\bar{I}_{\mathrm{e}} = \frac{e_0c}{2\pi R}$ of a single electron.

In the following sections simulation results are compared to gain curves, i.e. the modulation amplification factor versus the wavelength. The gain curves are numerically calculated by a Mathematica code written by G. Stupakov [105, 106] The optical functions are obtained from tracking a beam with the tracking code Elegant [68] through the chicane.

7.2 CSR Instability in the Benchmark Chicane

During a workshop on coherent synchrotron radiation in January 2002 [71] it was decided to make a comparison of various CSR simulation codes for a special benchmark chicane. I made simulations with the code TraFiC[4]. First results were presented at the High Brightness Electron Beams Workshop later that year [73]. The benchmark chicane is a C-chicane. Its basic parameters and the parameters of the charge distributions are given in table 7.1. The distributions are line-distributions.

dipole length	L_{B}	0.5 m	beam energy	E_0	5.0 GeV
1st and 3rd drift	L_{12}/L_{34}	5.0 m	flat top current	I_0	6000 A
2nd drift	L_{23}	1.0 m	norm. emittance	$\varepsilon_{\mathrm{x,y}}$	$0\ /\ 1 \cdot 10^{-6}$ m rad
bending radius	R	10.35 m	unc. energy spread	σ_ϵ	$0\ /\ 3 \cdot 10^{-5}$
bending angle	α	2.77 deg			
momentum comp.	R_{56}	-2.5 cm			

Table 7.1: *Parameters of the benchmark chicane and the electron bunch.*

The longitudinal current profile of the electron bunch consists of a central part with a uniform current and a gaussian head and tail. The current modulation is added to the full profile (figure 7.2). The shape of the profile is obtained by adjusting the charge of the sub-bunches. All sub-bunches have the same length. The distance between the centers of two subsequent sub-bunches is the same as their rms length.

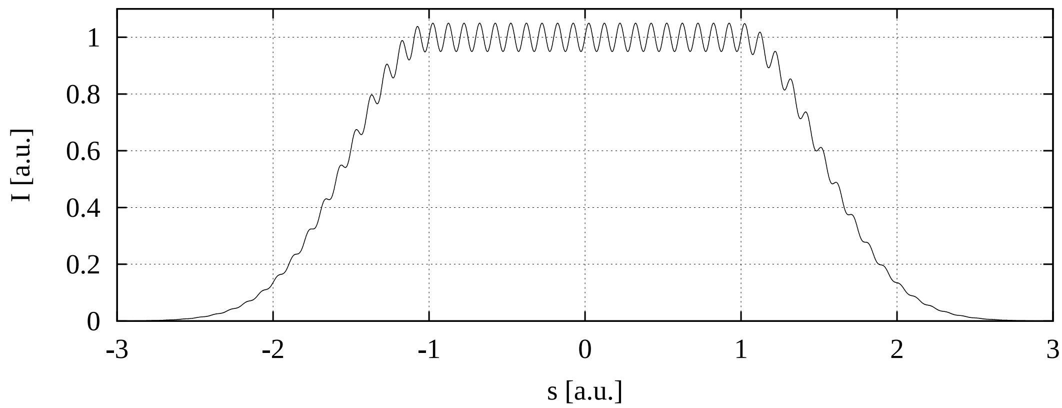

Figure 7.2: *An example of a modulated current profile is sketched. The profile has a gaussian head and tail and a uniform central part. The sinusoidal modulation is added to the full profile. In this sketch the modulation amplitude is exaggerated. The initial relative amplitude which is used in the simulations is below* 10^{-3} *and would not be visible in the plot.*

Since the longitudinal profile is obtained by a summation over gaussian sub-bunches, each sub-bunch has to be shorter than the wavelength of the modulation. Test simulations showed that at least 15 sub-bunches should be used per modulation period. If fewer sub-bunches are used, the gain decreases (figure 7.3). Actually, in my simulations I used up to 20 sub-bunches per period. The central part of the current profile has a length of 20 modulation periods. Consequently, the flat top consists of up to 400 sub-bunches.

The gaussian head and tail of the bunch have a total length of $90\,\mu$m each. To simulate a bunch with a modulation of $2\,\mu$m wavelength the sub-bunches have a length of $0.1\,\mu$m. That means, to model the head and the tail 1800 sub-bunches are needed and the full distribution consists of 2200 sub-bunches. This distribution does not include uncorrelated energy spread or transverse emittance.

The simplest way to include uncorrelated energy spread is to copy the full distribution to several energy levels in the longitudinal phase space and to adjust the charge in a way that the energy profile is gaussian. At least three levels with higher and three with lower energy should be populated. Unfortunately, this leads to distributions consisting of more than 10000 sub-bunches. When adding transverse emittance the number would be even higher.

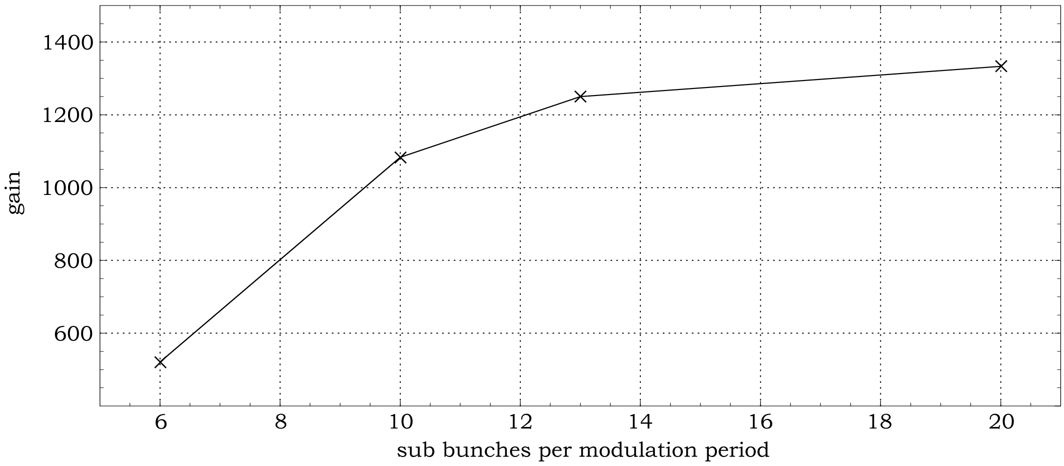

Figure 7.3: *The gain, which is calculated from simulation results, depends on the number of sub-bunches used per modulation period. At least* 15 *sub-bunches have to be used per period to get good results.*

In the simulations the maximum usable number of sub-bunches is about 10000. Otherwise the simulations would take too long. To reduce the number of sub-bunches the uncorrelated energy spread and the emittance were considered only for the modulated flat top part of the distribution. Unfortunately, strong deformations of the CSR fields start to build up at the edges of this region and, eventually, the full phase space distribution gets disturbed. The simulation results are only usable if at least a part of the modulated flat top remains undisturbed (figure 7.4).

A major problem in the simulations arises from the use of 1D line distributions. Since the density modulation is converted into an energy modulation the transverse sub-bunch positions will also be modulated in the dispersive parts of the chicane. Thus, the local transverse density changes. In very thin bunches this can have a considerable influence on the transverse CSR fields and the sub-bunch motion is disturbed. Eventually, the longitudinal density modulation is destroyed (figures 7.5 and 7.6). To reduce this disturbance a very large transverse size of the sub-bunches or a careful modelling of the transverse phase space is needed. When the transverse sub-bunch size gets too large the convolution method is not valid (see chapter 5). Distributing sub-bunches in the transverse phase space increases the number of sub-bunches by large factors and thus also the computation time. Consequently, for the following simulations in this section the influence of transverse CSR fields was switched off, even though the code TraFiC[4] was used which is an implementation of the 3D convolution method (see chapter 5). This can be justified since the amplification of the density modulations is a longitudinal effect. For the distributions used here, the global shape of the profiles does not change much when the transverse CSR fields are switched off (figures 7.5).

In general, when the transverse CSR fields are switched off in a 3D simulation code, the results are not better than the results from the 1D projected method which is a lot faster. Consequently, the 3D convolution method is only a good choice for simulations of bunches with density modulations if the transverse phase spaces are carefully populated with sub-bunches to suppress the noise. The 2D Green's function method shows similar challenges. The simulations in sections 7.3 and 7.4 were done with the code CSRTrack and make use of the projected method.

Nevertheless, the simulation results obtained for the benchmark chicane match well with the expectations from the numerical gain curves (figure 7.7).

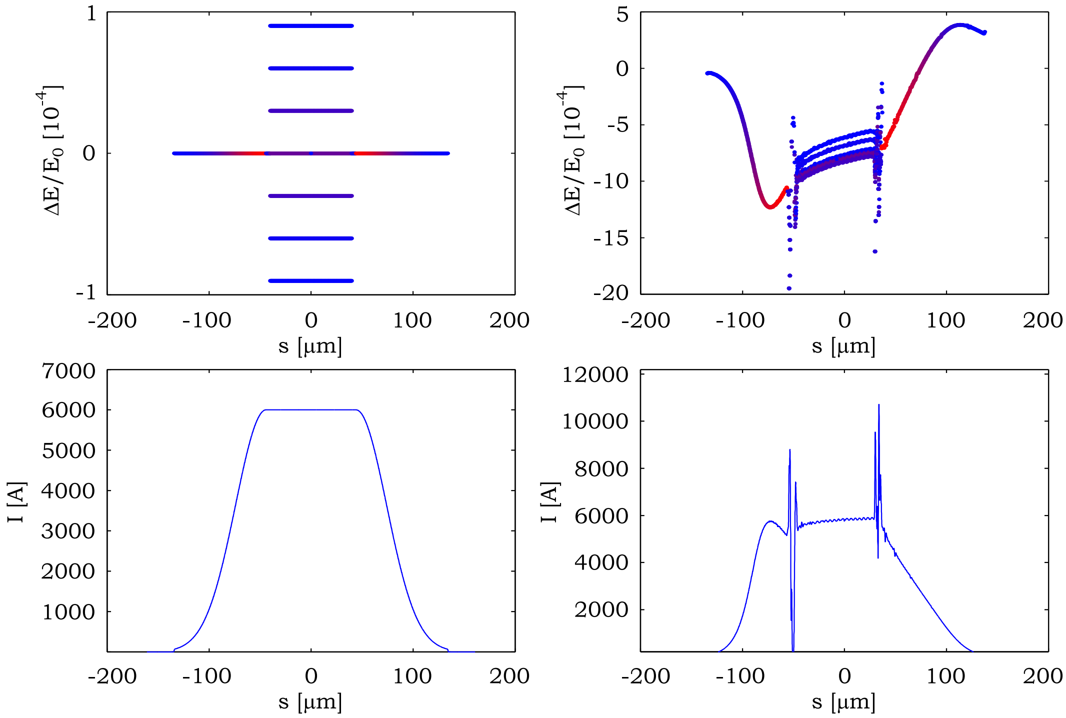

Figure 7.4: *The left column shows the initial longitudinal phase space (upper plot) and the initial current profile (lower plot) of a distribution with energy spread in the central part. The right column shows the final longitudinal phase space (upper plot) and the final current profile (lower plot).*

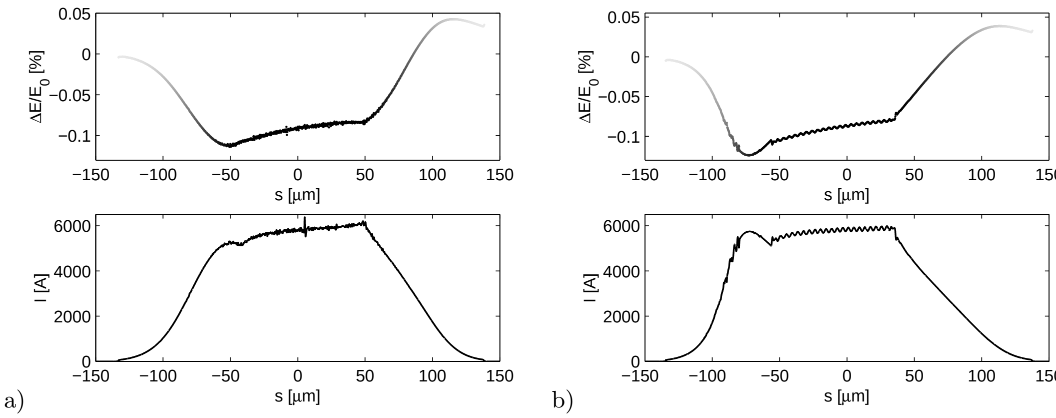

Figure 7.5: *On the left side the final longitudinal phase space (upper plot) and the final current profile (lower plot) are plotted for the case that longitudinal and transverse CSR fields are included in the simulations. On the right side the final longitudinal phase space (upper plot) and the the final current profile (lower plot) are plotted for the case that only longitudinal CSR fields are included. In the upper plots dark dots represent sub-bunches with higher charge than bright dots.*

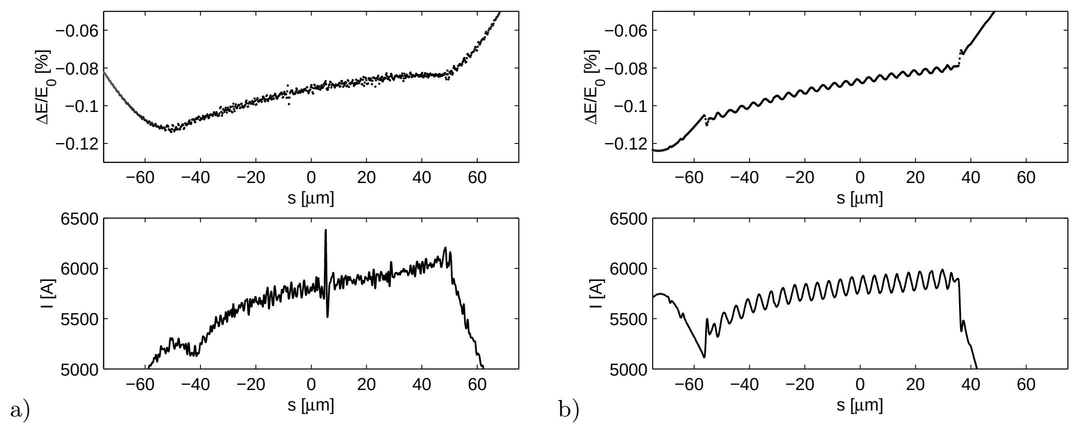

Figure 7.6: *Enlargements of the final longitudinal phase space (upper plots) and the final current profile (lower plots) are shown. The left column shows the results from simulations which include longitudinal and transverse CSR fields and the right column shows the results if only longitudinal CSR fields are included. The spike near the center of the lower left plot is a numerical error in the output file of TraFiC*[4].

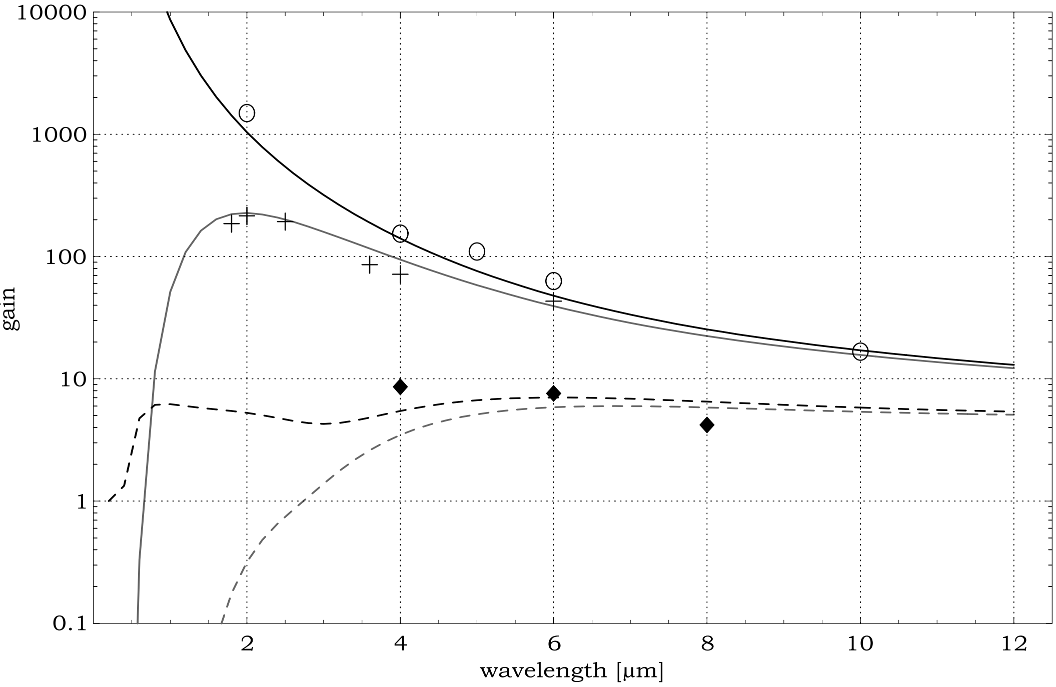

Figure 7.7: *Shown are the gain curves obtained from a numerical integration of eqn.(7.7) for a beam without energy spread and emittance (solid black), with energy spread but no emittance (solid grey), without energy spread but with emittance (dashed black) and with energy spread and emittance (dashed grey). These curves are compared to the gain obtained from simulation data without energy spread and emittance (circles), with energy spread but without emittance (crosses) and without energy spread but with emittance (diamonds).*

That the gain develops linearly along a dipole is confirmed by the simulations (figure 7.8). The development of the gain along the chicane is shown in figure 7.9. The amplitudes of the density and the energy modulations are small throughout most parts of the chicane. But inside the last dipole the modulation amplitudes are strongly enhanced (figure 7.10). Since the longitudinal CSR fields travel downstream of the last dipole the energy modulation is amplified behind the chicane. The dispersion is zero and the density modulation remains unchanged. Also this behavior can be seen in figure 7.9.

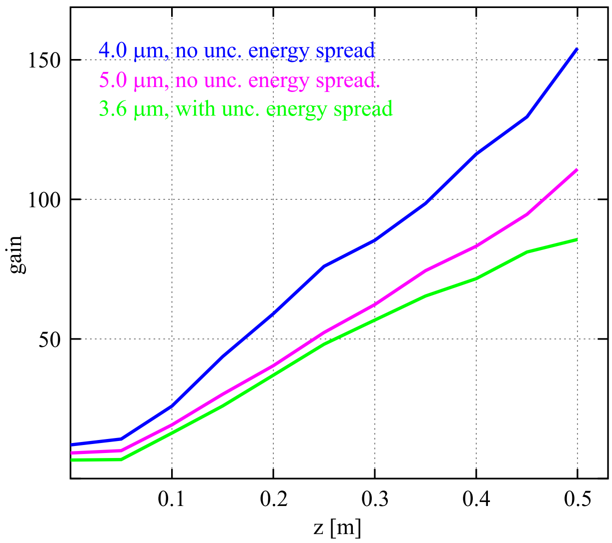

Figure 7.8: *The development of the simulated gain along the last dipole of the benchmark chicane is plotted for a bunch without uncorrelated energy spread and a modulation wavelength of* $4\,\mu$m *(black), a bunch without uncorrelated energy spread and a modulation wavelength of* $5\ \mu$m *(medium grey) and a bunch with uncorrelated energy spread and a modulation wavelength of* $3.6\ \mu$m *(light grey).*

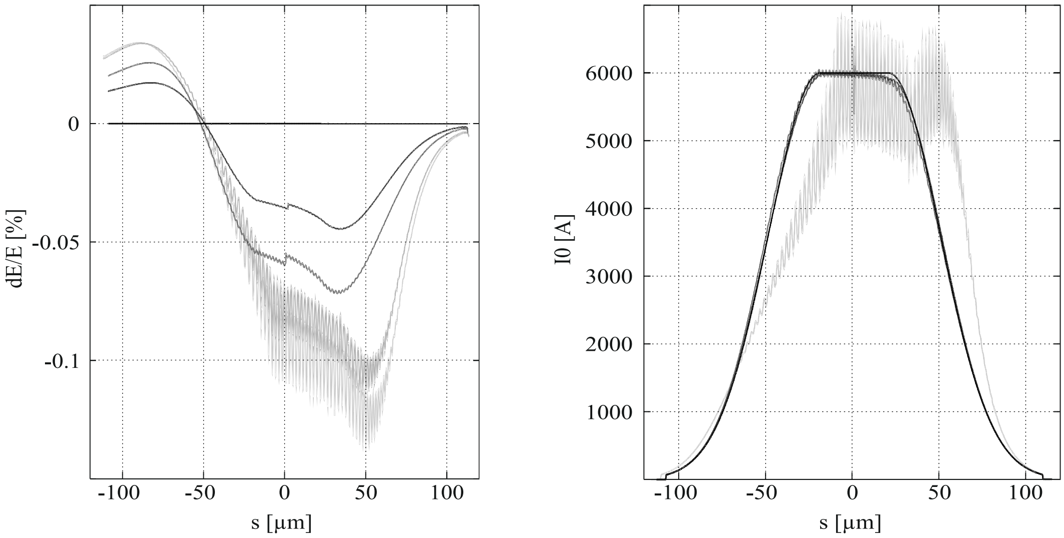

Figure 7.9: *The development of the longitudinal phase space distribution (left) and the current profile (right) along the chicane is shown (from dark to bright). Initially, there is no energy modulation but a small current modulation (black). The initial current modulation is too small to be visible. Until the end of the second dipole (dark grey) and the third dipole (medium grey) the phase space distribution is deformed by the CSR fields but only a small energy modulation builds up. Also the current modulation is only slightly stronger. At the end of the last dipole (grey) the modulation of the energy and the current is strong. After a short drift behind the last dipole (light grey) the energy modulation is even stronger. The current modulation is unchanged. The steps in the phase space distributions and the spikes in the current profiles around $s = 0$ are due to a numerical error in the output files of the first version of TraFiC^4.*

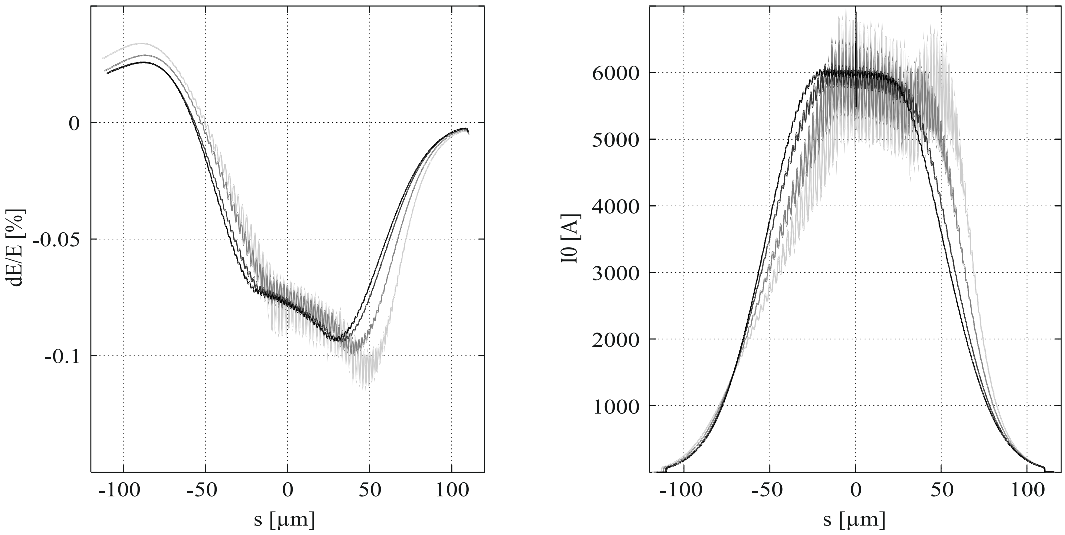

Figure 7.10: *The development of the longitudinal phase space distribution (left) and the current profile (right) along the last dipole is shown (from dark to bright). At the start of the last dipole energy and density modulation are small (black). Inside the dipole they are amplified and at the exit both modulations are strong (light grey).*

7.3 Comparison of C-chicanes and S-chicanes

S-chicanes require stronger dipoles than C-chicanes if they have the same R_{56}. Consequently, one can expect a stronger amplification of initial modulations. Here I compare a symmetric C-chicane and a symmetric 6-bend S-chicane. The chicane and electron bunch parameters are summarized in tables 7.2 and 7.3. The current profile of the electron bunch is gaussian. Thus, the gain curve along the bunch has a gaussian shape. In all plots always the peak gain is given. The simulations are performed with the code CSRTrack [67]. The 1D projected method is used.

dipole length	L_B	0.5 m		beam energy	E_0	450 MeV
1st and 3rd drift	L_{12}/L_{34}	5.75 m		peak current	I_0	500 / 2500 A
2nd drift	L_{23}	0.5 m		norm. emittance	$\varepsilon_{x,y}$	$0 / 1 \cdot 10^{-6}$ m rad
bending radius	R	7.82 m		unc. energy spread	σ_ϵ	$0 / 1 \cdot 10^{-5} / 1 \cdot 10^{-4}$
bending angle	α	3.665 deg				
momentum comp.	R_{56}	-5 cm				

Table 7.2: *Parameters of the symmetric C-chicane and the electron bunch.*

dipole length	L_B	0.5 m		beam energy	E_0	450 MeV
1st and 5th drift	L_{12}/L_{56}	2.375 m		peak current	I_0	500 / 2500 A
2nd and 4th drift	L_{23}/L_{45}	0.5 m		norm. emittance	$\varepsilon_{x,y}$	$0 / 1 \cdot 10^{-6}$ m rad
3rd drift	L_{34}	5.250 m		unc. energy spread	σ_ϵ	$0 / 1 \cdot 10^{-5} / 1 \cdot 10^{-4}$
bending radius	R	7.44 m				
bending angle	α	3.853 deg				
momentum comp.	R_{56}	-5 cm				

Table 7.3: *Parameters of the symmetric 6-bend S-chicane and the electron bunch.*

For the first comparison the peak current of the electron bunch is 500 A and the bunch is not compressed in the chicanes. If the bunch has a normalized transverse emittance of $\varepsilon_x = 1$ mm mrad, equation (7.7) results for both chicanes in a very small gain. In the S-chicane the maximum gain of a modulation in the charge density of such a bunch is 2. In the C-chicane the modulations are not amplified at all (figure 7.11). If the peak current of the bunch is 2500 A the gain increases to a maximum value of 20 in the S-chicane. In the C-chicane the gain does not exceed 8 (figure 7.12).

In figure 7.12 one can also see that simulations and numerical predictions agree well if the bunch is longer than the modulation wavelength. But if the modulation is longer than the rms length of the bunch the gain which is derived from the simulations drops below the numerical predictions. The simulations were done with gaussian bunches of $\sigma_s = 250\,\mu$m and 50 μm length.

Also when a bunch with an initial peak current of 500 A is compressed by a factor of 5 the amplification in the C-chicane and the S-chicane is different. Now the maximum gain in the S-chicane is about 15, whereas it is just 7 in the C-chicane (see figure 7.13).

In all three cases it is observable that energy spread and transverse emittance suppress the gain of short modulations. Especially, if a bunch with an uncorrelated energy spread of $\frac{\sigma_\epsilon}{E_0} = 10^{-4}$ and with a normalized transverse emittance of $\varepsilon_x = 1$mmmrad is compressed in a C-chicane the gain of modulations up to an initial wavelength of 80 μm does not exceed one. In S-chicanes only modulations longer than 55 μm are amplified. If the uncorrelated energy spread is $\frac{\sigma_\epsilon}{E_0} = 10^{-5}$ shorter modulations are also amplified. In C-chicanes the threshold lies at 7 μm and in S-chicanes it lies at 8 μm.

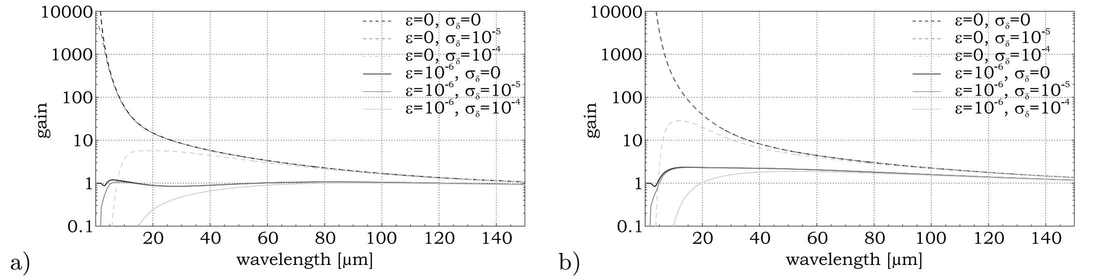

Figure 7.11: *The gain curves which are given by equation (7.7) are plotted for the C-chicane (a) and the S-chicane (b). Solid curves show the gain for bunches with a normalized transverse emittance of* $\varepsilon_{\rm x} = 1$ mm mrad. *Dashed curves show the gain for bunches with vanishing emittance. The relative rms uncorrelated energy spread is* 0 *(black),* 10^{-5} *(grey) and* 10^{-4} *(light grey). The peak current of the electron bunch is* 500 A. *The bunch is not compressed in the chicanes.*

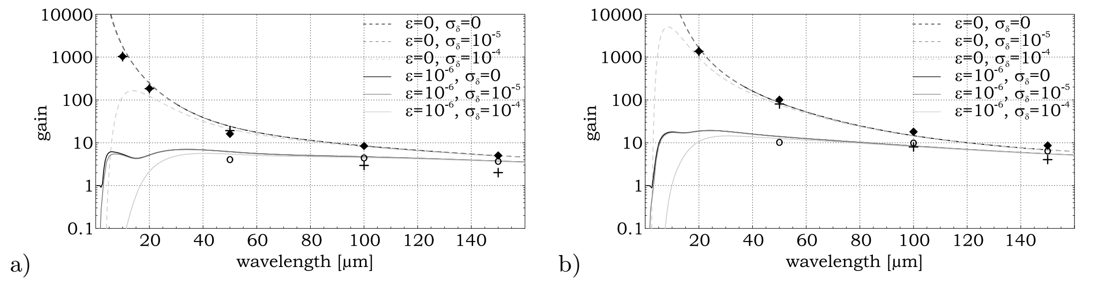

Figure 7.12: *The gain curves which are given by equation (7.7) are plotted for the C-chicane (a) and the S-chicane (b). Solid curves show the gain for bunches with a normalized transverse emittance of* $\varepsilon_{\rm x} = 1$ mm mrad. *Dashed curves show the gain for bunches with vanishing emittance. The relative rms uncorrelated energy spread is* 0 *(black),* 10^{-5} *(grey) and* 10^{-4} *(light grey). The peak current of the electron bunch is* 2500 A. *It is not compressed in the chicanes. The simulations agree well with the numerical results if the bunch has a length of* $\sigma_{\rm s} = 250\ \mu$m *and neither emittance nor energy spread (diamonds). Also when emittance is added simulations and numerical results agree well (circles). But if the bunch has a length of only* $\sigma_{\rm s} = 50\ \mu$m *in the simulations, the gain of modulations longer than the rms bunch length drops below the numerical predictions (crosses).*

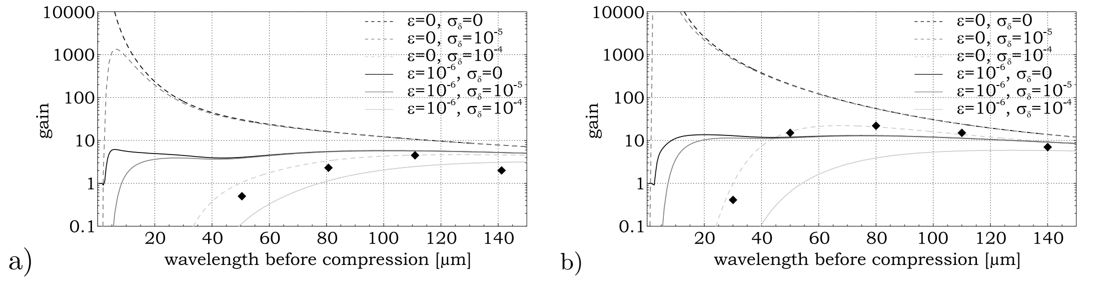

Figure 7.13: *The gain curves which are given by equation (7.7) are plotted for the C-chicane (a) and the S-chicane (b). Solid curves show the gain for bunches with a normalized transverse emittance of* $\varepsilon_{\rm x} = 1$ mm mrad. *Dashed curves show the gain for bunches with vanishing emittance. The relative rms uncorrelated energy spread is* 0 *(black),* 10^{-5} *(grey) and* 10^{-4} *(light grey). The initial peak current of the electron bunch is* 500 A. *It is compressed to a peak current of* 2500 A. *The simulations (diamonds), which include* 10^{-4} *relative rms uncorrelated energy spread but no transverse emittance, fit well to the predictions. But for long modulations the theoretical model starts to overestimate the simulated gain.*

In figure 7.14 it can be seen that the gain does not depend on the number of modulation periods in the bunch profile. The simulations were performed for a modulation wavelength of 50 μm. The bunch includes no emittance or energy spread. It has a peak current of 2500 A and is not compressed. Hence, the profile does not need to be really modulated. Any disturbance in the charge density will be amplified. The gain depends on the length of the disturbance and the local current.

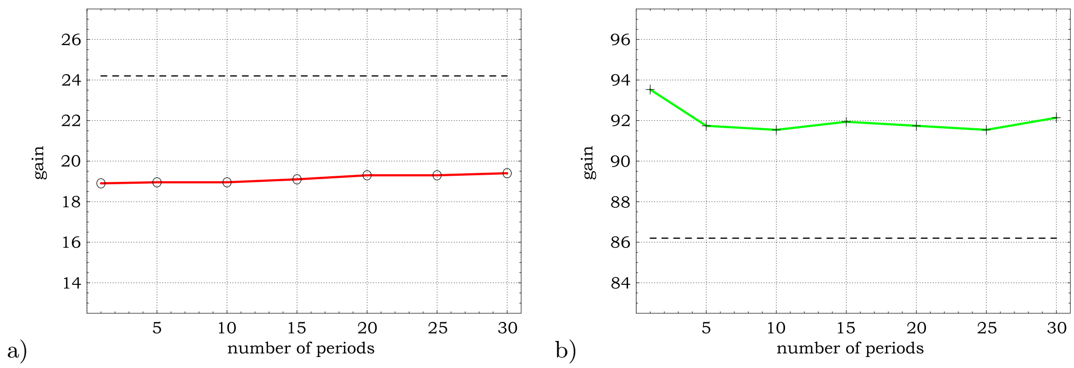

Figure 7.14: *The gain in the C-chicane (a) and in the S-chicane (b) is plotted for different numbers of modulation periods on top of a uniform profile with a current of* 2500 A. *The dashed lines are the numerical predictions. The differences between the simulations and the predictions lie within the simulation accuracy.*

Since the gain of very short modulations is suppressed by the emittance and especially by the uncorrelated energy spread these short modulations are not a concern. Long modulations, on the other hand, are only suppressed if they are longer than the bunch length. They can become important. The difference between S-chicanes and C-chicanes is not of major importance. In BC3 one can expect that modulations in the range of $50 - 150\mu$m are amplified by factors of up to 10. The lower boundary of this range depends on the value of the uncorrelated energy spread. If the uncorrelated energy spread is just $\frac{\sigma_E}{E_0} = 10^{-5}$ modulations with an initial wavelength larger than 10 μm are amplified.

7.4 CSR Instability in BC2 and BC3

We have seen in the last section that the gain in BC3 is moderate. But in the TTF2 linac one has to consider the interaction of BC2 and BC3. An initial density modulation will be amplified in BC2 and an additional energy modulation will build up. In BC3 the density and the energy modulation will be amplified. Their gain will depend on the amplitudes of both modulations in front of BC3. The gain which is predicted by the theoretical model should be smaller than the gain which is calculated from the simulation results since the model only considers an initial density modulation in the current profile and neglects the influence of the initial energy modulation.

Here simulations are performed which start just in front of BC2 and end a little downstream of BC3. The initial rms bunch length is $\sigma_s = 2$ mm. Its current profile is gaussian with a small sinusoidal modulation. A linear energy slope is induced in the longitudinal phase space to allow a compression in BC2 by a factor of 8. In ACC2 and ACC3 the electron bunch is accelerated from an initial energy of 130 MeV to a final energy of 450 MeV. It passes through the modules slightly off-crest to increase the energy slope. The compression factor in BC3 is 5. The final bunch length is $\sigma_s = 50$ μm. The phase space curvature which is induced by the R_{566} in BC2 is artificially taken out in front of ACC2. The curvature induced by the RF is small and its influence on beam dynamics is insignificant. No uncorrelated energy spread is included in the simulations, but transverse emittance is taken into account.

As expected the simulation results show that the gain in BC2 follows exactly the theoretical predictions (figure 7.15a). But the gain in BC3 is about a factor of 3 higher than predicted by eqn. (7.7) since the amplification process starts not only from a density modulation but also from an energy modulation (figure 7.15b). Thus the total gain of an initial density modulation is higher (figure 7.16).

The gain in the beam line is negligible only for short modulations. If $\frac{\sigma_\epsilon}{E_0} = 10^{-4}$ only modulations longer than 400μm in front of BC2 will become important. The exact location of the cut-off will strongly depend on the amount of uncorrelated energy spread in the bunch. If $\frac{\sigma_\epsilon}{E_0} = 10^{-5}$ the cut-off will be at shorter modulation wavelengths. Additionally, the peak gain will be higher in this case. The gain is important over a broad range and might reach up to 100.

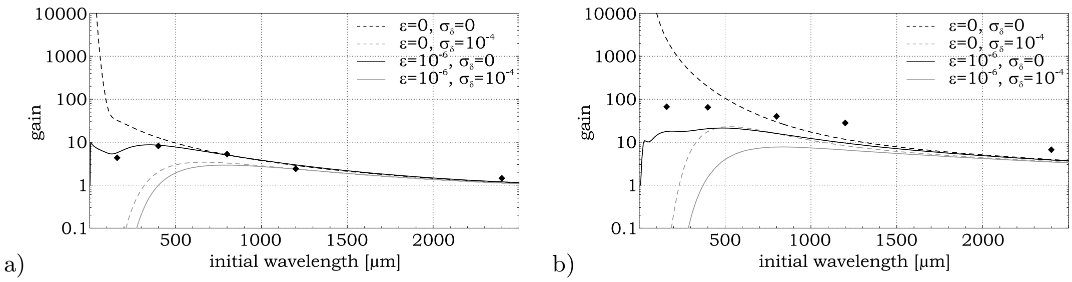

Figure 7.15: *The numerical gain curves in BC2 (a) and BC3 (b) are compared to simulation results (dots). The simulations were done only for the case that the initial bunches include transverse emittance but no uncorrelated energy spread.*

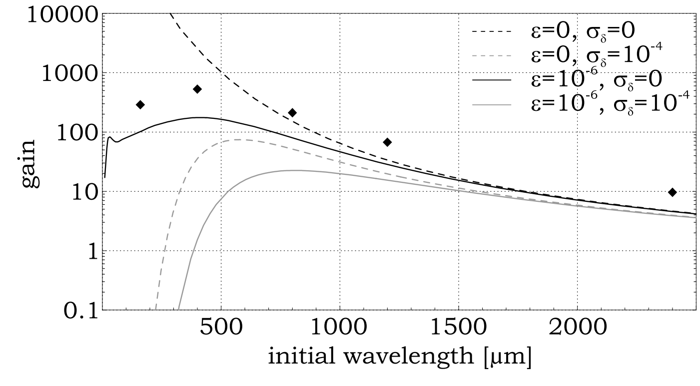

Figure 7.16: *The numerical gain curves in the beam line starting in front of BC2 and ending behind BC3 are compared to simulation results (dots). The simulations include emittance only. The numerical gain curves are multiplications of the individual gain in BC2 and BC3.*

Chapter 8

Conclusion and Outlook

SASE FELs rely on high quality electron bunches in terms of a small transverse emittance, a small energy spread and a high longitudinal charge density. At TTF2 low emittance bunches are produced in an RF gun. However, their peak current is limited due to the space charge fields and they must be compressed longitudinally before they pass the undulators. In the low energy part of a linac bunch compression can be done by velocity bunching. But if the electrons are ultra-relativistic, dispersive beam lines with an energy dependent path length are the only possibility to reduce the length of electron bunches. In the TTF2 linac two magnetic chicanes, BC2 and BC3, are included to compress the electron bunches in two stages. BC2 is a standard C-shaped chicane built of four dipoles and is based on the second bunch compressor which was already used at TTF1. BC3 had to be newly designed.

A main concern in bunch compressor chicanes is the coherent synchrotron radiation (CSR) which is generated by the electrons in the bending magnets. The longitudinal CSR fields lead to a nonuniform energy redistribution along the bunch and thus to chromatic effects in the chicane. Consequently, the transverse correlated emittance grows. The transverse CSR fields blow-up the transverse phase space distribution and dilute the slice emittance. Also higher order effects of the longitudinal CSR fields contribute to the slice emittance.

Various symmetric and asymmetric C-shaped and S-shaped chicanes are compared analytically and by computer simulations within this thesis. From geometric considerations, which included the impact of the longitudinal CSR fields, it is shown that the correlated emittance behind an S-shaped chicane is smaller than that behind a C-shaped chicane which compresses the electron bunches by the same amount. This prediction is confirmed by the computer simulations.

For the computer simulations the chicane settings and the parameters of the incoming electron bunch are varied to find an appropriate layout for BC3. A symmetric S-shaped chicane built of six dipoles is found to be a good solution. In this chicane the growth of the transverse emittance due to the CSR fields is smaller than that in the C-shaped chicanes. Asymmetric S-shaped chicanes and S-shaped chicanes built of four dipoles are only slightly better in terms of emittance growth than the chosen layout.

The mechanical and magnetic properties of dipole magnets designed for BC2 are analyzed. They match the requirements of BC3 and allow to build a very flexible bunch compressor chicane. The bending angles can be varied between 2.1° and 5.4°. This corresponds to an R_{56} ranging from $-1.5\,\mathrm{cm}$ to $-10\,\mathrm{cm}$. The magnets can also be switched off and the beam can pass through BC3 without deflection. The total length of the magnetic chicane is 14 m. Together with the quadrupoles, the steering magnets and the diagnostic systems both in front of and behind the chicane the total length of the BC3 section is 21.9 m.

The impact of CSR is estimated in the computer simulations by making use of different calculation methods. The simplest, and thus fastest, is the one-dimensional projected method which only calculates the longitudinal CSR fields of a one-dimensional charge distribution. The most complicated but also most correct method is the three-dimensional integration of the scalar and vector potentials. Unfortunately, this second method is too slow for a direct implementation in computer codes. Therefore the calculation effort is reduced by using a convolution of a longitudinal one-dimensional profile and a transverse two-dimensional charge density to describe the three-dimensional sub-bunches which model the charge distribution. By making slight approximations the calculation of the electromagnetic fields can then be reduced to a sum of a one-dimensional integration and analytical functions. Nevertheless, only some 1000 sub-bunches can be used to model the charge distribution. Otherwise the calculation time would be too high.

To overcome the limitation of the three-dimensional convolution method in terms of the number of sub-bunches which can be tracked, a two-dimensional calculation of Green's functions on a mesh can be used. This method is faster than the convolution method and yields more precise results than the projected method. Due to these advantages the Green's function method is very well suited for the calculation of the electromagnetic fields in bunch compressor simulations.

CSR will not only lead to an emittance growth but also to an amplification of density or energy modulations in the electron bunch. This effect is called CSR microbunch instability. The amplification factor depends on the modulation wavelength and increases towards shorter modulations. However, uncorrelated energy spread and emittance suppress the amplification of very short modulations.

The simulations performed within this thesis show a good agreement with the predictions from a theoretical model, although the amplification of modulations with wavelengths exceeding the rms bunch length is overestimated by the theoretical model. This is caused by the assumption of infinite bunch length on which the derivation of the model is based.

For a symmetric 6-bend S-shaped chicane the amplification factors are higher by a factor of $2-3$ than those in a symmetric C-shaped chicane. From this point of view a C-chicane might have been the preferred layout for BC3. Nevertheless, when the lower emittance growth in S-chicanes is taken into account, they still seem to be a good choice. A quantitative comparison of both chicanes is only possible, when the exact shape of the electron bunch is known, since the emittance growth and the growth of the energy spread induced by the CSR microbunch instability strongly depend on the initial phase space distribution of the electron bunch.

Using BC3 parameters for the simulations shows that modulations in the wavelength range of $10-150\,\mu$m are amplified by factors up to 10. The lower boundary will increase if the assumed uncorrelated energy spread is higher.

In a beam line consisting of two bunch compressors one should expect a stronger amplification than the theoretical model predicts. In the first bunch compressor the amplification process starts from a pure density modulation. But in the second bunch compressor the amplification starts from a combined density and energy modulation which was induced in the first bunch compressor. This behavior is confirmed by simulations of a beam line starting in front of BC2 and ending behind BC3. The total amplification factor is found to reach up to two orders of magnitude.

The simulations of modulated electron bunches presented in this thesis neglect the influence of wake fields. Additionally, the CSR fields are only calculated by the simple projected method. Thus, the influence of space charge and transverse CSR fields is not taken into account. All these effects lead to a nonlinear modification of the phase space distribution. From simple physical arguments one can expect that very short modulations in the micrometer range in either energy or charge density should be further suppressed. In contrast to this, long modulations might be even amplified, e.g. as explained in [35] for a space charge driven instability.

A more realistic development of the full 6D phase space distribution of the electron beam can only be obtained in start-to-end simulations. They should take into account space charge fields throughout the full beam line and wake fields when possible, e.g. the geometric wake fields in the cavities. The CSR fields in the bunch compressor chicanes should be calculated by using the Green's function method. Also the reduction of the CSR power due to the shielding effect of the vacuum chamber is important. The beam model has to include transverse emittance and uncorrelated energy spread.

These very demanding simulations are feasible due to a considerable development of the simulation codes during the past years and an increasing speed of the computers. Especially the implementation of the Green's function method in the CSR codes makes it possible to simulate the behavior of charge distributions consisting of several 10000 sub-bunches on the computers available at DESY. This should be enough to populate the horizontal phase space and to include uncorrelated energy spread in the beam model. Consequently, it is a lot easier to incorporate CSR simulations in start-to-end simulations which usually make use of bunches consisting of several 10000 up to some 100000 particles generated by space-charge codes like ASTRA.

The simulation results obtained will allow a better understanding of beam dynamics and can be a good basis for the commissioning of a new accelerator, e.g. the VUV-FEL.

Appendix A

Recursive calculation of Dispersion and Momentum Compaction Factor

From the definitions of the matrix elements in formulae (3.8) and (3.9) we see that it is easy to calculate dispersion and momentum compaction factor up to any order when the energy dependencies of the particle offset $x(\delta)$ and the path length $l(\delta)$ are known. But in some situations it may be more convenient to use $x(\alpha)$ and $l(\alpha)$ directly without introducing the dependence on the energy. For convenience I will denote dispersion and momentum compaction factor with $R_{m6}^{(n)}(\alpha)$. The order of the matrix element is given by n. Offset and path length are denoted with $R_{m6}^{(0)}(\alpha)$.

A particle with an energy deviation δ_{E} is deflected in a rectangular dipole by the angle $\sin\alpha^* = \frac{\sin\alpha}{1+\delta_{\mathrm{E}}}$. For the calculation of the $R_{m6}^{(n)}(\alpha)$ also the derivatives

$$\frac{\partial\delta}{\partial\alpha} = -\frac{1}{\tan\alpha}\frac{\sin\alpha_0}{\sin\alpha} \quad \Leftrightarrow \quad \frac{\partial\alpha}{\partial\delta} = -\tan\alpha\frac{\sin\alpha}{\sin\alpha_0} \tag{A.1}$$

are needed. Following the definition in formula (3.8) the first order matrix element is

$$R_{m6}^{(1)}(\alpha) = \left(\frac{\partial\alpha^*}{\partial\delta}\frac{\partial u(\alpha^*)}{\partial\alpha^*}\right)_{\alpha^*=\alpha} = -\tan\alpha\left(\frac{\partial u(\alpha^*)}{\partial\alpha^*}\right)_{\alpha^*=\alpha} \tag{A.2}$$

To derive the second order matrix element from formula (3.9) is a little more complicated:

$$\begin{aligned}
R_{m6}^{(2)}(\alpha) &= \frac{1}{2}\left(\frac{\partial\alpha^*}{\partial\delta}\frac{\partial}{\partial\alpha^*}\left(\frac{\partial\alpha^*}{\partial\delta}\frac{\partial u(\alpha^*)}{\partial\alpha^*}\right)\right)_{\alpha^*=\alpha} \\
&= \frac{1}{2}\left(\frac{\partial\alpha^*}{\partial\delta}\right)_{\alpha^*=\alpha}\left(\frac{\partial u(\alpha^*)}{\partial\alpha^*}\frac{\partial}{\partial\alpha^*}\frac{\partial\alpha^*}{\partial\delta} + \frac{\partial\alpha^*}{\partial\delta}\frac{\partial}{\partial\alpha^*}\frac{\partial u(\alpha^*)}{\partial\alpha^*}\right)_{\alpha^*=\alpha} \\
&= \frac{1}{2}\left(\frac{\partial\alpha^*}{\partial\delta}\right)_{\alpha^*=\alpha}\left(\frac{\partial u(\alpha^*)}{\partial\alpha^*}\right)_{\alpha^*=\alpha}\left(\frac{\partial}{\partial\alpha^*}\frac{\partial\alpha^*}{\partial\delta}\right)_{\alpha^*=\alpha} \\
&+ \frac{1}{2}\left(\left(\frac{\partial\alpha^*}{\partial\delta}\right)_{\alpha^*=\alpha}\right)^2\left(\frac{\partial^2 u(\alpha^*)}{\partial\alpha^{*2}}\right)_{\alpha^*=\alpha} \\
&= -\frac{1}{2}R_{m6}^{(1)}(\alpha)\frac{\cos^2\alpha+1}{\cos^2\alpha} - \frac{1}{2}\tan^2\alpha\left(\frac{\partial}{\partial\alpha^*}\left(\frac{1}{\tan\alpha^*}R_{m6}^{(1)}(\alpha^*)\right)\right)_{\alpha^*=\alpha} \\
&= -\frac{1}{2}R_{m6}^{(1)}(\alpha)\frac{\cos^2\alpha+1}{\cos^2\alpha} + \frac{1}{2}R_{m6}^{(1)}(\alpha)\frac{1}{\cos^2\alpha} - \frac{1}{2}\tan\alpha\left(\frac{\partial R_{m6}^{(1)}(\alpha^*)}{\partial\alpha^*}\right)_{\alpha^*=\alpha} \\
&= -\frac{1}{2}R_{m6}^{(1)}(\alpha) - \frac{1}{2}\tan\alpha\left(\frac{\partial R_{m6}^{(1)}(\alpha^*)}{\partial\alpha^*}\right)_{\alpha^*=\alpha}
\end{aligned} \tag{A.3}$$

Following the same steps also the third order or even higher order matrix elements can be calculated. Already from (A.2) and (A.3) the following recursive formula can be derived which describes the matrix elements up to any order $n \geq 1$:

$$R_{m6}^{(n)}(\alpha) = -\frac{n-1}{n}R_{m6}^{(n-1)}(\alpha) - \frac{1}{n}\tan\alpha\left.\frac{\partial R_{m6}^{(n-1)}(\alpha^*)}{\partial\alpha^*}\right|_{\alpha^*=\alpha} \tag{A.4}$$

Bibliography

[1] M. Tigner, A possible Apparatus for Electron Clashing-Beam Experiments, Nuovo Cimento 37, pp. 1228-1231, 1965

[2] R. Assmann, Beam Dynamics in SLC, in proceedings of PAC1997, Vancouver, Canada, May 1997

[3] R. Assmann, LEP Operation and Performance with Electron Positron Collisions at 209 GeV, in proccedings of the 11^{th} workshop on LEP performance, Chamonix, France, January 2001

[4] R. Schmidt, Status of the LHC, in proceedings of EPAC2002, Paris, France, June 2002

[5] F. Richard, J. R. Schneider, D. Trines, A. Wagner (editors), TESLA Technical Design Report, DESY 2001-011, March 2001

[6] Y. H. Chin, JLC R&D Status, in proceedings of PAC2001, Chicago, USA, June 2001

[7] N. Phinney, Next Linear Collider Design Status, in proceedings of HEACC2001, Tsukuba, Japan, March 2001

[8] R. Brinkmann, G. Materlik, J. Rossbach, J. R. Schneider, B.-H. Wiik, An X-Ray FEL laboratory as part of a linear collider design, NIM A 393, pp. 86-92, July 1997

[9] C. Pellegrini et al., A 2 to 4 nm High Power FEL on the SLAC LINAC, NIM A 331, pp. 223-227, 1993

[10] F. Richard, J. R. Schneider, D. Trines, A. Wagner (editors), TESLA XFEL Technical Design Report Supplement, DESY 2002-167, October 2002

[11] D. Edwards (ed.), TESLA Test Facility Linac Design Report, TESLA 95-01, March 1995

[12] J. Rossbach, A VUV free electron laser at the TESLA Test Facility at DESY, NIM A 375, pp. 269-273, June 1996

[13] V. Ayvazyan et al., A new powerful source for coherent VUV radiation: Demonstration of exponential growth and saturation at the TTF Free-Electron Laser, Eur. Phys. J. D 20, pp. 149-156, June 2002

[14] SASE FEL at the TESLA Test Facility Phase 2, Tesla-Fel 2002-01, June 2002

[15] J. Andruszkow et al., First Observation of Self-Amplified Spontaneous Emission in a Free-Electron Laser at 109 nm Wavelength, Phys. Rev. Letters 85(18), pp 3825-3829, October 2000

[16] K. Floettmann, T. Limberg, P. Piot, Generation of ultrashort electron bunches by cancellation of nonlinear distortions in the longitudinal phase space, Tesla-Fel 2001-06, June 2001

[17] P. Castro, Beam trajectory calculations in bunch compressors of TTF2, DESY technical note 2003-01, April 2003

[18] K. Tiedke et al., The SASE FEL at DESY: Photon Beam Diagnostics for the User Facility, in proccedings of SRI2003, San Francisco, USA, August 2003

[19] B. Faatz, The SASE FEL at the TESLA Test Facility as user Facility, in proceedings of FEL2002, Argonne, USA, September 2002

[20] J. M. J. Madey, Stimulated Emission of Bremsstrahlung in a Periodic Magnetic Field, Journal of Applied Physics 42(5), pp. 1906-1913, April 1971

[21] L. R. Elias et al., Observation of Stimulated Emission of Radiation by Relativistic Electrons in a Spatially Periodic Transverse Magnetic Field, Phys. Rev. Letters 36(13), pp. 717-720, March 1976

[22] E. L. Saldin, E. A. Schneidmiller, M. V. Yurkov, The Physics of Free Electron Lasers, Springer, 2000

[23] J. Rossbach, Linac Based Free-Electron Lasers, in proceedings of CERN Accelerator School, Brunnen, Switzerland, July 2003

[24] S. Reiche, Numerical Studies for a Single Pass High Gain Free-Electron Laser, DESY-Thesis 2000-012, March 2000

[25] J. M. J. Madey, Relationship between Mean Radiated Energy, Mean Squared Radiated Energy and Spontaneous Power Spectrum in a Power Series Expansion of the Equation of Motion in a Free-Electron Laser, Nuovo Cimento 50B, pp. 64-88, March 1979

[26] A. M. Kondratenko and E. L. Saldin, Generating Of Coherent Radiation By A Relativistic Electron Beam In An Ondulator, Part. Accel. 10, pp. 207-216, 1980

[27] R. Bonifacio, C. Pellegrini, L. M. Narducci, Collective instabilities and high-gain regime in a free electron laser, Opt. Commun. 50(6), pp. 373-378, July 1984

[28] S. Milton et al., Exponential Gain and Saturation of a Self-Amplified Spontaneous Emission Free-Electron Laser, Science 292(5524), pp. 2037-2041, June 2001

[29] K. Floettmann, P. Piot, An Upgraded Injector for the TTF FEL-User Facility, in proceedings of EPAC2002, Paris, France, June 2002

[30] W. Decking, G. Hoffstaetter, T. Limberg, Bunch Compressor for the TESLA Linear Collider, TESLA 2000-40, January 2001

[31] P. Emma, V. Bharadwaj, Bunch Compressor Options for the LEUTL Facility at the APS, June 1999, unpublished

[32] H. Wiedemann, Particle Accelerator Physics 1+2, 2nd Edition, Springer, 2003

[33] K. L. Brown, A First- and Second-Order Matrix Theory for the Design of Beam Transport Systems and Charged Particle Spectrometers, SLAC-R-75, June 1982

[34] M. Borland, J. W. Lewellen, S. V. Milton, A highly flexible bunch compressor for the APS LEUTL FEL, in proceedings of LINAC2000, Monterey, USA, August 2000

[35] E. L. Saldin, E. A. Schneidmiller, M. V. Yurkov, Longitudinal Space Charge Driven Microbunch Instability in TTF2 linac, TESLA-FEL-2003-02, May 2003

[36] J. Schwinger, On Radiation by Electrons in a Betatron, transcribed by M. A. Furman, LBNL-39088, July 1996

[37] Ya. S. Derbenev, J. Rossbach, E. L. Saldin, V. D. Shiltsev, Microbunch Radiative Tail-Head Interaction, Tesla-FEL 95-05, September 1995

[38] B. Murphy, S. Krinsky, R. L. Gluckstern, Longitudinal Wakefield for an Electron Moving on a Circular Orbit, Part. Accel. 57, pp. 9-64, 1997

[39] E. L. Saldin, E. A. Schneidmiller, M. V. Yurkov, On the coherent radiation of an electron bunch moving in an arc of a circle, NIM A 398, pp. 373-394, October 1997

[40] J. S. Nodvick, D. S. Saxon, Suppression of Coherent Radiation by Electrons in a Synchrotron, Phys. Rev. 96(1), pp. 180-184, October 1954

[41] J.D. Lackson, Classical Electrodynamics, 3rd Edition, J. Wiley&Sons, 1999

[42] V. G. Bagrov, N. I. Fedosov, I. M. Ternov, Radiation of relativistic electrons moving in an arc of a circle, Phys. Rev. D 28(10), pp. 2464-2472, November 1983

[43] R. Talman, Novel Relativistic Effect Important in Accelerators, Phys. Rev. Letters 56(14), pp. 1429-1432, April 1986

[44] G. V. Stupakov, Effect of Centrifugal Transverse Wakefield for Microbunch in Bend, SLAC-PUB-8028, December 1998

[45] G. Geloni, J. Botman, J. Luiten, M. van der Wiel, M. Dohlus, E. Saldin, E. Schneidmiller, M. V. Yurkov, Transverse Self-Fields within an Electron Bunch Moving in an Arc of a Circle, DESY 02-048, April 2002

[46] G. Geloni, J. Botman, M. van der Wiel, M. Dohlus, E. Saldin, E. Schneidmiller, M. V. Yurkov, Transverse Self-Interactions within an Electron Bunch Moving in an Arc of a Circle (Generalized), DESY 03-044, April 2003

[47] M. Dohlus, A. Kabel, T. Limberg, Optimal Beam Optics in the TTF-FEL Bunch Compressor Sections: Minimizing the Emittance Growth, in proceedings of PAC1999, New York, USA, March 1999

[48] P. Emma, R. Brinkmann, Emittance Dilution through Coherent Energy Spread Generation in Bending Systems, in proceedings of PAC1997, Vancouver, Canada, May 1997

[49] S. A. Kheifets, B. Zotter, Shielding Effects on Coherent Synchrotron Radiation, CERN SL-95-92 (AP), Geneva, Switzerland, September 1995

[50] R. Li, C. L. Bohn, J. J. Bisognano, Analysis on the Steady-State Coherent Synchrotron Radiation with Strong Shielding, in proceedings of PAC1997, Vancouver, Canada, May 1997

[51] S. Heifets, A. Michailichenko, On the Impedance due to Synchrotron Radiation, SLAC/AP-83, December 1990

[52] R. Li, C. L. Bohn, J. J. Bisognano, Shielded Transient Self-Interaction of a Bunch entering a circle from a Straight Path, in proceedings of PAC1997, Vancouver, Canada, May 1997

[53] P. Krejcik et al., Commissioning of the SPPS Linac Bunch Compressor, in proceedings of PAC2003, Portland, USA, May 2003

[54] G. V. Stupakov, Wake and Impedance, SLAC-PUB 8683, November 2000

[55] L. Palumbo, V. G. Vaccaro, M. Zobov, Wake Fields and Impedance, in proceedings of CAS Advanced School on Accelerator Physics, pp. 331-390, Rodes, Greece, September 1993

[56] K. Yokoya, Resistive Wall Impedance of Beam Pipes of General Cross Section, Particle Accelerators 41, pp. 221-248, 1993

[57] H. Schlarb, Resistive Wall Wake Fields, Diploma Thesis, University of Hamburg, Germany, August 1997

[58] M. Dohlus, M. I. Ivanyan, V. M. Tsakanov, Surface Roughness Study for the TESLA-FEL, TESLA-FEL 2000-26, Feburary 2001

[59] L. Palumbo, A. Mostacci, D. Alessini, Review of Surface Roughness Effects on Beam Quality, in proceedings of ICFA workshop on The Physics and Application of High Brightness Electron Beams, Chia Laguna, Italy, July 2002

[60] M. Huening, Analysis of Surface Roughness Wake Fields and Longitudinal Phase Space in a Linear Electron Accelerator, DESY Thesis 2002-029, August 2002

[61] W. Giesske, private communication

[62] G. V. Stupakov, Impedance of Small-Angle Collimators in High-Frequency Limit, SLAC-PUB-8857, June 2001

[63] G. V. Stupakov, Geometrical Wake of a Smooth Taper, SLAC-PUB-95-7086, December 1995

[64] K. Yokoya, Impedance of Slowly Tapered Structures, CERN SL/90-88 (AP), July 1990

[65] S. A. Heifets, S. A. Kheifets, Coupling Impedance for Modern Accelerators, SLAC-PUB-5297, May 1991

[66] M. Dohlus, A. Kabel, T. Limberg, Uncorrelated Emittance Growth in the TTF-FEL Bunch Compression Sections due to Coherent Synchrotron Radiation and Space Charge Effects, in proceedings of EPAC1998, Stockholm, Sweden, June 1998

[67] M. Dohlus, private communication

[68] M. Borland, Elegant: A flexible SDDS-compliant code for accelerator simulation, APS LS-287, September 2000

[69] F. Ciocci, L. Giannessi, A. Marranca, L. Mezi, M. Quattromini, Self-Consistent three-dimensional RF-gun dynamics integration based on the Lienard-Wiechert retarded potentials, NIM A 393, pp. 434-438, July 1997

[70] L. Giannessi, P. Musumeci, M. Quattromini, TREDI: fully 3D beam dynamics simulation of RF guns, bendings and FELs, NIM A 436, pp. 443-444, November 1999

[71] http://www.desy.de/csr, internet site of the ICFA Beam Dynamics mini workshop on Coherent synchrotron radiation and its impact on the dynamics of high brightness electron beams, Berlin, Germany, January 2002

[72] http://www.desy.de/s2e, internet site of the ICFA Future Light Sources Sub Panel mini workshop on Start-to-End Simulations of X-Ray FELs, Berlin, Germany, August 2003

[73] J. Rosenzweig, G. Travish, L. Serafini (editors), The Physics and Application of High Brigthness Electron Beams, World Scientific, 2003,
and http://www.physics.ucla.edu/AABD, internet site of the Joint ICFA Advanced Accelerator and Beam Dynamics workshop on The Physics and Application of High Brightness Electron Beams, Chia Laguna, Italy, July 2002

[74] E. L. Saldin, E. A. Schneidmiller, M. V. Yurkov, Radiative interaction of electrons in a bunch moving in an undulator, NIM A 417, pp. 158-168, November 1998

[75] M. Dohlus, Two Methods for the Calculation of CSR Fields, TESLA-FEL 2003-05, 2003

[76] M. Borland, Simple method for particle tracking with coherent synchrotron radiation, Phys Rev. ST AB 4(070701), July 2001

[77] M. Dohlus, A. Kabel, T. Limberg, Efficient field calculation of 3D bunches on general trajectories, NIM A 445, pp.338-342, 2000

[78] R. Li, Self-Consistent Simulation of the CSR Effect, in proceedings of EPAC1998, Stockholm, Sweden, June 1998

[79] M. Dohlus, Methods for CSR tracking, talk given at the ICFA Future Light Sources Sub Panel mini workshop on Start-to-End Simulations of X-Ray FELs, Berlin, Germany August 2003

[80] M. Dohlus, private communication

[81] A. Kabel, private communication

[82] A. Loulergue, A. Mosnier, Chicane, Wiggler and FODO-cells, CEA/DSM/ DAPHNIA/SEA Technical note 00-02, Saclay, France, February 2000

[83] A. Loulergue, A. Mosnier, A simple S-chicane for the final bunch compressor of TTF-FEL, DAPHNIA-SEA technical note 2000-06, Saclay, France, January 2000

[84] A. Loulergue, A. Mosnier, TTF2/BC3 optic proposal (DRAFT), Saclay, France, May 2000, unpublished

[85] A. Loulergue, A. Mosnier, TTF2 emittance versus optics (DRAFT), Saclay, Fance, June 2000, unpublished

[86] K. Floettmann, S. M. Lidia, P. Piot, Recent improvements to the ASTRA Particle Tracking Code, in proceedings of PAC2003, Portland, USA, May 2003

[87] P. Piot, private communication

[88] Y. Holler, private communication

[89] P. Emma, Bunch Compressor Beamlines for the TESLA and S-Band Linear Colliders, TESLA 95-17, July 1995

[90] J. Rossbach, private communication

[91] Y. Kim et al., Tolerances of the TTF2 first Bunch Compressor, in proceedings of PAC2003, Portland, USA, May 2003

[92] J. Prenting, private communication

[93] H. Grote, F. Iselin, The MAD Program, CERN/SL/90-13 (AP), 1996

[94] H. J. Eckoldt, private communication

[95] D. Noelle, private communication

[96] H. Schlarb, private communication

[97] K. L. Bane, T. O. Raubenheimer, J. T. Seeman, Electron Transport of a Linac Coherent Light Source (LCLS) Using the SLAC Linac, in proccedings of PAC1993, Washington D.C., USA, May 1993

[98] R. Li, Sensitivity of the CSR self-interaction to the local longitudinal charge concentration of an electron bunch, NIM A 475, pp. 498-503, 2001

[99] M. Borland, Start-to-End simulations of SASE FELs from the gun through the undulator, in proceedings of FEL2001, Darmstadt, Germany, August 2001

[100] T. Limberg, P. Piot, E. Schneidmiller, An analysis of longitudinal phase space fragmentation at the TESLA Test Facility, NIM A 475, pp. 353-356, 2001

[101] E. L. Saldin, E. A. Schneidmiller, M. V. Yurkov, Longitudinal Phase Space Distortions in Magnetic Bunch Compressors, in proceedings of FEL2001, Darmstadt, Germany, August 2001

[102] E. L. Saldin, E. A. Schneidmiller, M. V. Yurkov, Klystron Instability of a relativistic Electron Beam in a Bunch Compressor, Tesla-Fel 2002-02, January 2002

[103] S. Heifets, G. Stupakov, S. Krinsky, Coherent synchrotron radiation instability in a bunch compressor, Phys. Rev. ST AB 5(064401), June 2002 (a sign error is corrected in: S. Heifets, G. Stupakov, S. Krinsky, Erratum: Coherent synchrotron radiation instability in a bunch compressor, Phys. Rev. ST AB 5(129902), December 2002)

[104] Z. Huang, K. J. Kim, Formulas for coherent synchrotron radiation microbunching in a bunch compressor chicane, Phys. Rev. ST AB 5(074401), July 2002 (a sign error is corrected in: Z. Huang, K. J. Kim, Erratum: Formulas for coherent synchrotron radiation microbunching in a bunch compressor chicane, Phys. Rev. ST AB 5(129903), December 2002)

[105] Mathematica 4.2, Wolfram Research Inc., 2002

[106] G. Stupakov, private communication

Acknowledgements

During the last few years I have met many people who all contributed in one way or the other to my thesis. Some helped me to understand physics and to design BC3, some created the construction plans and built BC3, some made my work and my life more interesting. To all of you I am very grateful.

First of all, I would like to thank my advisors Prof. Dr. Peter Schmüser and Prof. Dr. Jörg Roßbach for the opportunity and the help to prepare my thesis at DESY.

I am indebted to Martin Dohlus for many useful discussions about synchrotron radiation and its calculation in computer codes. The computer code he provided, proved to be a valuable tool for my simulations.

When I started my thesis Philippe Piot and Torsten Limberg always found time to explain the physics of bunch compressors to me. Throughout the years several questions have also been answered by Evgeny Schneidmiller and at the end Gianluca Geloni clarified some subtleties which I would not have understood without him. Markus Körfer kindly supported me with my part of the technical planning. I want to thank all of you.

I should not forget Alexandre Loulergue and Alban Mosnier from CEA Saclay who started the design of BC3. And by doing so they founded the basis of the final BC3 layout.

Andreas Kabel from SLAC had a hard time with me pointing out several bugs in his simulation code, though I had a hard time with his code. Thank you for your patience.

I must apologize to Marieke de Loos and Bas van der Geer from Pulsar Physics. You spent so much time answering my questions about your computer program and implementing things for me into it. However, in the end the start-to-end simulations were not included in my thesis and, consequently, I don't present a single result obtained with your code. By the way, I also send best wishes to Lisa.

Not only many colleagues from the accelerator physics group contributed to the realization of Bunch Compressor 3 by helping me to find a suitable layout for the chicane and the periphery, but also many colleagues from the technical groups contributed by constructing the components and finally building BC3. I would like to thank all of you.

Especially, I am indebted to Wolfgang Gießke who made the construction plans of BC3 and did a lot of the technical coordination.

For the opportunity to visit and gain insight into the work of other labs, I want to thank Helen and Don Edwards from Fermilab, Michael Borland and Stephen Milton from ANL as well as Paul Emma and Patrick Krejcik from SLAC. I very much enjoyed my time during those visits.

I also want to thank Susan Wipf and John Maidment for proofreading my thesis. Hopefully my English is not too German anymore.

Finally, I want to say thank you to my family and to my friends. You could not help me with my thesis, but you did enough to make the past years nicer and easier. My family always supported me when necessary and even when not. Tobias, Chi Nhan, Ralf and Daniel had some food for me almost every Wednesday evening. Anna, Caro and Steffi brightened my life.

Hamburg, August 2004